FINITE ELEMENT ANALYSIS OF SLOTLINE-BOWTIE JUNCTION

by

Chong Man Yuen

A thesis submitted in partial fulfillment of the requirements for the degree of

Master of Philosophy

The Electronic Engineering Department

The Chinese University of Hong Kong

June 1997

To my family

Abstract

Slotline-Bowtie hybrid antenna is an ultra-wide band antenna. Experimental result showed that it has stable radiation pattern control over many frequency decades. The performance of the antenna can be further improved by optimizing the geometric parameters of the antenna.

Finite element method is a numerical technique for solving differential equation with boundary conditions. This methodology has been extensively used in many aspects of engineering and it has been employed in electromagnetics since 1980s. In this research, a new kind of finite element called "vector element" was adopted to eliminate non-physical, spurious modes. Two different approaches were used together to model free space radiation. Firstly, first order "absorbing boundary condition" (ABC) was imposed at the outermost surface of the computation domain. Secondly, a novel "perfectly matched layer" (PML) was placed to absorb all radiation at any incident angles. Moreover, a new mesh generator was developed to study the slotline-bowtie junction. It allows local mesh refinement to study specific region in detail.

A program was written in Fortran to study the slotline-bowtie junction. In the first step, we studied the slotline structure. The results agreed very well with closed form solution. Next, we compared the absorbing effects of different artificial layers to find the best combination of the parameters for the remaining simulations. In the second step, a taper was added at one end of the slotline. We tested the radiation patterns for different taper angles and different lengths of dielectric extension. We verified previous experimental results which stated that the optimal dielectric extension is one quarter of guided wavelength. Finally, a vertical metallic bowtie was added to the slotline taper to form the slotline-bowtie antenna. It was shown that the addition of metallic bowtie enhanced the radiation characteristics of the antenna.

Acknowledgment

"God Shall supply all your needs according to His riches in glory in Chridst Jesus."

Philippian 4:19

I would like to express my appreciation to many friends and colleagues who have helped me in this study. First of all, I wish to express my sincere gratitude to my supervisor, Prof. Albert K.Y. Lai who introduced me to this interesting problems, for his kind support and enthusiasm.

The assistance and comradeship of my fellow graduate student, both past and present, cannot be overstated. Special thanks go to Dr. Qin Zhou, Mr.Yat Man Cheng for their useful discussions; Mr. Fan Chun Wah and Mr. Wai Hung Lee who helped me solved many computer problems.

I appreciate Miss Kit Man Lau for her love and help in preparing this thesis. I also wish to thank Mr Wai Man Leung for being a great friednd. I would like to express my deepest gratitude to my family for their encouragement and confidence in me during my academic career. Finally and most importantly, I thank God for His grace and love. To our God and Father be the glory for ever and ever! Amen.

Table of Contents

List of Figure

Figure

List of Tables

Table

List of Appendices

Appendix

Chapter One

Introduction

1.1 Background

Significant advances in microwave engineering during the past few decades have changed the way many people live. For one thing, mobile phones become a necessity in a highly commercialised city. Also, sensitive radar and satellite communication systems have many applications in military and civilian area.

People enjoy the advantages of these services. More and more channels are needed to satisfy the rapid increase of demand. One possible solution to the problem is the development of a system operating with very wide bandwidth. Consequently, many wide band antennas are being developed to fulfil this requirement.

A novel slotline-bowtie hybrid antenna was presented for ultra wide-band applications [1.1]. It allows stable radiation pattern control over many frequency decades. This is useful both in military radar system and civil communication.

Basically, this antenna is a combination of slotline circuit board antenna and bowtie horn. The slotline antenna, with an improved version of Y-Y transition and a large slotline open circuit, serves as a balanced feed structure. The bowtie horn provides wide band radiation pattern.

Experiments showed that the slotline bowtie hybrid antenna is an ultra wide band antenna operating from 2 to 18 GHz with a low standing wave ratio, flat plateau-like main radiation beam. It is capable of producing both wide (60^0) and narrow (30^0) half-power beamwidths, low sidelobes and backlobe (40 to 50 dB down), and independent

control of *E*- and *H*-plane beamwidth. It is expected that performance of the antenna can be further improved by optimising the design parameters.

The principal method of studying complex wave phenomenon has shifted from analytical to computational methods. Computational electromagnetics have experienced a dramatic increase in importance over the past ten years. Because of the evolution of more powerful and less expensive computers and the development of an array of numerical techniques, the traditional analytic method with its limited applications to canonical structure is less competitive compared with the fast, accurate and flexible numerical tools.

Among many computational methods, finite element method (FEM) is selected to study the ultra-wide-band antenna. In addition to providing accurate results, the element method has the unique flexibility of handling complex shapes. This feature is important in the characterisation of the complicated slotline-bowtie junction.

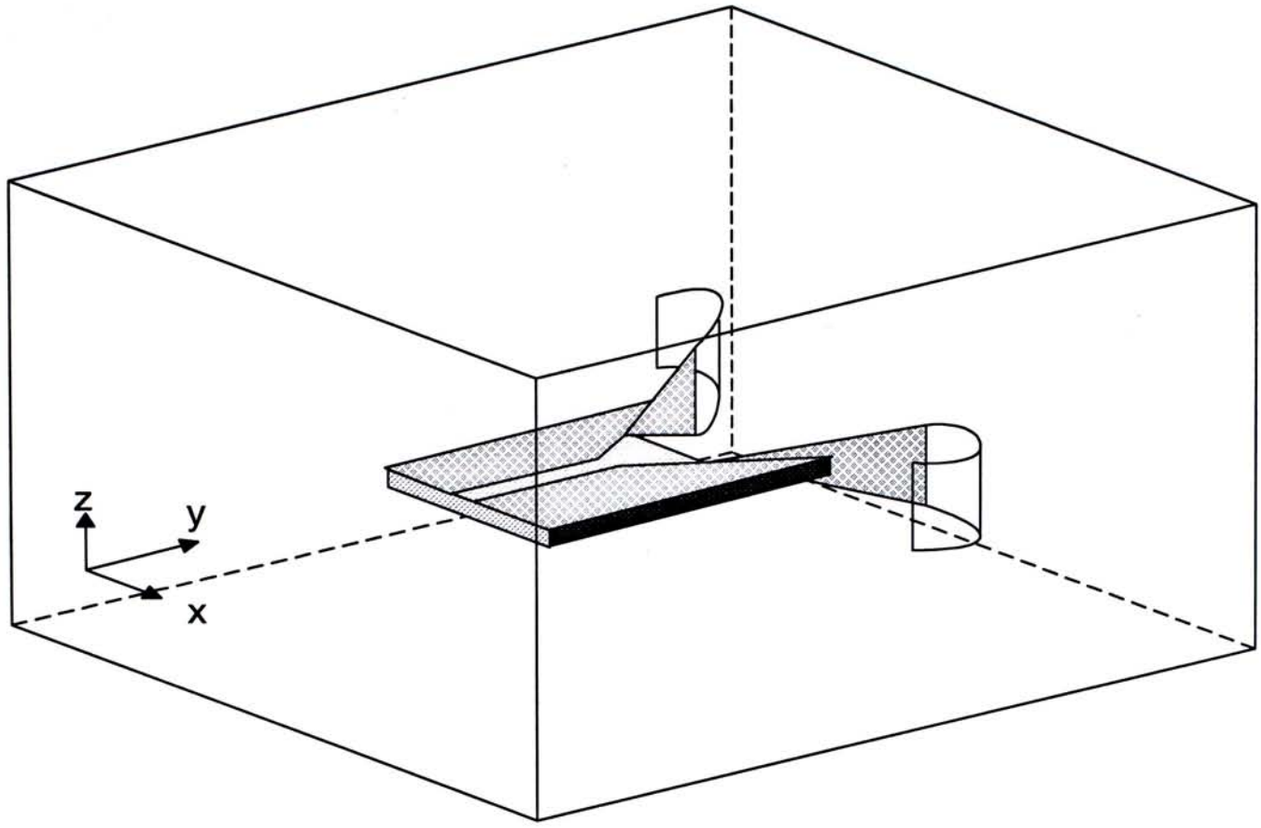

Figure 1.1 The slotline-bowtie junction

1.2 Ultra-Wide Band Antenna

In recent years, countries in Europe and North America have begun a massive liberation of the frequency spectrum for ubiquitous wireless communication use [1.2], such as digital cellular phones, cordless phones, Personal Communication Systems, low earth orbit (LEO) satellite mobile, long distance microwave/millimetre wave wireless links, etc. While some of these frequency bands are allocated, others are actually auctioned off to companies that may be local or state-wide or nation-wide.

One concern over millimetre wave transmission is atmospheric attenuation. For local areas, where cumulative atmospheric attenuation is low, large contiguous chunks of frequencies can be used. On the other hand, there are certain "pass bands" where attenuation is particularly low and is very useful for long distance propagation. For both cases, a wideband antenna that can cover multiple pass bands will be most useful because it can save a lot of communication hardware. Moreover, with the development of advanced millimetre wave components, such as the ultra wide band HEMT, the use of wide chunks of frequency (despite attenuation) over longer and longer distances is now possible. This implication is most significant, as a 10 GHz bandwidth can easily translate to 20 Gbit/s data rate. (Of course many issues in wideband circuitry need to be addressed before a commercially viable system will emerge). An undersea fibre optic cable typically carries 20 to 40 fibres, each providing 2.5 Gbit/s data rate and the total is 50 to 100 Gbit/s. Obviously a wide band wireless link is not that far off. Hence it is likely that within a few years a huge amount of data will be transmitted and received through ultra wide band wireless communications.

Researchers have sensed this and have been spending a lot of effort in the development of ultra-wideband components operating in both microwave and millimetre

wave, such as ultra wide band biasing for distributed amplifiers [1.3], 300 MHz bandwidth voltage controlled oscillators [1.4], ultra-wide-band frequency doublers [1.5], ring couplers [1.6], 4 port junctions [1.7] and other novel components. To transmit such wideband data, beamforming in sparse arrays require new techniques to suppress grating lobes [1.8]. A new method of coding data for ultra-wide-band transmission is proposed [1.9], and where even diagnostic techniques for wideband wireless communication networks need to be developed [1.10].

One thing notably missing is an ultra wide band antenna to provide the means of sending and receiving data, i.e. the front-end of the communication system. Without this, the system will not work properly. In fact, developers of ultra-wide-band systems are now relying on old wideband antenna technology. However, this is not feasible in view of several shortcomings. For example, although the old and venerable broadband horn is capable of octave frequency bandwidths, the radiation beamwidths of the antenna change drastically as a function of frequency (the higher the narrower). A wideband communication system basestation engineer would discover, to his dismay, that while the antenna radiation beam may be able to cover the cell site at the low end of the frequency bandwidth, it will only be able to cover a small portion at the high frequency end.

The essential component of this project is the slotline-bowtie hybrid antenna [1.1] that is derived from the more commonly known slotline antenna and bowtie antenna. Its use has been experimentally verified from 2 to 18 GHz in one case and 500 MHz to 17 GHz in another. Its initial desirable characteristics include wide frequency bandwidth, highly controllable beamwidths, constant beamwidth through wide frequency spread, high gain high sensitivity, etc. It is intended to be used as the feed horn of the offset reflector in an antenna compact range, which necessarily imposes the most stringent requirement on its

properties, otherwise the compact range measurement precision will be compromised. Other uses include an antenna for ground probing radar [1.11], analysis of the ice surface [1.12], pulse excited parabolic reflector systems [1.13] etc. All these applications capitalise on the very wide bandwidth of this antenna.

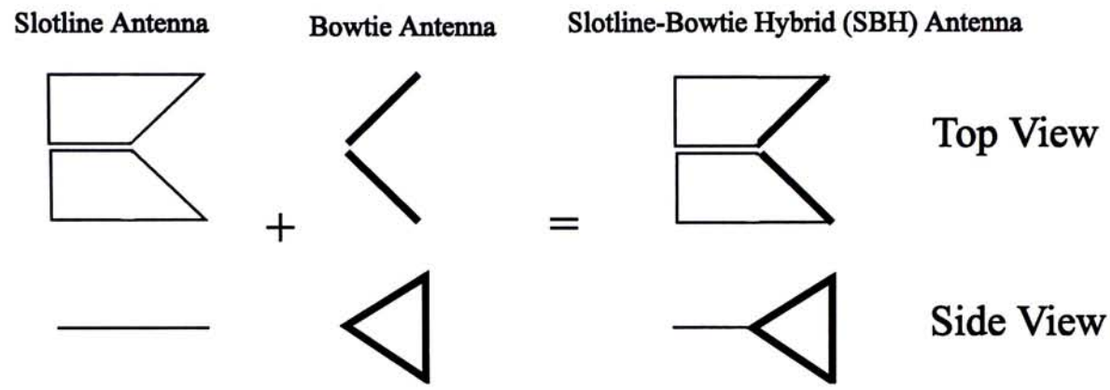

Figure 1.2 Slotline-Bowtie Hybrid (SBH) Antenna

The front end of the antenna consists of a bowtie structure. The version shown here is only the traditional bowtie. In the actual antenna, the bowtie is further extended using various blended rolled functions to roll around at its end to eliminate diffraction from that edge [1.1]. The bowtie front-end was fed by a slotline antenna, with the slotline being 37 μm wide in theory and about 120 μm wide in practice. The slotline is geometrically like the dual of microstrip, with a fine slot on the groundplane acting as the transmission line. The groundplane is on top of a thin slice of dielectric about 0.635 mm thick and with a relative permittivity of 10.8. The dielectric is so thin it is not apparent in the figure. The value of permittivity is also very important as it affects the amount of leakage field on the one hand and the radiation mechanism on the other hand. The bowtie is not directly mated to the beginning of the slotline opening, but rather is a certain distance from it, as can be seen in Fig.1.2. This distance, plus the material in that space (not shown), is of paramount

importance to the radiation mechanism of this antenna. Although not modelled here, the original antenna is fed from a microstrip line coupled to the slotline via a Y-Y microstrip to slotline transition [1.9](Fig.1.3). Because of this, the antenna allows ample space for the placement of active circuitries to convert the antenna to an Active Antenna. Moreover, the existence of both microstrip and slotline adds to the flexibility of placing active circuitries.

This antenna was experimentally conceived and has eluded detailed analysis for a long time due to its very complicated shape, sharp tips located at sharp triangular openings, thin and finite sized dielectric, very smooth blended-rolled contoured bowtie surface, and extremely narrow slotline track. The slotline antenna alone has been studied by Taflove et. al. [1.14] while the bowtie antenna alone has been studied by Shlager and Smith [1.15]. However, rough approximations are made in both papers. To model the slotline to bowtie junction, a more flexible meshing technique, which is offered by Finite Element Method, is needed.

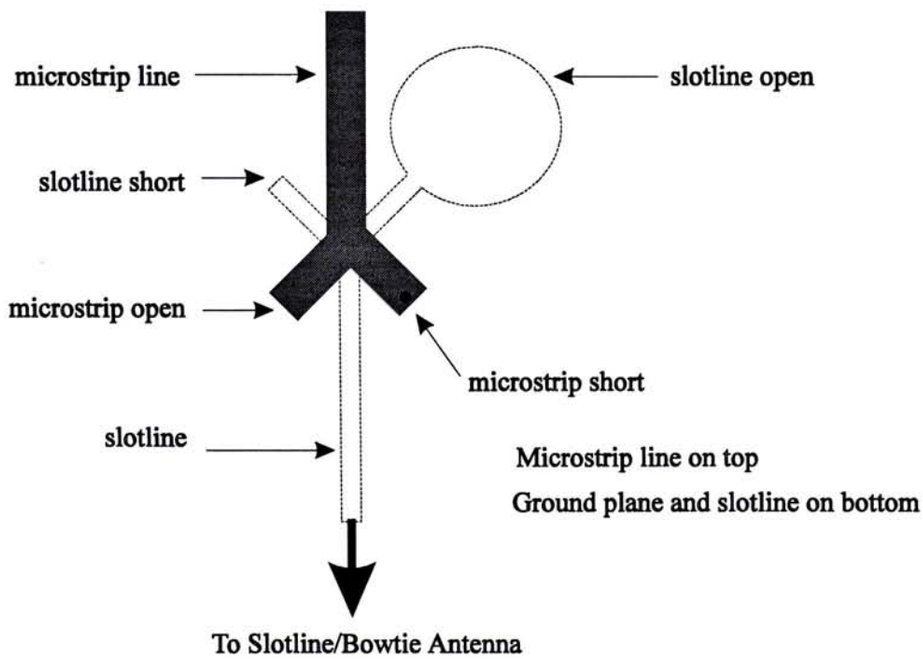

Figure 1.3 An improved Y-Y microstrip to slotline transition

Figure 1.4 A Slotline-Bowtie Hybrid (SBH) antenna operating with high performance from 50 MHz to 20 GHz. Standing some 13 feet tall at the ElectroScience Lab, Ohio State University, USA. Courtesy Professor W. D. Burnside, ElectroScience Lab, Ohio State University.

1.3 Finite Element Method (FEM)

The finite element method is a numerical tool for obtaining solutions to boundary-value problems. A typical boundary-value problem can be defined by a governing differential equation in a domain Ω:

$$\mathcal{L}\phi = \chi \tag{1.1}$$

together with the boundary condition on the boundary Γ that encloses the domain. In (1.1), $\mathcal{L}$ is a differential operator, χ is the excitation function or source, and ϕ is the unknown quantity to be determined. The principle of Finite Element method is to replace an entire continuous domain by a number of discrete sub-domains in which the unknown function is represented by simple interpolation functions with unknown coefficients.

In other words, the original boundary-value problem with infinite number of degrees of freedom is approximated into a problem with a finite number of degrees of freedom. Rather than solving the differential equation directly, the problem is transformed into a variational problem. In this work, a set of algebraic equations or a system of equations is obtained by applying the Ritz method, which is a variational procedure. Finally, solution of the boundary-value problem is obtained by solving the system of equations.

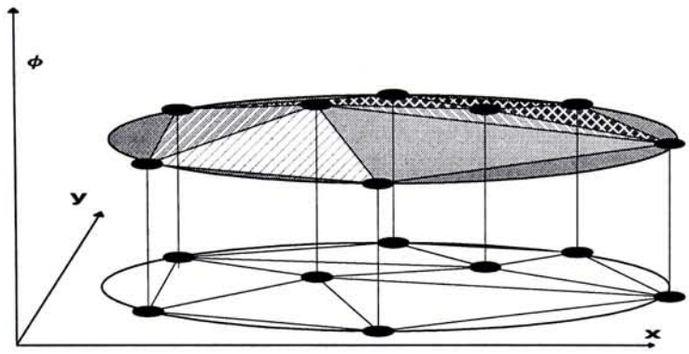

Figure 1.5 Piecewise elements are used to represent the unknown function in boundary condition problem

In general, the basic steps in a finite element simulation is as follows:

THEORETICAL DEVELOPMENT
1) Identify the governing differential equation and specify the boundary conditions.
2) Construct a corresponding functional for the problem.
3) Develop a specific expression of the trial function.
4) Apply variational method to the functional and substitute the trial function to obtain a system of equations.
5) Prepare expressions for element matrices.

(B) NUMERICAL COMPUTATION
1) Specify all numerical data for the problem.
2) Evaluate element matrix for each element and assemble them into a system of equations.
3) Incorporate boundary conditions into the system of equations.
4) Solve the system of equations.
5) Analyse the result.

Table 1.1 Basic procedures in a typical finite element (FE) analysis

1.3.1 Domain Discretization

In this step, the entire domain Ω is sub-divided into a number of small domains, denoted as Ω^e $(e=1,2,3,...M)$, with M denoting the total number of subdomains. A good mesh should capture the fine geometric details of the object. In some region, the function may change so dramatically that denser mesh is necessary at that area.

The selection of the structure of small domain also determines the expression of shape function representing that subdomain. In a domain governed by a linear, self-

adjoint (symmetric) and positive-bounded operator of order $2m$, where m is any natural number, the trial function should fulfil two requirements listed below:

a) *Completeness condition*: The element trial solution and any of its derivatives up to order m should be able to assume any constant within an element, in the limit as the size of the element reduces to zero.

b) *Continuity condition*: The C^{m-1} continuity interelement boundaries: the trial function and its derivatives up to order of $m-1$ should be continuous.

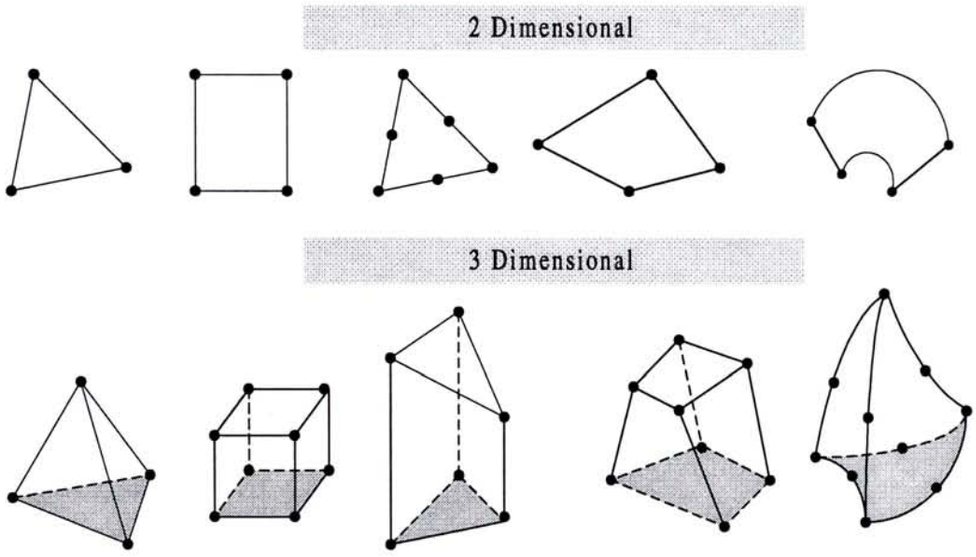

Figure 1.6 Examples of finite elements

Usually, the trial function is expressed as a polynomial of the form

$$\phi = \alpha_1 + \alpha_2 x + \alpha_3 y + \alpha_4 z + \alpha_5 xy + \alpha_6 xz + \alpha_7 yz + \cdots \qquad (1.2)$$

In fact, a complete polynomial satisfies these requirements. In 2 dimensions, a polynomial is complete to degree p if it contains all terms up to and including those of degree p, i.e., all terms in the first $p+1$ rows of Pascal's triangle. Trial functions based on complete polynomial have important properties of geometric isotropy and independence of orientation. We observed that the triangular (2D) and tetrahedral (3D) elements are

particular useful for modelling the bowtie-slotline junction. Detailed derivation of the interpolation functions for these elements are given in Appendix1.

Furthermore, it is possible to rewrite the trial function as a summation of products of interpolation function and nodal value of each node, i.e.,

$$\tilde{\phi}^e = \sum_{j=1}^{n} N_j^e \phi_j^e \tag{1. 3}$$

where N_j^e is the interpolation function and, ϕ_j^e is the nodal value at each node. The superscript "e" represents the element number, while the subscript j is the node number in the element. For example, the simplest expression

$$N_j^s = L_j^s = \frac{1}{2\Delta^s}(a_j^s + b_j^s x + c_j^s y) \qquad (\textit{on } XY \text{ plane})$$

2-Dimensional triangular element (1. 4)

and

$$N_j^e = L_j^e = \frac{1}{6V^e}(a_j^e + b_j^e x + c_j^e y + d_j^e z)$$

3-Dimensional tetrahedral element (1. 5)

One can verify the fact that

$$N_i^e(x_j^e, y_j^e, z_j^e) = \delta_{ij} = \begin{cases} 1 & i = j \\ 0 & i \neq j \end{cases} \tag{1. 6}$$

This is an important feature that guarantees the continuity of the solution across the element side. Solving the system of equations is the final step in a finite element analysis.

1.3.2 Formulation: Variational method

The Ritz method, also known as the Rayleigh-Ritz method, is a variational method in which the boundary-value problem is formulated in terms of a variational expression, referred to as a functional, whose minimum corresponds to the governing differential equation under the given boundary conditions. The approximate solution is then obtained by minimising the functional with respect to its variables.

To illustrate the procedure, let us first define the inner product as

$$\langle \phi, \psi \rangle = \int_{\Omega} \phi \psi^* d\Omega \tag{1.7}$$

where the asterisk denotes the complex conjugate. With this definition, it can be shown that the solution to (1.1) can be obtained by minimising the functional [12]

$$F(\tilde{\phi}) = \frac{1}{2}\langle \mathcal{L}\tilde{\phi}\tilde{\phi}, \rangle - \frac{1}{2}\langle \tilde{\phi}, \chi \rangle - \frac{1}{2}\langle \chi, \tilde{\phi} \rangle \tag{1.8}$$

provided the operator $\mathcal{L}$ is self-adjoint, that is,

$$\langle \mathcal{L}\phi, \psi \rangle = \langle \phi, \mathcal{L}\psi \rangle \tag{1.9}$$

and positive definite ,that is

$$\langle \mathcal{L}\phi, \psi \rangle = \begin{cases} > 0 & \phi \neq 0 \\ = 0 & , \phi = 0 \end{cases} \tag{1.10}$$

The trial function $\tilde{\phi}$ denotes the approximation of the unknown function ϕ.

In finite element, the domain is divided into a number of subdomains, say M elements. The functional is then expressed as the sum of the functional over each element,

$$F(\tilde{\phi}) = \sum_{e=1}^{M} F^e(\tilde{\phi}^e) \tag{1. 11}$$

The trial function is usually written as

$$\tilde{\phi}^e = \sum_{j=1}^{n} N_j^e \phi_j^e = \{N^e\}^T \{\phi^e\} = \{\phi^e\}^T \{N^e\} \tag{1. 12}$$

where n is the number of node associated with the element. N_j^e are the chosen expansion functions defined over the element "e". ϕ_j^e are constant coefficients to be determined. Substituting (1.12) into (1.11), we obtain

$$F^e(\tilde{\phi}^e) = \frac{1}{2}\{\phi^e\}^T \int_\Omega \{N^e\} \mathcal{L} \{N^e\}^T d\Omega \{\phi^e\} - \{\phi^e\}^T \int_\Omega f\{N^e\} d\Omega \tag{1. 13}$$

To minimise the functional $F^e(\tilde{\phi}^e)$, the partial derivatives with respect to ϕ_j^e vanish. This yields a set of linear algebraic equation

$$0 = \frac{\partial F^e(\tilde{\phi}^e)}{\partial \phi_i^e} = \frac{1}{2} \sum_{j=1}^{N} \phi_i^e \int_\Omega (N_i^e \mathcal{L} N_j^e + N_j^e \mathcal{L} N_i^e) d\Omega - \int_\Omega N_i f d\Omega$$

or

$$0 = \frac{1}{2} \sum_{j=1}^{N} \left[\phi_i^e K_{ij}^e\right] - b_i^e \qquad i = 1,2,\ldots,N \tag{1. 14}$$

By invoking the self-adjoint property of the operator $\mathcal{L}$,

$$K_{ij}^e = \int_\Omega N_i^e \mathcal{L} N_j^e d\Omega \tag{1. 15}$$

$$b_i^e = \int_\Omega N_i^e f d\Omega \tag{1. 16}$$

we can rewrite the above in matrix form:

$$\left\{\frac{\partial F^e}{\partial \phi^e}\right\} = \begin{Bmatrix} \frac{\partial F^e}{\partial \phi_1^e} \\ \frac{\partial F^e}{\partial \phi_2^e} \\ \vdots \\ \frac{\partial F^e}{\partial \phi_n^e} \end{Bmatrix} = [K^e]\{\phi^e\} - \{b^e\} \tag{1. 17}$$

and the variation of the total functional is then:

$$\frac{\partial F(\phi)}{\partial \phi} = \sum_{e=1}^{M} \left\{\frac{\partial F^e(\phi)}{\partial \phi^e}\right\} = \sum_{e=1}^{M} [K^e]\{\phi^e\} - \sum_{e=1}^{M} \{b^e\} = 0$$

i.e.

$$\sum_{e=1}^{M} [K^e]\{\phi^e\} = \sum_{e=1}^{M} \{b^e\} \tag{1. 18}$$

An approximate solution for (1.1) is then obtained by solving the following matrix equation.

$$[K]\{\phi\} = \{b\} \tag{1. 19}$$

where $[K]$ and $\{b\}$ are formed by assembling the element matrices $[K^e]$ and $\{b^e\}$.

Chapter Two

Theory

In wave theory, the electromagnetic fields follow strictly the Maxwell's equations. In finite volume, the free propagation of wave will somehow be distorted as it interacts with materials. Such interactions have been studied intensively because of its great importance in physics and engineering. Mathematically speaking, the physical phenomena is equivalent to a second order differential equation with specific boundary conditions. Generally, it is quite difficult and time-consuming to solve analytically the electromagnetic problems involving different materials and complex structures. In fact, the problem can be solved more than one way. As an alternative, the differential equation with boundary conditions can be transformed into a functional and solved by variational method. This approach is not commonly used historically until the rapid development of powerful computers primarily due to its requirement of intensive computational power.

In numerical computations of electromagnetics, the domain is finite and the outgoing wave must be terminated at the boundary. Therefore, special treatment is necessary at the boundary so that the fictitious surface is as transparent as possible.

In this research, edge element (or vector element) is used. It is reported that the new element is free from many drawbacks of the conventional nodal elements. Therefore, it is very useful in electromagnetic computations.

Finally, we will review the basic theory of the slotline. A clear picture of the fields inside and around a slotline is useful in this study. We can compare the simulation results with the closed form solution to verify the results of the finite element method. Besides, the slotline theory provides valuable information of field distribution. We can locally refine the mesh wherever necessary.

2.1 Variational principles for electromagnetics

Variational methods have been used historically to solve many physical problems. In general, variational principle comes from *Hamilton's principle of least action.* It postulates that the dynamics of a physical system can be completely characterised if a scalar function of the system exists and is stationary [2. 1].

Mathematically, variational principle defines a scalar functional F in an integral form

$$F(\phi) = \int_{\Omega} v(\phi, \frac{\partial \phi}{\partial x}, \cdots) d\Omega + \int_{\Gamma} w(\phi, \frac{\partial \phi}{\partial x}, \cdots) d\Gamma \qquad (2.\ 1)$$

in which ϕ is the unknown function and v, w are specified operators. Ω is the domain while Γ is the boundary of the domain. The solution to a problem is a function ϕ^* which makes $F(\phi)$ stationary with respect to small change $\delta\phi$. Assuming the exact solution in the following form

$$\phi = \sum_{i=1}^{n} N_i \phi_i \qquad (2.\ 2)$$

The variation of the functional becomes

$$\delta F(\phi^*) = \frac{\partial F}{\partial \phi_1} \delta\phi_1 + \frac{\partial F}{\partial \phi_2} \delta\phi_2 + \ldots + \frac{\partial F}{\partial \phi_n} \delta\phi_n \qquad (2.\ 3)$$

and the stationary condition can be written in the matrix form:

$$\left\{ \frac{\partial F}{\partial \phi^*} \right\} = [K]\{\phi\} + \{f\} = 0 \qquad (2.\ 4)$$

If the functional $F(\phi)$ is quadratic, i.e., if the function ϕ and its derivatives occur in power not exceeding two, it can be shown that the matrix $[K]$ is always symmetric [2. 2]. This is a very important advantage of the variational approach.

2.1.2 Construction of functional

The construction of functional in electromagnetics depends on the adjointness of the differential operator $\mathcal{L}$ and the boundary operator as well as the nature of the media. The vector wave equation is

$$\nabla \times (\frac{1}{\mu_r} \nabla \times \vec{E}) - k_0^2 \varepsilon_r \vec{E} = -jk_0 Z_0 \vec{J} \qquad (2.5)$$

and the boundary conditions:

$$\hat{n} \times \vec{E} = \vec{P} \qquad \text{on } S_1 \qquad (2.6)$$

$$\frac{1}{\mu_r} \hat{n} \times (\nabla \times \vec{E}) + \xi \hat{n} \times (\hat{n} \times \vec{E}) = \vec{U} \qquad \text{on } S_2 \qquad (2.7)$$

where μ_r, ε_r and ξ are all complex valued. $\vec{P}$ and $\vec{U}$ are known vectors and ξ is a parameter specifying the surface properties. According to the generalised variational principle [2. 3], for a differential problem

$$\mathcal{L}\phi = \chi \qquad (2.8)$$

if the operator $\mathcal{L}$ is self-adjoint for homogeneous boundary conditions, then its solution can be obtained by seeking the stationary point of the functional given as

$$F(\phi) = \frac{1}{2}\langle \mathcal{L}\phi, \phi \rangle - \frac{1}{2}\langle \mathcal{L}\phi, u \rangle + \frac{1}{2}\langle \phi, \mathcal{L}u \rangle - \langle \phi, \chi \rangle \qquad (2.9)$$

in which u is any function satisfying the given inhomogeneous boundary conditions. Note that the inner product is now defined as

$$\langle \phi, \psi \rangle = \int_\Omega \phi \psi d\Omega \qquad \underline{\textit{symmetric product}} \qquad (2.10)$$

To demonstrate the application of the variational principle for the vector wave equation involving inhomogeneous boundary conditions, we first define the operator $\mathcal{L}$ as

$$\mathcal{L} = \nabla \times (\frac{1}{\mu_r} \nabla \times) - k_0^2 \varepsilon_r \qquad (2.11)$$

According to the definition of the inner product,

$$\left\langle \mathcal{L}\vec{E}, \vec{F} \right\rangle = \iiint_V \vec{F} \cdot \left[\nabla \times \left(\frac{1}{\mu_r} \nabla \times \vec{E} \right) - k_0^2 \varepsilon_r \vec{E} \right] dV \qquad (2.12)$$

applying the second vector Green's theorem (a.22) to the above yields

$$\left\langle \mathcal{L}\vec{E}, \vec{F} \right\rangle = \iiint_V \vec{E} \cdot \left[\nabla \times \left(\frac{1}{\mu_r} \nabla \times \vec{F} \right) - k_0^2 \varepsilon_r \vec{F} \right] dV$$

$$+ \oiint_S \frac{1}{\mu_r} \left[\vec{E} \times (\nabla \times \vec{F}) - \vec{F} \times (\nabla \times \vec{E}) \right] \cdot \hat{n} dA \qquad (2.13)$$

since

$$\left[\vec{E} \times (\nabla \times \vec{F}) \right] \cdot \hat{n} = (\hat{n} \times \vec{E}) \cdot (\nabla \times \vec{F}) = -\vec{E} \cdot \left[\hat{n} \times (\nabla \times \vec{F}) \right] \qquad (2.14)$$

it is clear that if both $\vec{E}$ and $\vec{F}$ satisfy the homogeneous Dirichlet boundary condition,

$$\hat{n} \times \vec{E} = 0 \qquad \text{on } S_1 \qquad (2.15)$$

and the homogeneous Neumann boundary condition of the third kind,

$$\frac{1}{\mu_r} \hat{n} \times (\nabla \times \vec{E}) + \xi \hat{n} \times (\hat{n} \times \vec{E}) = 0 \qquad \text{on } S_2 \qquad (2.16)$$

with $S_1+S_2=S$, the surface integral vanishes, even if ε_r and μ_r are complex. Thus the inner product becomes

$$\left\langle \mathcal{L}\vec{E}, \vec{F} \right\rangle = \iiint_V \vec{E} \cdot \left[\nabla \times \left(\frac{1}{\mu_r} \nabla \times \vec{F} \right) - k_0^2 \varepsilon_r \vec{F} \right] dV = \left\langle \vec{E}, \mathcal{L}\vec{F} \right\rangle \qquad (2.17)$$

So $\mathcal{L}$ is a **self-adjoint** operator for homogeneous boundary conditions.

Therefore, the corresponding functional, with these boundary conditions, can be expressed as following:

$$F(\vec{E}) = \frac{1}{2}\iiint_V \left[\nabla \times \left(\frac{1}{\mu_r}\nabla \times \vec{E} - k_0^2 \varepsilon_r \vec{E}\right)\right] \cdot \vec{E} dV$$

$$-\frac{1}{2}\iiint_V \left[\nabla \times \left(\frac{1}{\mu_r}\nabla \times \vec{E} - k_0^2 \varepsilon_r \vec{E}\right)\right] \cdot \vec{u} dV$$

$$+\frac{1}{2}\iiint_V \vec{E} \cdot \left[\nabla \times \left(\frac{1}{\mu_r}\nabla \times \vec{u} - k_0^2 \varepsilon_r \vec{u}\right)\right] dV$$

$$+ jk_0 Z_0 \iiint_V (\vec{E} \cdot \vec{J}) dV \qquad (2.18)$$

both $\vec{E}$ and $\vec{u}$ satisfy the boundary conditions (2.15), (2.16). Applying the first vector Green's theorem and discarding the terms not containing $\vec{E}$, the above becomes,

$$F(\vec{E}) = \frac{1}{2}\iiint_V \left[\nabla \times (\frac{1}{\mu_r}\nabla \times \vec{E} - k_0^2 \varepsilon_r \vec{E})\right] \cdot \vec{E} dV$$

$$+\frac{1}{2}\iint_{S_1} \frac{1}{\mu_r} \vec{P} \cdot (\nabla \times \vec{E}) dA$$

$$+ jk_0 Z_0 \iiint_V (\vec{E} \cdot \vec{J}) dV \quad + \frac{1}{2}\iint_{S_2} \vec{E} \cdot \vec{U} dA \qquad (2.19)$$

$$= \frac{1}{2}\iiint_V \left[\frac{1}{\mu_r}(\nabla \times \vec{E}) \cdot (\nabla \times \vec{E}) - k_0^2 \varepsilon_r \vec{E} \cdot \vec{E}\right] dV$$

$$+ \iint_{S_1} \left[\frac{\xi}{2}(\hat{n} \times \vec{E}) \cdot (\hat{n} \times \vec{E}) + \vec{E} \cdot \vec{U}\right] dA$$

$$+ jk_0 Z_0 \iiint_V (\vec{E} \cdot \vec{J}) dV \qquad (2.20)$$

Furthermore, we can construct the functional for anisotropic media in a similar manner. The wave equation becomes

$$\nabla \times \left[\ddot{\mu}^{-1} \cdot (\nabla \times \vec{E})\right] - k_0^2 \ddot{\varepsilon}_r \cdot \vec{E} = -jk_0 Z_0 \vec{J} \qquad (2.21)$$

with boundary conditions

$$\hat{n} \times \vec{E} = \vec{P} \qquad \text{on } S_1 \qquad (2.22)$$

$$\hat{n} \times \left[\ddot{\mu}_r^{-1} \cdot (\nabla \times \vec{E})\right] + \gamma(\vec{E}) = \vec{U}^{inc} \qquad \text{on } S_2 \qquad (2.23)$$

where $\vec{P}$ and $\vec{U}^{inc}$ are known vectors. Specifically, $\vec{U}^{inc}$ depends on the incident fields $\vec{E}^{inc}$. $\gamma(\vec{E})$ is an operator specifying the surface nature. The functional is given as [2.4]

$$F(\vec{E}) = \frac{1}{2} \iiint_V \left[(\nabla \times \vec{E}) \cdot \ddot{\mu}_r^{-1} \cdot (\nabla \times \vec{E}) - k_0^2 \vec{E} \cdot \ddot{\varepsilon}_r \cdot \vec{E}\right] dV$$

$$+ j\omega\mu_0 \iiint_V \vec{E} \cdot \vec{J} dV$$

$$- \frac{1}{2} \iint_{S_2} [\vec{E} \cdot \gamma(\vec{E})] dS$$

$$+ \iint_{S_2} [\vec{E} \cdot \vec{U}] dS \qquad (2.24)$$

provided that the dyadic relative permittivity $\ddot{\varepsilon}_r$ and dyadic relative permeability $\ddot{\mu}_r$ are symmetric:

$$(\ddot{\varepsilon})_r^T = \ddot{\varepsilon}_r \quad \text{and} \quad (\ddot{\mu}^{-1})^T = \ddot{\mu}^{-1}$$

and $\gamma(\vec{E})$ is also symmetric so that

$$\iint_s \vec{E} \cdot \gamma(\delta\vec{E}) dS = \iint_s \delta\vec{E} \cdot \gamma(\vec{E}) dS$$

2.2 Artificial Boundary

In open space scattering and radiation problems, the electromagnetic wave propagates over long distance. This implies an infinite number of unknowns in the finite element simulation to cover the open region. An artificial surface must be introduced to truncate the exterior region.

A perfect truncation should appear as transparent as possible to the scattered and radiated field. In other words, the non-physical reflections must be minimised even though the boundary is placed very closed to the object. Current research on this topic is very active [2.5][2.6][2.7][2.8]. Basically, three different approaches are commonly adopted:

1) Boundary Integral Equation
2) Conformal Absorbing Boundary Conditions
3) Perfectly Matched Layer (PML).

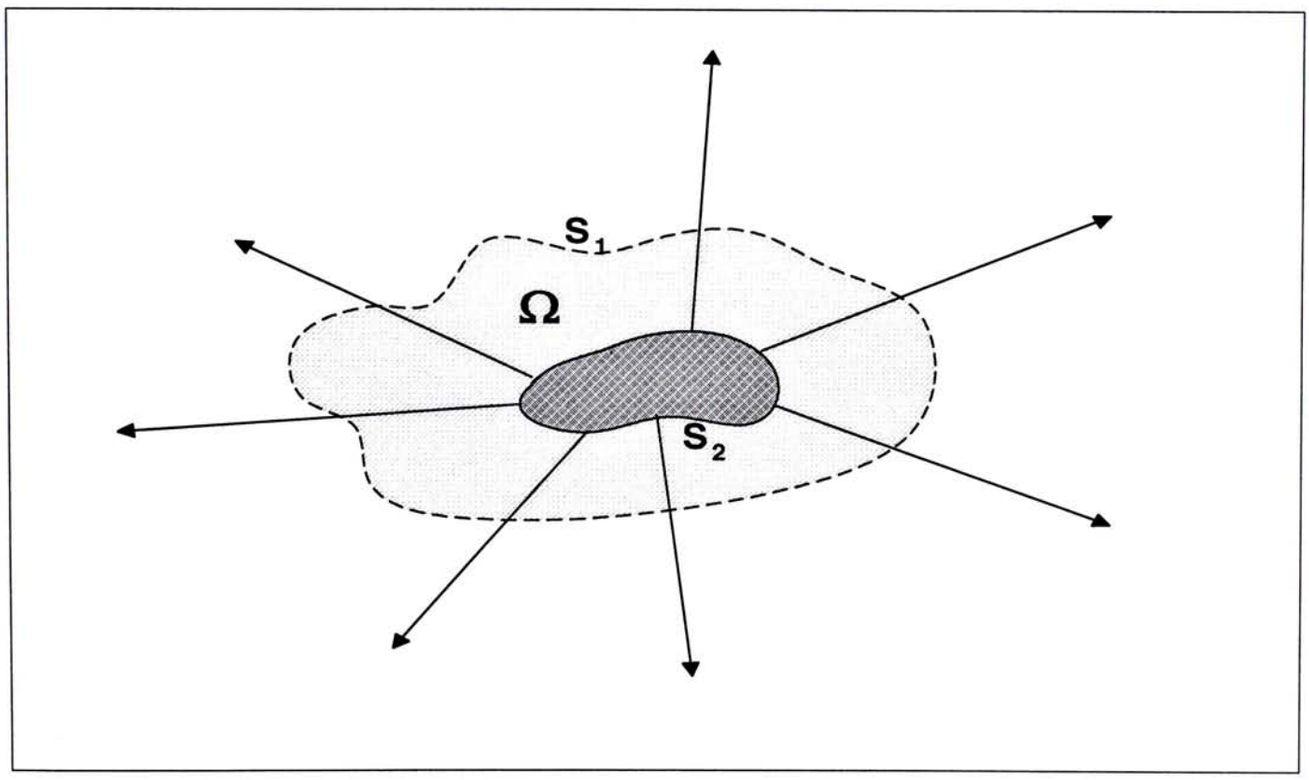

Figure 2. 1 The computational domain is enclosed by a fictitious surface S_1

For the first method, exact representation of the artificial boundary condition is an integral equation. The corresponding operator is non-local in time and space. The resultant matrix is a fully populated sub-matrix [2.4], in contrast to the highly sparse matrix generated by the finite element formulation. Actually, sparsity is a crucial advantage of the finite element method in terms of memory requirement and computational cost. The boundary integral method is also difficult to implement on complex 3 dimensional objects, consequently, it is limited to simple structures [2.9][2.10][2.11].

To overcome this compatibility problem, the so-called absorbing boundary conditions (ABCs) have been developed [2.12][2.13]. These local operators are approximate, but help retain the sparsity of the finite element matrices. Practical implementations are usually limited to the first and second order types, because, in a finite element framework, the continuity requirements of higher order ABCs are very difficult to satisfy.

A breakthrough in performance was achieved in 1994, when J. P. Berenger proposed a "Perfectly Matched Layer" in the context of finite-difference time -domain (FDTD) algorithm for electromagnetic wave problems [2.14]. Berenger's approach is based on a splitting of each Cartesian field component into two sub-components and yields a reflectionless interface between free space and the absorber. This desirable property holds for waves of arbitrary polarisation and at all incident angles.

2.2.1 Absorbing Boundary Conditions

In three dimensions, the scattered/radiated field, denoted as $\vec{E}^{sc}$, satisfies, in a homogeneous space exterior to the scattered/radiator, the vector wave equation

$$\nabla \times \nabla \times \vec{E}^{sc} - k^2 \vec{E}^{sc} = 0 \qquad (2.25)$$

and the Sommerfeld radiation condition at infinity. According to Wilcox [2.15], such a field can be represented by a convergent infinite series

$$\vec{E}^{sc}(\vec{r}) = \frac{e^{-jkr}}{r} \sum_{n=0}^{\infty} \frac{\vec{A}_n(\theta,\varphi)}{r^n} \qquad (2.26)$$

where r,θ,φ are the usual spherical co-ordinates. Webb and Kanellopoulos[2.16] constructed a general m-th order differential operator that annihilates the first m terms of (2.26). Such operators lead directly to the desired absorbing boundary condition. They defined the operator $\mathcal{B}_m$ $(m=1,2,3\ldots)$ as:

$$\mathcal{B}_m\left(g\frac{\vec{A}_n(\theta,\varphi)}{r^{n+1}}\right) = (n+1-m)(n+2-m)\ldots(n-1)ng\frac{\vec{A}_{nt}(\theta,\varphi)}{r^{n+1+m}}$$

$$+ s(n+1-m)(n+2-m)\ldots(n-2)(n-1)\nabla_t\left(\frac{g\vec{A}_{nr}(\theta,\varphi)}{r^{n+m}}\right) \qquad (2.27)$$

Since A_{or} is zero, the radial part of the electric or magnetic field vector vanishes at a great distance from the object. This is a well-known fact in electromagnetics. It can be seen that the right-hand side of (2.27) vanishes for $n = 0,1,2,\ldots m-1$, or in other words, $\mathcal{B}_m$ annihilates the first m terms of (2.26). With $n > m-1$, after being operated on by $\mathcal{B}_m$, those terms in (2.27) are proportional to $r^{-(m+n+1)}$. It turns out that

$$\mathcal{B}_m(\vec{E}^{sc}) = O(r^{-(2m+1)}) \qquad (2.28)$$

Therefore, $\mathcal{B}_m(\vec{E}^{sc}) = 0$ can be regarded as an approximate boundary condition applicable to a spherical surface of sufficiently large radius r.

Now let us derive the explicit form for the first and second order absorbing boundary conditions suitable for the finite element formulation. The first order condition is

$$\mathcal{B}_1(\vec{E}) = \hat{r} \times \nabla \times \vec{E}_t^{sc} - jk\vec{E}_t^{sc} + s\nabla_t \vec{E}_r^{sc} = 0$$

or

$$\hat{r} \times (\nabla \times \vec{E}^{sc}) \approx -jk\hat{r}\cos\theta_a \times (\hat{r} \times \vec{E}^{sc})$$

where θ_a denotes the angle of perfect absorption. The second order condition ,with s = 1, is given as [2.13]

$$\begin{aligned}\mathcal{B}_2(\vec{E}^{sc}) = \quad & -2(jk + \tfrac{1}{r})\hat{r} \times \nabla \times \vec{E}^{sc} + 2jk(jk + \tfrac{1}{r})\vec{E}_t^{sc} \quad = 0 \\ & + \nabla \times \left[r(\nabla \times E^{sc})_r\right] + jk\nabla_t \vec{E}_t^{sc}\end{aligned}$$

or

$$\hat{r} \times (\nabla \times \vec{E}^{sc}) \approx -jk_0 \cos\theta_{a1}\hat{r} \times (\hat{r} \times \vec{E}^{sc}) + \frac{\cos\theta_{a2}}{jk_0}\left\{\nabla \times \left[\hat{r}(\nabla \times \vec{E}^{sc})_r\right] + \nabla_t(\nabla \cdot \vec{E}_t^{sc})\right\}$$

where θ_{a1} and θ_{a2} are parameters controlling two angles of perfect absorption. Both the first and second order absorbing boundary conditions can be written uniformly as

$$\hat{r} \times (\nabla \times \vec{E}^{sc}) + \mathcal{P}(\vec{E}^{sc}) = 0$$

or

$$\hat{r} \times (\nabla \times \vec{E}) + \mathcal{P}(\vec{E}) = \vec{U}^{inc} \qquad (2.29)$$

where $\vec{U}^{inc}$ depends on the incident fields. $\mathcal{P}(\vec{E})$ is a surface operator defined by

$$\mathcal{P}(\vec{E}) = jk_0 \cos\theta_a \hat{r} \times (\hat{r} \times \vec{E}) \qquad (2.30)$$

where is θ_a the angle of perfect absorption for first order absorbing boundary. Similarly,

$$\mathcal{P}(\vec{E}) = jk\hat{r}\cos\theta_{a1} \times (\hat{r} \times \vec{E}) + \beta\left\{\nabla \times \left[\hat{r}(\nabla \times \vec{E})_r\right] + \nabla_t(\nabla \cdot \vec{E}_t)\right\} \qquad (2.31)$$

where $\beta = \dfrac{\cos\theta_{a2}}{jk_0}$. θ_a the angle of perfect absorption for second order absorbing boundary.

Next we show that the first order operator $\mathcal{P}(\vec{E})$ defined in (2.31) is self-adjoint. For this, we consider

$$\oiint_S \vec{F} \cdot \mathcal{P}(\vec{E})dS$$

$$= \oiint_s F \cdot \left\{jk_0\hat{r} \times (\hat{r} \times \vec{E}) - \beta\nabla \times \left[\hat{r}(\nabla \times \vec{E})_r\right] - \beta\nabla_t(\nabla \cdot \vec{E}_t)\right\}dS \qquad (2.32)$$

Invoking the vector identity

$$\vec{F} \cdot \hat{r} \times (\hat{r} \times \vec{E}) \quad = -(\hat{r} \times \vec{F})(\hat{r} \times \vec{E}) = \vec{E} \cdot \hat{r} \times (\hat{r} \times \vec{F}) \qquad (2.33)$$

(2.32) can be written as

$$\oiint_S \vec{F} \cdot \mathcal{P}(\vec{E})dS = \oiint_s \vec{E} \cdot \mathcal{P}(\vec{F})dS$$

Therefore, the operator $\mathcal{P}(\vec{E})$ of first order ABC defined in (2.29) is indeed **self-adjoint.**

2.2.2 Perfectly Matched Layer (PML)

Berenger [2.14] introduced a modification to Maxwell's equations to allow for the specification of material properties that results in a reflectionless lossy material. The material is reflectionless in the sense that a plane wave propagating through an infinite free space

/lossy material interface has no reflection for any angles of incidence. Berenger referred to this material as a perfectly matched layer (PML). Although validity of the idea was demonstrated with numerical experiments, the physical meaning of his modifications to Maxwell's equations was not very clear. Chew and Weedon [2. 17] provided a systematic analysis of the PML in terms of the concept of 'co-ordinate stretching". They demonstrated the compatibility of Berenger's modifications in a more generalised form of Maxwell's equations. Recently, an important discovery obtained by Sacks *et al* [2. 18] was that the reflectionless properties of a material can be achieved if the material is assumed to be anisotropic. Unlike Berenger's approach, this method does not require a modification of Maxwell's equations, making it easier to analyse in the general framework of electromagnetic theory. A brief derivation of the anisotropic PML is presented below by considering the simple plane wave incidence problem shown in Fig. 2.1 .

The general time-harmonic form of Maxwell's equations are

$$\nabla \cdot \ddot{\varepsilon}\vec{E} = 0 \qquad \nabla \cdot \ddot{\mu}\vec{H} = 0$$

$$\nabla \times \vec{E} = -j\omega\ddot{\mu}\vec{H} - \ddot{\sigma}_M \vec{H} \qquad \nabla \times \vec{H} = j\omega\ddot{\mu}\vec{E} + \ddot{\sigma}_E \vec{E} \tag{2. 34}$$

we consider materials where $\ddot{\varepsilon}$ and $\ddot{\mu}$ are complex diagonal tensors of the form

$$\ddot{\mu} = \begin{pmatrix} \mu_x + {}^{\sigma_M^x}/_{j\omega} & 0 & 0 \\ 0 & \mu_y + {}^{\sigma_M^y}/_{j\omega} & 0 \\ 0 & 0 & \mu_z + {}^{\sigma_M^z}/_{j\omega} \end{pmatrix}$$

and

$$\ddot{\varepsilon} = \begin{pmatrix} \varepsilon_x + {}^{\sigma_M^x}/_{j\omega} & 0 & 0 \\ 0 & \varepsilon_y + {}^{\sigma_M^y}/_{j\omega} & 0 \\ 0 & 0 & \varepsilon_z + {}^{\sigma_M^z}/_{j\omega} \end{pmatrix} \tag{2. 35}$$

the following condition is required to match the intrinsic impedance of the medium to free space:

$$\boxed{\frac{\ddot{\varepsilon}}{\varepsilon_0} = \frac{\ddot{\mu}}{\mu_0}} \qquad (2.36)$$

Thus, $\ddot{\varepsilon}$ and $\ddot{\mu}$ can be written as

$$\ddot{\mu} = \mu_0 \ddot{\Lambda} \qquad \text{and} \qquad \ddot{\varepsilon} = \varepsilon_0 \ddot{\Lambda} \qquad (2.37)$$

where $$\ddot{\Lambda} = \begin{pmatrix} a & 0 & 0 \\ 0 & b & 0 \\ 0 & 0 & c \end{pmatrix}$$

Consequently, Maxwell's equations in the medium reduce to

$$\nabla \cdot \ddot{\Lambda}\vec{E} = 0 \qquad \nabla \cdot \ddot{\Lambda}\vec{H} = 0$$

$$\nabla \times \vec{E} = -j\omega\mu_0 \ddot{\Lambda}\vec{H} \qquad \nabla \times \vec{H} = j\omega\varepsilon_0 \ddot{\Lambda}\vec{E} \qquad (2.38)$$

Combining two curl equations gives

$$\nabla \times \left[\ddot{\Lambda}^{-1} \cdot (\nabla \times \vec{E})\right] - k_0^2 \ddot{\Lambda} \cdot \vec{E} = 0 \qquad (2.39)$$

The dispersion relation, which determines the form of the propagation vector $\vec{k}$, turns out to be

$$\frac{k_x^2}{bc} + \frac{k_y^2}{ac} + \frac{k_z^2}{ab} = k_0^2 \qquad (2.40)$$

which is the equation of an ellipsoid whose solutions are of the form

$$k_x = k_0\sqrt{bc}(\sin\theta)(\cos\phi)$$

$$k_y = k_0\sqrt{ac}(\sin\theta)(\sin\phi)$$

$$k_z = k_0\sqrt{ab}(\cos\theta) \qquad (2.41)$$

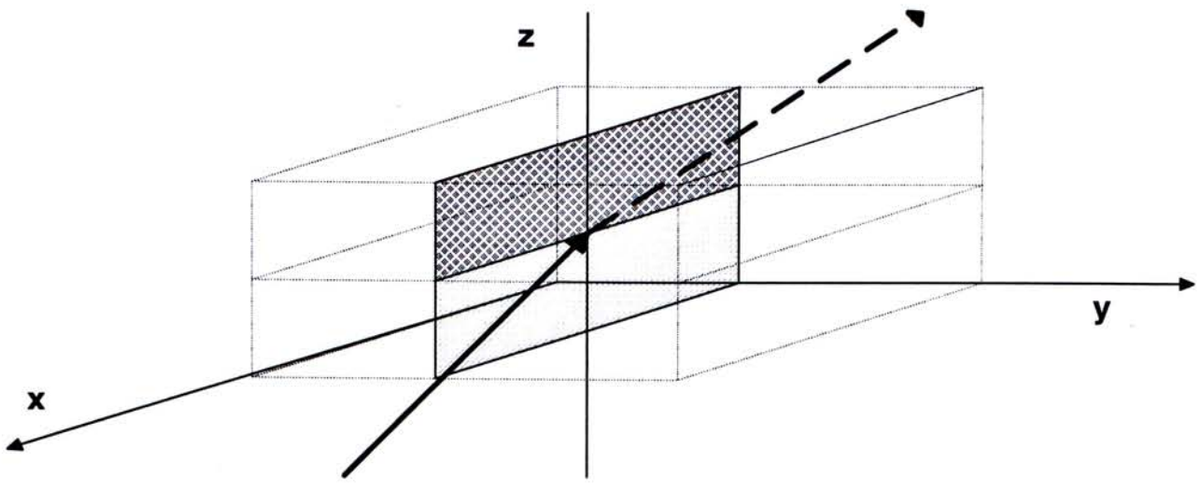

Figure 2. 2 Plane wave incident on an interface separating two half-spaces in *xz* plane

This result suggests that the individual components of the propagation vector can be manipulated through the choice of *a, b* and *c*. On the other hand, the generalisation of Snell's law (phase matching condition) requires

$$\sin\theta_i = \sin\theta_r \tag{2. 42}$$

$$\sqrt{bc}\sin\theta_t = \sin\theta_i \tag{2. 43}$$

As a result, the reflection coefficients of TE and TM case are

$$R^{TE} = \frac{\cos\theta_i - \sqrt{\frac{b}{a}}\cos\theta_t}{\cos\theta_i + \sqrt{\frac{b}{a}}\cos\theta_t} \tag{2. 44}$$

and

$$R^{TM} = \frac{\sqrt{\frac{b}{a}}\cos\theta_t - \cos\theta_i}{\cos\theta_i + \sqrt{\frac{b}{a}}\cos\theta_t} \tag{2. 45}$$

respectively. Imposing the requirement $\sqrt{bc} = 1$ simplifies the phase matching condition (16). It follows that $\theta_i = \theta_t$ and the reflection coefficients are not a function of incident angle. By also requiring $a = b$, the interface will be perfectly reflectionless for any frequency, angle of incidence, and polarisation. Thus, the values of a, b and c are not independent but are related by

$$a = b = \frac{1}{c} \tag{2. 46}$$

For this reason, the PML layer can be characterised by one complex number $a = \alpha - j\beta$. When $\alpha, \beta > 0$, the transmitted wave will be damped in the anisotropic medium

$$\vec{E}_t(x,z) = \vec{E}_0 e^{-k_0 \beta \cos\theta_{tz}} e^{-jk_0(\sin\theta_{tz} + \alpha\cos\theta_{tz})} e^{j\omega t} \tag{2. 47}$$

it is easy to see that α determines the wave length in the anisotropic absorber and β determines the rate of decay of the transmitted wave. The material tensor $\ddot{\Lambda}$ can be written in the form

$$\ddot{\Lambda} = \begin{pmatrix} \alpha - j\beta & 0 & 0 \\ 0 & \alpha - j\beta & 0 \\ 0 & 0 & \frac{\alpha + j\beta}{\alpha^2 + \beta^2} \end{pmatrix} \tag{2. 48}$$

Selection of optimum values for α and β is not unique. Intensive researches have addressed this issue and many good discussions with experimental supports have appeared recently [2. 19][2. 20][2. 21]. M. Kuzuoglu and R. Mittra [2. 22] considered the law of causality and show the frequency dependency of PML as

1) Low-frequency limit *($a\omega << 1$)*

$$a(\omega) \approx 1 + f(x, y, z) \tag{2. 49}$$

2) High-frequency limit *($a\omega >> 1$)*

$$a(\omega) \approx 1 - \frac{f(x, y, z)}{\eta\omega} \tag{2. 50}$$

where η is a constant and f is a function of position such that it reduces to zero at the free space-PML interface and is a non-decreasing function in the direction normal to the boundary. J.Y. Wu *et al*[2. 23] set arbitrarily $\alpha = \beta = s'$, sufficient absorption was obtained at $s' = 1.5$. They also pointed out that the choice of s' must be made in conjunction with the

mesh size. J.M. Jin and W.C. Chew [2. 24]suggested the value of β shall vary quadratically in the multi-layer PML, i.e.,

$$\alpha - \beta = 1 - \delta_{max}\left(\frac{l}{L}\right)^2 \qquad (2.\ 51)$$

where δ_{max} denotes the maximum loss tangent, l is the distance from the free space-PML interface and L is the thickness of the PML.

2.3 Edge basis function

In chapter one, the finite element method based on nodal formulation was discussed. The simulation results are in terms of the values of scalar field at the nodes of the element. However, some serious problems were encountered which hindered the research of field computation for many years. First, it was the occurrence of "spurious modes" [2. 25][2. 26] which were numerical solutions that have no correspondence to physical reality. Spurious eignvalues are caused by improper modelling of nullspace of the curl-curl operator[2. 27]. Secondly, the inconvenience of imposing boundary conditions at material interface as well as conducting surface. Thirdly, the traditional nodal approach faced difficulties in handling field singularities [2. 28].

A revolutionary approach based on edge element formulation was developed in [2. 29][2. 30][2. 31]. The edge element has a special property that its degrees of freedom, instead of being associated with nodes, are related to the edges of the mesh. Fortunately, all the aforementioned difficulties visually disappeared [2. 32][2. 33][2. 34]. Here, as examples, we present the expressions of first order triangular and tetrahedral edge element for two dimensions and three dimensions respectively:

Linear triangular edge element

$$\vec{N}_i^s = l_i^s (L_{i1}^s \nabla L_{i2}^s - L_{i2}^s \nabla L_{i1}^s) \qquad i=1,2,3 \qquad (2.52)$$

where

$$L_j^s = \frac{1}{2\Delta^s}(a_j^s + b_j^s x + c_j^s y) \qquad j=1,2,3,4 \qquad (2.53)$$

Linear tetrahedral edge element

$$\vec{N}_i^e = l_i^e (L_{i1}^e \nabla L_{i2}^e - L_{i2}^e \nabla L_{i1}^e) \qquad i=1,2,...,6 \qquad (2.54)$$

where

$$L_j^e(x,y,z)=\frac{1}{6V^e}(a_j^e+b_j^e x+c_j^e y+d_j^e z) \qquad j=1,2,3,4 \qquad (2.55)$$

the function L_j^s and L_j^e are *Lagrangre* Polynomial. Note that the element coefficients are discussed in chapter one and Appendix 1.

Edge i	Node i_1	Node i_2
1	1	2
2	2	3
3	3	1

Table 2. 1 Edge numbering of triangular element

Edge i	Node i_1	Node i_2
1	1	2
2	1	3
3	1	4
4	2	3
5	4	2
6	3	4

Table 2. 2 Edge numbering of tetrahedral element

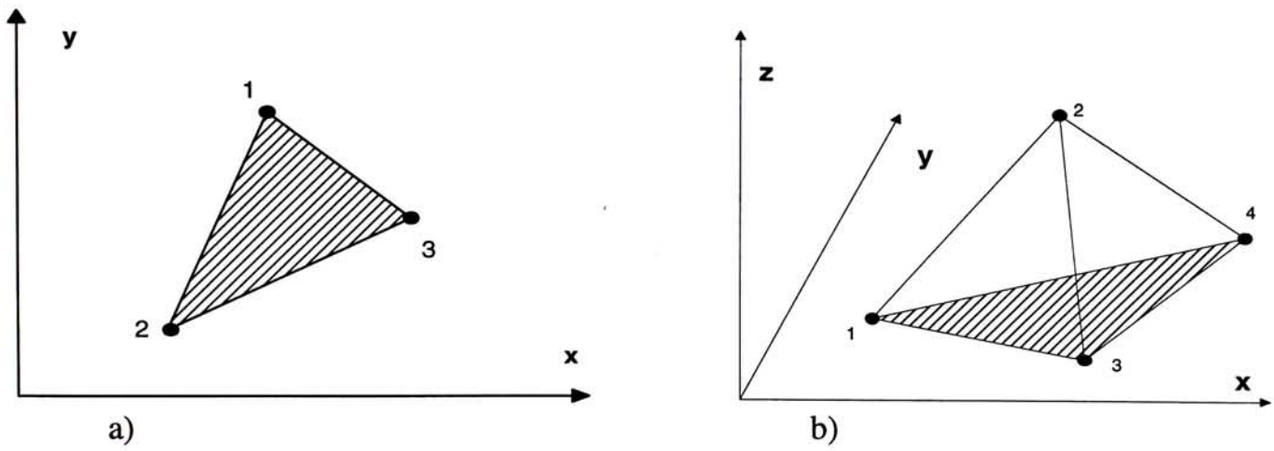

Figure 2. 3a) A triangular element on *xy* plane b) A tetrahedral element

In general, the higher order basis functions are capable of providing more accurate results with coarse mesh, fewer unknowns and less overall computation efforts [2. 35]. The

trade-off of higher order is the increase of complexity both in formulation and the program implementation. Therefor linear edge elements are good enough for most cases. Next, we consider the unique features of the edge elements. As an example, in triangular edge element, it is not difficult to observe that

$$\nabla \cdot \vec{N}_1^s = l_1^s \left[\nabla \cdot (L_1^s \nabla L_2^s) - \nabla \cdot (L_2^s \nabla L_1^s) \right] = 0 \qquad (2.56)$$

In other words, these functions satisfy the divergence condition $\nabla \cdot \vec{N}_i = 0$ within each element. Therefore, they are good candidates to represent the vector fields in source-free regions.

Another important feature of these basis functions is that $\vec{N}_i^s$ has a tangential component only along the i-th edge and none along all the other edges. Let $\vec{s}_1$ be the unity vector pointing form node 1 to node 2. Since L_1^s is a linear function that varies from one at node 1 to zero at node 2 and L_2^s is a linear function that varies from one at node 2 to zero at node 1, we have $\vec{s}_1 \cdot \nabla L_1^s = -1/l_1^s$, where l_1^s denotes the length of the edge connecting nodes 1 and 2. Therefore

$$\vec{s}_1 \cdot \vec{N}_1^s = L_1^s + L_2^s \qquad (2.57)$$

or in other words, $\vec{N}_1^s$ has a constant tangential component along the edge (1,2). Thus, the continuity of the tangential field across all element edges is guaranteed.

Obviously, the quantity

$$\nabla \times \vec{N}_i^s = l_i^s \left[\nabla \times (L_{i1}^s \nabla L_{i2}^s) - \nabla \times (L_{i2}^s \nabla L_{i1}^s) \right] = 2 l_i^s (\nabla L_{i1}^s \times \nabla L_{i2}^s) \qquad (2.58)$$

which is a non-zero constant. Thus, $\vec{N}_i^s$ possesses all the necessary properties for being a vector basis function for the edge field associated with the edge segment i.

The edge element can be characterised as a curl-conforming basis function of Nedelec type [2. 36]. The curl-conforming function maintains only tangential continuity across element boundaries. The fact that these function do not prescribed normal continuity not only makes them suitable for modelling fields at material boundaries, but is also responsible for their ability to suppress spurious nonzero eigenvalues. Besides, Webb [2. 37] considered the problem of field singularities and argued that, without any need of special trial functions, good accuracy can be obtained in global quantities.

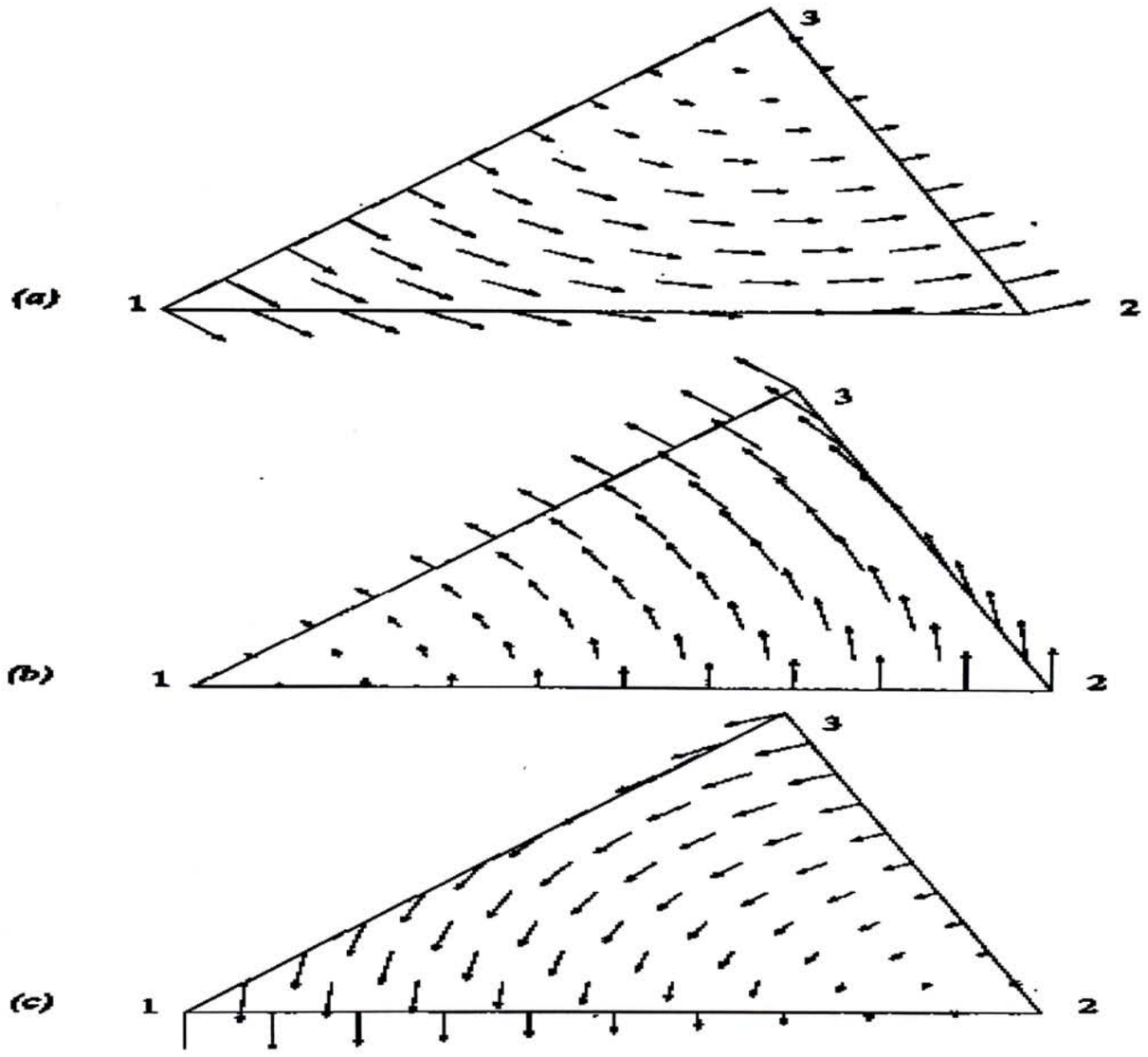

Figure2.3 Vector basis functions for a triangular element. (a) $\vec{N}_1^e$ (b) $\vec{N}_2^e$ (c) $\vec{N}_3^e$
(After J.M. Jin[24]).

2.4 Slotline Analysis

A slotline consists of a dielectric substrate with a narrow slot etched in the metallization on one side of the substrate. It is a planar transmission structure proposed for use in MICs by Cohn in 1968[2.37]. In a slotline, the wave propagates along the slot with the major electric field component oriented across the slot in the plane of metallisation on the dielectric substrate. The mode of propagation is non-TEM and almost transverse electric in nature. However, unlike conventional waveguides, there is no low frequency cut-off because the slotline is a two-conductor structure. An open circuit can be achieved by slowly tapering the metallization constituting the slot. The guide wavelength and impedance Z_0 of a slotline increases with the width of the slot. If λ_g is less than about $0.4\lambda_0$ where λ_0 is the free-space wavelength, the fields are adequately contained, and the slotline behaves as a transmission line [2.38]. Departure from this condition results in radiation. This characteristic of the slotline is the basis for the design of the new antenna. The new antenna was developed by increasing the width of the slotline gradually from the feed end so as to make λ_g greater than $0.4\lambda_0$ at the open end, thereby allowing the slotline to radiate. The slot width was tapered linearly over a length of λ_0. The open end of the slotline enhances the radiation further. This is due to the tendency of the wave propagating along the slotline to radiate in the direction of its propagation at the open end when the slot width is sufficiently large. The mechanism of radiation resembles that of a leaky wave antenna[1.1].

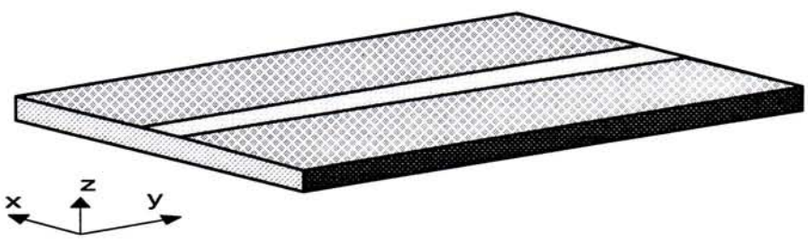

Figure 2.4 A slotline structure

2.4.1 Closed form of slotline

The slotline field contains six components: three electric components and three magnetic components. The longitudinal component of the electric field is very weak since the energy propagates between the two conductors. If the slot width W is much smaller than the free-space wavelength λ_o, the electric field across the slot may be represented by an equivalent line source of magnetic current, and then the far-field contains only three components: H_z, H_r and E_ϕ . At a distance r at least several times larger than W the longitudinal component of magnetic fields is given by [2.39]

$$H_z = AH_o^{(1)}(k_c r) \tag{2. 59}$$

and other field components

$$H_r = -\frac{j2\pi}{\lambda_g}\cdot\frac{1}{k_c^2}\cdot\frac{\partial H_z}{\partial r} = \frac{A}{\sqrt{1-(\frac{\lambda_g}{\lambda})^2}}H_1^{(1)}(k_c r) \tag{2. 60}$$

$$E_\phi = \frac{j\omega\mu}{k_c^2}\cdot\frac{\partial H_z}{\partial r} = -\frac{A\eta\frac{\lambda_g}{\lambda}}{\sqrt{1-(\frac{\lambda_g}{\lambda})^2}}H_1^{(1)}(k_c r) \tag{2. 61}$$

where $H_n^1(x)$ is the Hankel function of first kind of order n and argument x. The coefficient k_c ,of zero-order approximation, is

$$k_c = \frac{j2\pi}{\lambda}\sqrt{\frac{\varepsilon_r - 1}{2}} \tag{2. 62}$$

For large values of r, $H_0^{(1)}(j|r|)$ and $H_1^{(1)}(j|r|)$ may be expressed as

$$H(j|r|) = \frac{2}{\sqrt{j\pi|r|}}\exp(-|r| - j\frac{(2n+1)\pi}{4}) \tag{2. 63}$$

Therefore, if $k_c r$ is imaginary, the field will decay with distance r. Equation (2.62) shows that $k_c r$ is imaginary for the ratio λ_g/λ_0 is less than one. Hence a relative wavelength ratio less than unity is a sufficient condition to ensure transverse decay of the field. As λ_g/λ_0 is decreased, or the value ε_r increased, the ratio of decay becomes faster and fields become more tightly bound to the slot.

One accurate expression for the slotline wavelength with one percent accuracy is given as [2.40]:

$$\frac{\lambda_g}{\lambda_0} = -\left(\frac{0.11W}{h} + 0.077\right)\log\left(\frac{100h}{\lambda_0}\right) + \frac{0.104W}{h} + 0.507 \qquad (2.64)$$

provided that the following condition are fulfilled:

$$\varepsilon_r = 9.7$$

$$0.01 \le h/\lambda_0 \le \frac{0.25}{\sqrt{\varepsilon_r - 1}}$$

$$0.1 < W/h \le 1.0$$

where h and W are the thickness and the width of the slotline. λ_g is the guided wavelength on the slotline and λ_o is the free space wavelength.

Chapter Three

Implementation of FEM

The basic steps of a finite element analysis were outlined in chapter one. In chapter two, we discussed the theory of variational method combined with artificial boundaries to solve typical wave equations. In the current chapter, we will focus on the special slotline-bowtie junction. Details of the working procedures will be given to illustrate the implementation of finite element simulation of the ultra-wide band antenna.

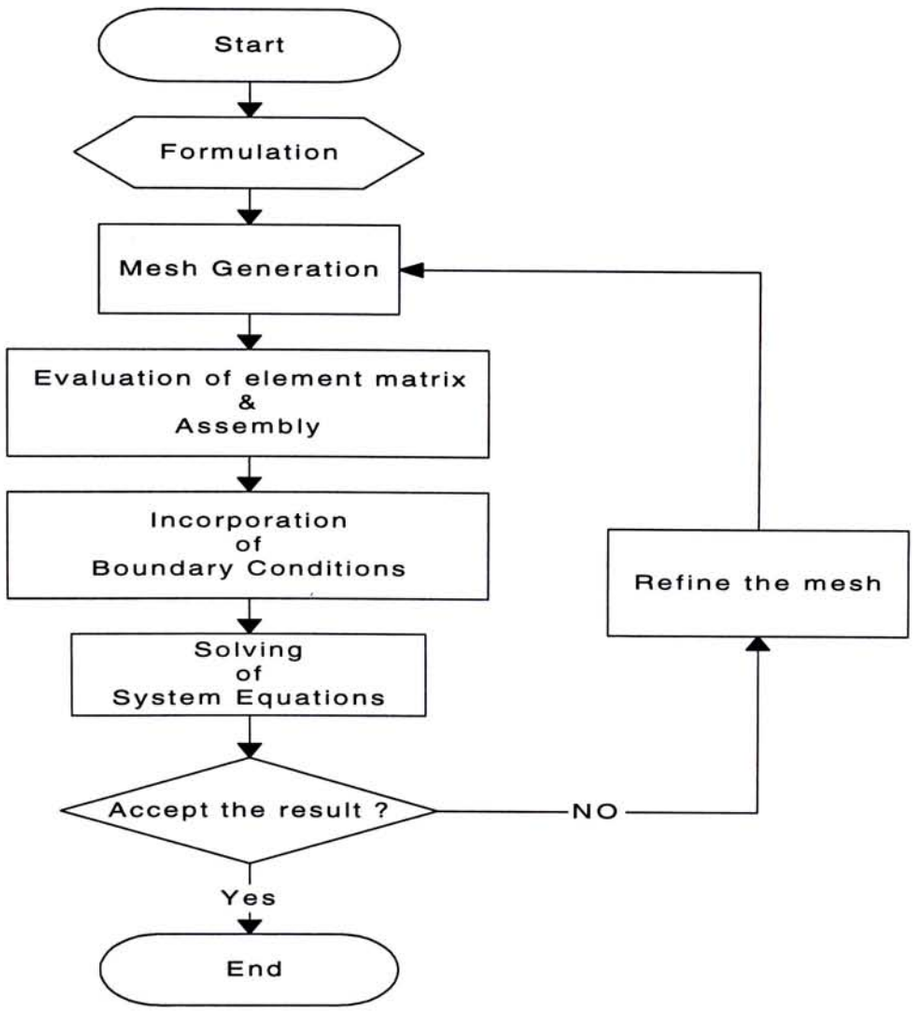

Figure 3. 1 Procedures of a typical finite element analysis

3.1 Formulation of element matrices

In a finite element simulation of the antenna, the bowtie-slotline junction was placed in a domain enclosed by a fictitious surface S_0. Inside the domain, the behavior of electromagnetic wave is governed by the vector wave equation,

$$\nabla \times \left[\ddot{\mu}_r^{-1} \cdot \left(\nabla \times \vec{E} \right) \right] - k_0^2 \ddot{\varepsilon}_r \cdot \vec{E} = -jk_0 Z_0 \vec{J} \qquad (3.1)$$

with the boundary conditions

$$\hat{n} \times \left[\ddot{\mu}_r^{-1} \cdot (\nabla \times \vec{E}) \right] + \boldsymbol{\mathcal{P}}(\vec{E}) = \vec{U}^{inc} \qquad \text{on } S_0 \qquad (3.2)$$

We assume that the media contains materials with diagonal dyadic relative permittivity $\ddot{\varepsilon}_r$ and permeability $\ddot{\mu}_r$, such that

$$(\ddot{\varepsilon})_r^T = \ddot{\varepsilon}_r \quad \text{and} \quad (\ddot{\mu}_r^{-1})^T = \ddot{\mu}_r^{-1} \qquad (3.3)$$

where $\boldsymbol{\mathcal{P}}(\vec{E})$ is a first order absorbing boundary condition. $\vec{U}^{inc}$ is a known vector for a given incident field. The functional is [3.1]:

$$F(\vec{E}) = \frac{1}{2} \iiint_{\Omega} \left[(\nabla \times \vec{E}) \cdot \ddot{\mu}_r^{-1} \cdot (\nabla \times \vec{E}) - k_0^2 \vec{E} \cdot \ddot{\varepsilon}_r \cdot \vec{E} \right] dV - \frac{1}{2} \iint_{S_0} [\vec{E} \cdot \boldsymbol{\mathcal{P}}(\vec{E})] dS$$

$$+ j\omega\mu_0 \iiint_{\Omega} \vec{E} \cdot \vec{J} dV + \iint_{S_0} [\vec{E} \cdot \vec{U}^{inc}] dS \qquad (3.4)$$

we rewrite the functional as

$$F(\vec{E}) = F_A(\vec{E}) + F_B(\vec{E}) + F_C(\vec{E}) + F_D(\vec{E}) \qquad (3.5)$$

where

$$F_A(\vec{E}) = \frac{1}{2} \iiint_{\Omega} \left[(\nabla \times \vec{E}) \cdot \ddot{\mu}_r^{-1} \cdot (\nabla \times \vec{E}) - k_0^2 \vec{E} \cdot \ddot{\varepsilon}_r \cdot \vec{E} \right] dV$$

$$F_B(\vec{E}) = -\frac{1}{2} \iint_{S_0} [\vec{E} \cdot \boldsymbol{\mathcal{P}}(\vec{E})] dS$$

$$F_C(\vec{E}) = j\omega\mu_0 \iiint_{\Omega} \vec{E} \cdot \vec{J} dV$$

$$F_D(\vec{E}) = \iint_{S_0} [\vec{E} \cdot \vec{U}^{inc}] dS \qquad (3.6)$$

Since we are working on radiation problem, we ignored the term $F_D(\vec{E})$ that is responsible for the scattering effect. We divide the whole domain Ω into M tetrahedral elements; the enclosed surface S_0 consists of N surface triangular elements. Consequently, the functional becomes a summation of M terms, each term corresponding to an element.

$$F(\vec{E}) = \sum_{e=1}^{M} F^e(\vec{E}^e)$$

$$= \sum_{e=1}^{M} F_A^e(\vec{E}^e) + \sum_{s=1}^{N} F_B^s(\vec{E}^s) + \sum_{e=1}^{M} F_C^e(\vec{E}^e) \qquad (3.7)$$

Next, we approximate the electric field within each element by selecting linear tetrahedral edge element

$$\vec{E}^e = \sum_{i=1}^{6} \vec{N}_i^e E_i^e = \{E^e\}^T \{\vec{N}^e\} = \{\vec{N}^e\}^T \{E^e\} \qquad e=1,2,\ldots,M \qquad (3.8)$$

where

$$\vec{N}_i^e = l_i^e (L_{i1}^e \nabla L_{i2}^e - L_{i2}^e \nabla L_{i1}^e) \qquad i=1,2,\ldots,6$$

$$L_j^e(x, y, z) = \frac{1}{6V^e}(a_j^e + b_j^e x + c_j^e y + d_j^e z) \qquad j=1,2,3,4$$

For the outermost surface, triangular surface edge element was employed

$$\vec{E}^s = \sum_{i=3}^{n} \vec{N}_i^s E_i^s = \{E^s\}^T \{\vec{N}^s\} = \{\vec{N}^s\}^T \{E^s\} \qquad s=1,2,\ldots,N \qquad (3.9)$$

where

$$\vec{N}_i^s = l_i^s (L_{i1}^s \nabla L_{i2}^s - L_{i2}^s \nabla L_{i1}^s) \qquad i=1,2,3$$

$$L_j^s = \frac{1}{2\Delta^s}(a_j^s + b_j^s x + c_j^s y) \qquad j=1,2,3$$

Exact expressions of the coefficients are listed in Appendix 1 and 2. Consequently, the imposition of stationarity to the functional yields

$$\boxed{\left\{\frac{\partial F(\vec{E})}{\partial \vec{E}}\right\} = \sum_{e=1}^{M}\left\{\frac{\partial F_A^e(\vec{E}^e)}{\partial \vec{E}^e}\right\} + \sum_{s=1}^{N}\left\{\frac{\partial F_B^s(\vec{E}^s)}{\partial \vec{E}^s}\right\} + \sum_{e=1}^{M}\left\{\frac{\partial F_C^e(\vec{E}^e)}{\partial \vec{E}^e}\right\} = \{0\}} \qquad (3.\ 10)$$

Next, we considered the partial differentiation of each term. First,

$$\begin{aligned} F_A^e(\vec{E}^e) &= \frac{1}{2}\iiint_e \left[(\nabla \times \vec{E}^e)\cdot \vec{\vec{\mu}}_r^{e^{-1}} \cdot (\nabla \times \vec{E}^e) - k_0^2 \vec{E}^e \cdot \vec{\vec{\varepsilon}}_r \cdot \vec{E}^e\right] dV \\ &= \frac{1}{2}\{E^e\}[A^e]\{E^e\} + \frac{1}{2}\{E^e\}[AA^e]\{E^e\} \end{aligned} \qquad (3.\ 11)$$

where

$$[A^e] = \iiint_e \{\nabla \times \vec{N}^e\}\cdot \vec{\vec{\mu}}_r^{e^{-1}} \cdot \{\nabla \times \vec{N}^e\}^T dV$$

$$[AA^e] = -k_0^2 \cdot \iiint_e \{\vec{N}^e\}\cdot \vec{\vec{\varepsilon}}_r^e \cdot \{\vec{N}^e\}^T dV$$

Therefore

$$\sum_{e=1}^{M}\left\{\frac{\partial F_A^e(\vec{E}^e)}{\partial \vec{E}^e}\right\} = \sum_{e=1}^{M}[A^e]\{E^e\} + \sum_{e=1}^{M}[AA^e]\{E^e\} \qquad (3.\ 12)$$

The second term,

$$F_B^s(\vec{E}^{sc}) = \frac{-1}{2}\iint_s \vec{E}^s \cdot \boldsymbol{\mathcal{P}}(\vec{E}^s)\, dA \qquad (3.\ 13)$$

The first order Absorbing Boundary Condition was employed, and the corresponding operator $\boldsymbol{\mathcal{P}}(\vec{E}^s)$ was

$$\boldsymbol{\mathcal{P}}(\vec{E}^s) = jk_0 \cos\theta_a \left[\hat{n} \times (\hat{n} \times \vec{E}^s)\right] \qquad (3.\ 14)$$

Thus the functional accounting for the fictitious surface was in the form

$$F_B^s(\vec{E}^s) = \frac{jk_0 \cos\theta_a}{2} \iint_s (\hat{n} \times \vec{E}^s) \cdot (\hat{n} \times \vec{E}^s) dA$$

$$= \frac{1}{2} \{E^s\}^T \left[(jk_0 \cos\theta_a) \iint_S \{\hat{n} \times \vec{N}^s\} \cdot \{\hat{n} \times \vec{N}^s\}^T dA \right] \{E^s\} \qquad (3.15)$$

it may take the matrix form

$$F_B^s(\vec{E}) = \frac{1}{2} \{E^s\}^T [B^s] \{E^s\} \qquad (3.16)$$

where

$$[B^s] = jk_0 \cos\theta_a \iint_S \{\hat{n} \times \vec{N}^s\} \cdot \{\hat{n} \times \vec{N}^s\}^T dS$$

So the sum of partial differentials is given as

$$\sum_{s=1}^{N} \left\{ \frac{\partial F_B^s(\vec{E}^s)}{\partial \vec{E}^s} \right\} = \sum_{s=1}^{N} [B^s] \{E^s\} \qquad (3.17)$$

Finally, the excitation part is

$$F_C^e(\vec{E}^e) = j\omega\mu_0 \iiint_e E^e \cdot \vec{J} dV \qquad (3.18)$$

Similarly, the summation of partial differentials is

$$\sum_{e=1}^{M} \left\{ \frac{\partial F_C^e(\vec{E}^e)}{\partial \vec{E}^e} \right\} = \sum_{e=1}^{M} \{C^e\} \qquad (3.19)$$

where

$$\{C^e\} = -j\mu_0\omega_0 \iiint_e \{\vec{N}^e \cdot \vec{J}\} dV$$

In summary, the stationarity of the overall functional

$$\left\{ \frac{\partial F(\vec{E})}{\partial \vec{E}} \right\} = \{0\} \qquad (3.20)$$

leads to a system of equations

$$\sum_{e=1}^{M}[A^e]\{E^e\}+\sum_{e=1}^{M}[AA^e]\{E^e\}+\sum_{s=1}^{N}[B^s]\{E^s\}=-\sum_{e=1}^{M}\{C^e\} \tag{3.21}$$

where

$$[A^e]=\iiint_e\{\nabla\times\vec{N}^e\}\cdot\vec{\mu}_r^{e^{-1}}\cdot\{\nabla\times\vec{N}^e\}^T dV \tag{3.22}$$

$$[AA^e]=-k_0^2\cdot\iiint_e\{\vec{N}^e\}\cdot\vec{\varepsilon}_r^e\cdot\{\vec{N}^e\}^T dV \tag{3.23}$$

$$[B^s]=jk_0\cos\theta_a\iint_s\{\hat{n}\times\vec{N}^s\}\cdot\{\hat{n}\times\vec{N}^s\}^T dA \tag{3.24}$$

$$\{C^e\}=-j\mu_0\omega_0\iiint_e\{\vec{N}^e\cdot\vec{J}\}dV \tag{3.25}$$

In fact, it is possible to combine all the element matrices $[A^e]$ $[AA^e]$ and $[B^s]$ to form a single matrix, say $[K]$. On the other hand, all $\{C^e\}$ are put together to form $\{RHS\}$.

$$[K]\{E\}=\{RHS\} \tag{3.26}$$

the global matrix is a square matrix of size, where the size equals the total number of edges in the domain. The details of assembly will be given in section (3.3).

There is a simpler alternative way of excitation. One can resort to a simple gap source, in which the electric field of an edge corresponding to the source of excitation was defined *a priori.*

3.2 Mesh Generation

Domain discretization is a vital but difficult procedure in a finite element analysis. In real engineering problems, it usually involves several thousands of elements to model complex three-dimensional objects. The need of replacing manual data entry motivates the development of automatic mesh generation that becomes a hot research topic. [3.2] [3.3]

[3.4]. An ideal mesh consists of equally spaced mesh with local refinement at certain regions. The performance of mesh discretization affects the accuracy of the final mesh. Thus, it remains a challenge for researchers to improve the mesh quality and accelerate the process [3.5][3.6][3.7].

In general, triangle (2D) and tetrahedron (3D) are widely used in automatic mesh generation because of their flexible structure. There are a large number of ways of triangulating an arbitrary set of points on a plane, however, the difference of lengths in each triangle should be minimized in a good mesh. In 1934, Delaunay proved that there exists a unique triangulation which maximizes the sum of the smallest angles in the grid. The Delaunay Triangulation and its variants are now commonly employed in mesh generation process in many commercial software packages. But the algorithm is difficult to implement, especially in three-dimensional space. The primary objective of mesh discretization for our project is to properly model the slotline-bowtie junction. Instead of following the Delaunay algorithm, we developed a simple method for this investigation. We noticed that the junction is well modeled with a special arrangement of rectangular boxes. (Fig. 3.2b).

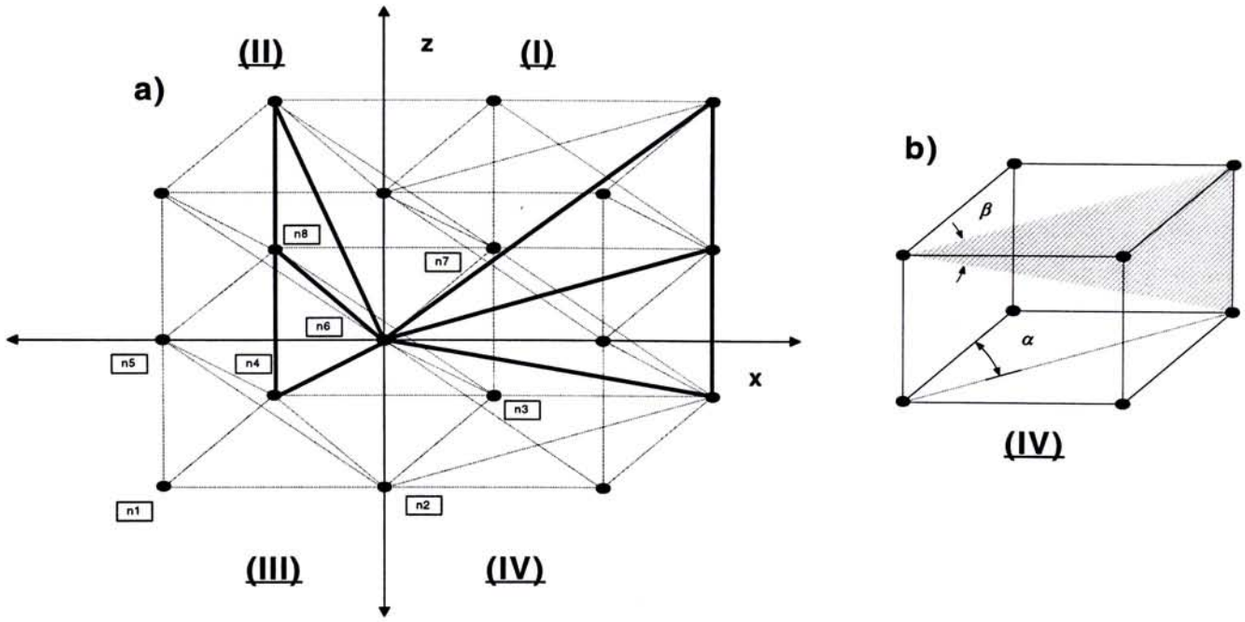

Figure 3. 2 Division of the domain a)The bowtie structure is modeled by a rectangular mesh.
b) Flare angles (α,β) can be adjusted by the lengths of the box.

We briefly outline the algorithm of discretization as below. The entire domain Ω is divided into four quadrants filled with boxes. There are nineteen edges associated with each box and six tetrahedrons inside. In Appendix 3, the arrangement of edges and tetrahedrons in each quadrant are given. At the end of the process, information of all node coordinates and the connectivity array are available. At the end of the process, the output must contain the following information:

1) Vertex Positions

   a) Coordinates of four nodes of each tetrahedral element:
   $X(e,i)$, $Y(e,i)$, $Z(e,i)$, $i=1,2,3,4$ $e=1,2,...,M$

   b) Coordinates of three nodes of each tetrahedral surface:
   $XS(e,j)$, $YS(e,j)$, $ZS(e,j)$, $j=1,2,3,4$ $s=1,2,...,N$

2) Connectivity Array[1] :

   a) Volume Connectivity Array:
   $NE(i,e)$, $i=1,2,...,6$, $e=1,2,....M$

   b)Surface Connectivity Array:
   $NS(j,s)$, $j=1,2,...,6$ $s=1,2,....M$

---

[1] *Remark:* Connectivity array contains the relationship between local and global numbering of each edge. For example, in an volume element $\Im$, the local edge 2 corresponding to global number $\Im$,then we have $\Im = NE(\aleph,2)$

Element	Local edge					
e	1	2	3	4	5	6
⋮	⋮	⋮	⋮	⋮	⋮	⋮
$\aleph$	⋮	$\Im$	⋮	⋮	⋮	⋮
⋮	⋮	⋮	⋮	⋮	⋮	⋮

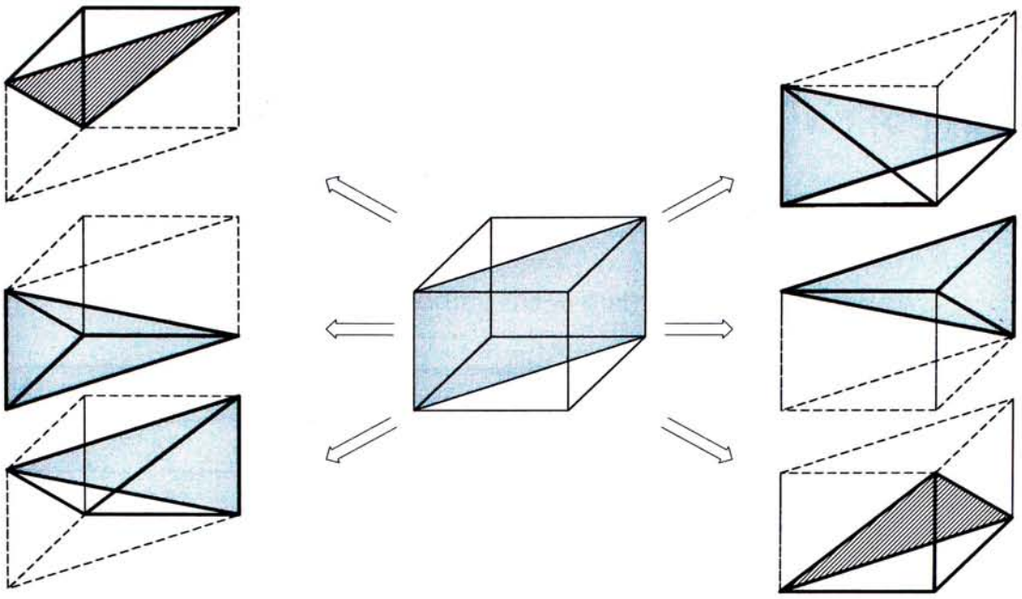

Figure 3. 3 Cutting of a box into six tetrahedrons

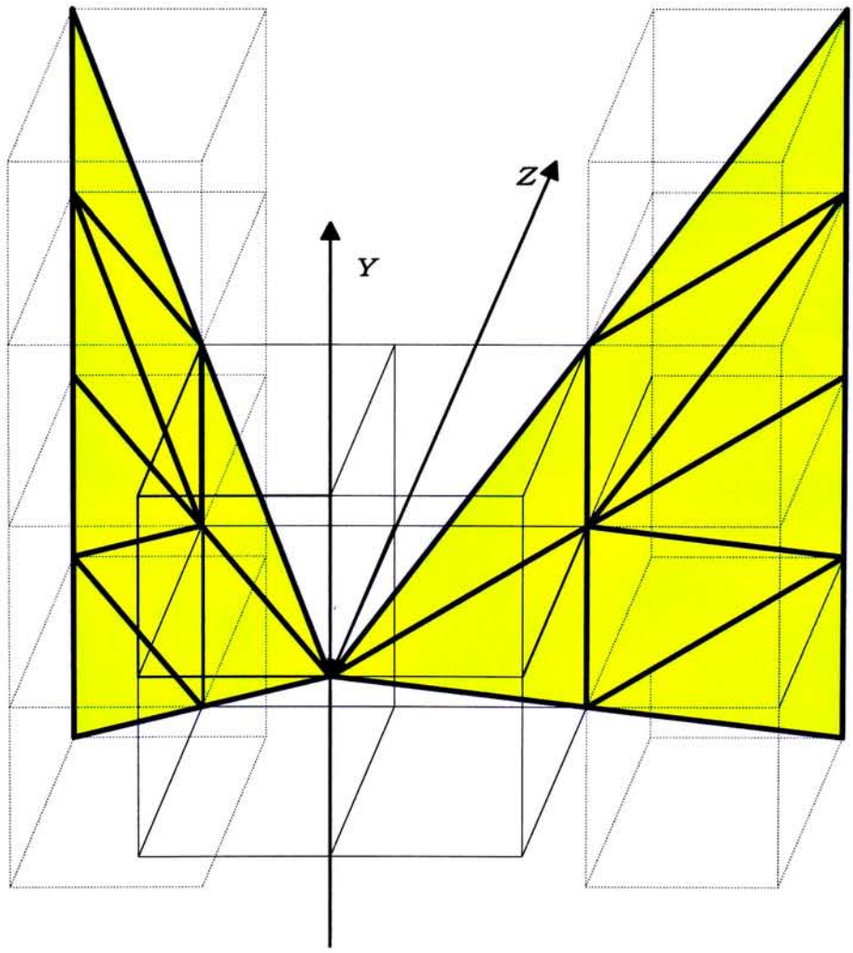

Figure 3.4 The slotline-bowtie junction in a rectangular mesh

3.3 Assembly

In finite element method, matrix entries ($[A^e]$,$[AA^e]$,$[B^s]$ and $\{C^e\}$) are computed element by element. Finally, they are put together to form an overall matrix equation $[K]\{\phi\}=\{RHS\}$. The general rule for adding these matrices are listed below:

Element matrix entry	*Location added to*
A_{ij}^e	$K_{NE(i,e),NE(j,e)}$
AA_{ij}^e	$K_{NE(i,e),NE(j,e)}$
B_{ij}^s	$K_{NS(i,e),NS(j,e)}$
C_i^e	$RHS_{NE(i,e)}$

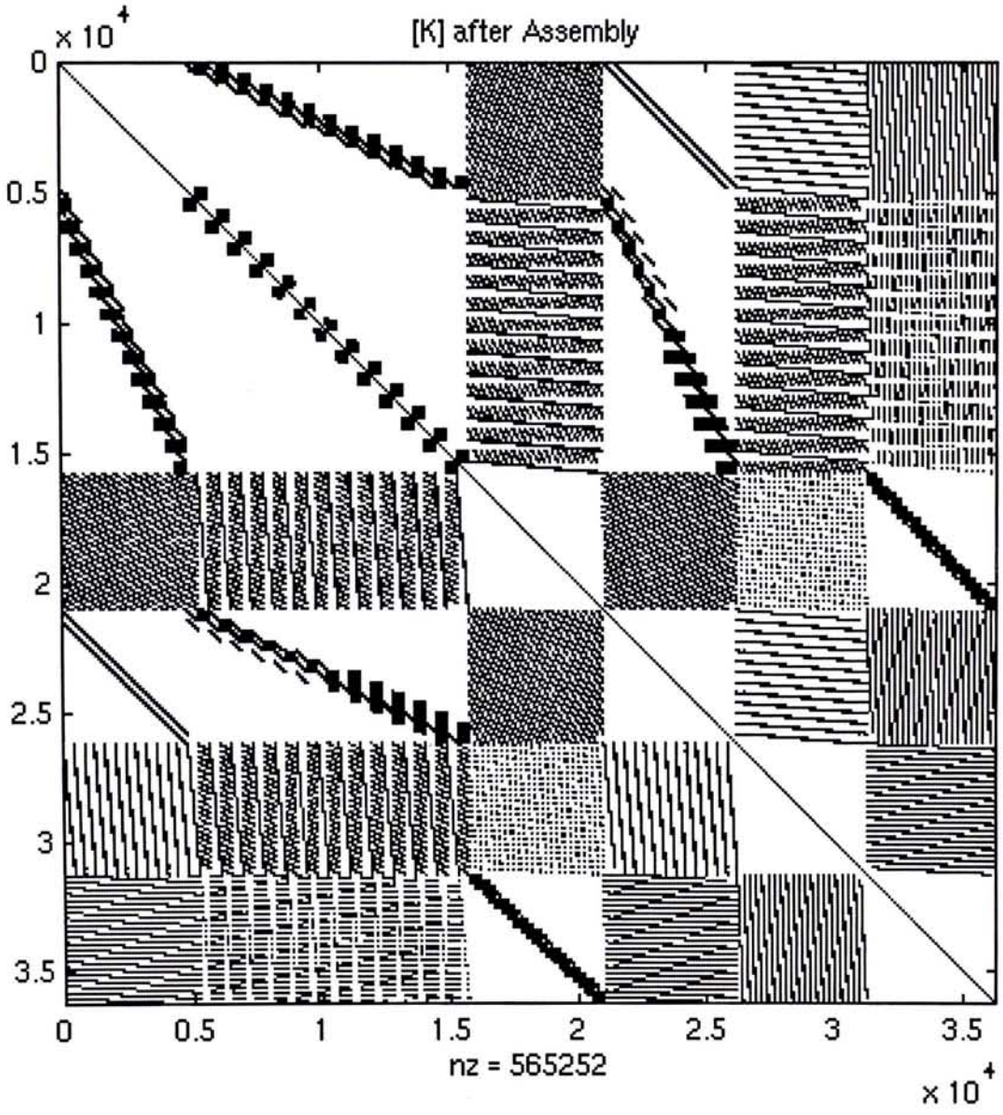

Figure 3.5 System matrix [K] after assembly.

3.4 Incorporation of Boundary Conditions

The slotline consists of two metal plates on the top of dielectric material. Also the vertical bowtie are made of metal. Since the tangential field on the perfect conductor is exactly zero. Thus, the edge on the metal surface must be set to zero before solving the matrix. Suppose there are N_I edges residing on the metal surface, we store the global edge numbers in a vector called "metal_position(i)". The imposition of the boundary condition can be accomplished simply by setting

$K_{\text{metal\_position(i), metal\_position(i)}} = 1$ $\quad$ $K_{\text{metal\_position(i),j}} = 0$ $\quad$ $RHS_{\text{metal\_position(i)}} = 0$

for $\quad i=1,2,3,...,N_I \quad$ & $\quad j \neq$ metal_position(i)

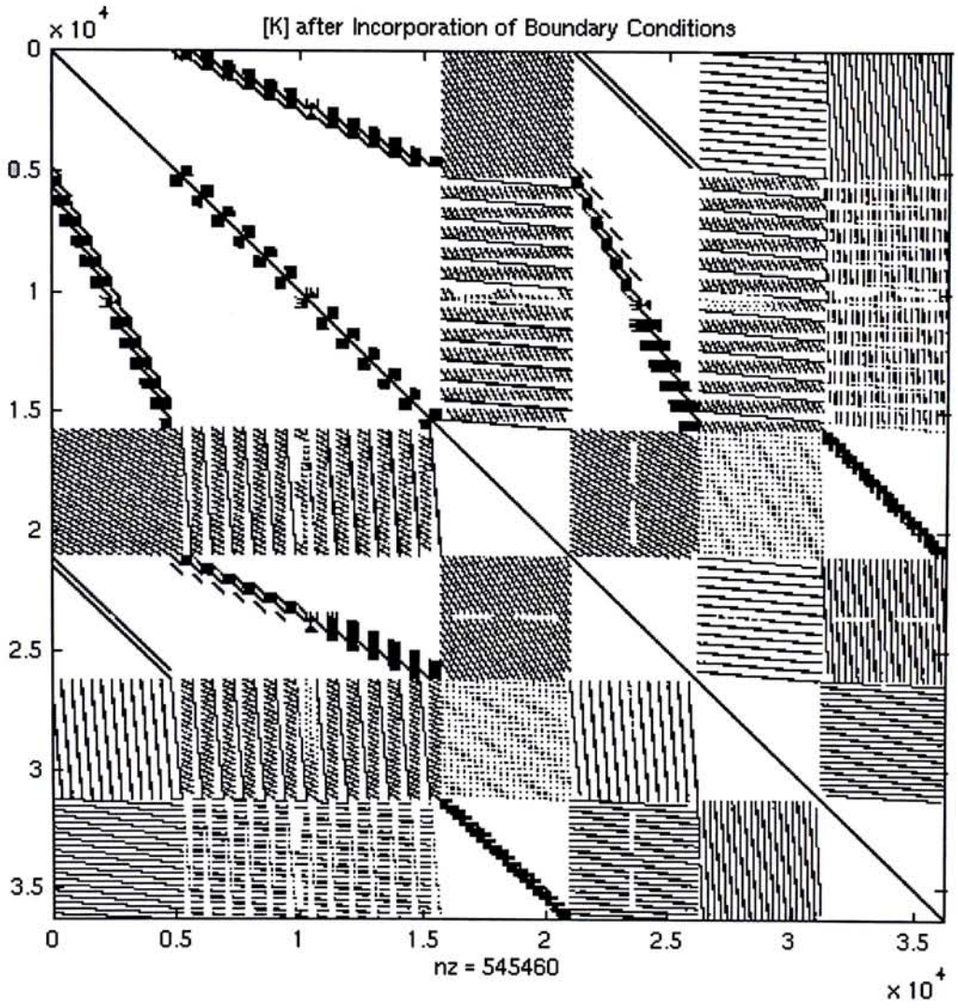

Figure 3. 6 System matrix after incorporation of boundary conditions

3.5 Solution of the system of equations

The size of matrix can be very large: tens of thousand. In a full matrix solver, all the matrix entries are stored and involved in the solving. It may take more than 150 Mbytes of RAM and seven hours to solve a matrix of size 5000 x 5000. However, some sophisticated solver can handle the same problems within half an hour using 30 Mbytes of RAM only. The latest version of MATLAB 5.1 add some functions specifically for sparse matrix to fully utilize the advantage of sparsity.

Before solving the matrix, reordering was carried out to make its Cholesky , LU, or QR factors sparser. A good column permutation of the matrix [K] will take less time and storage than computing the original matrix [3.8]. In particular, the minimum degree of ordering is selected because it usually leads to better sparsity factor than most other ordering methods[3.9]. Since the operator of the vector wave equation is positive and self-adjoint, the overall system of equations should be symmetric and positive definite. As a result, Cholesky factorization is used to solve the matrix problems because it is most efficient for symmetric positive definite matrix. .

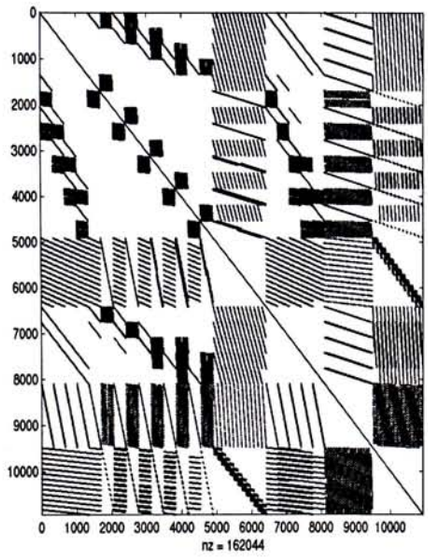

Figure 3. 7 Original matrix

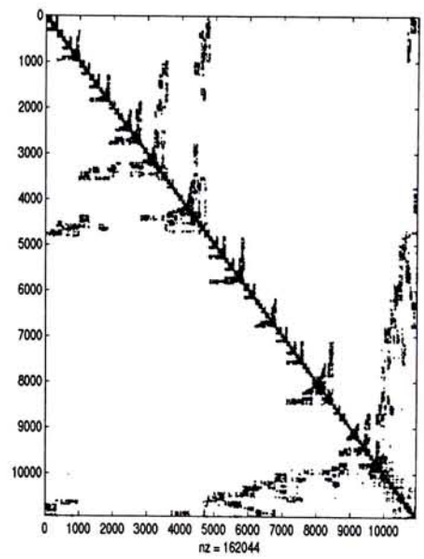

Figure 3. 8 After minimum degree of ordering

3.6 Code Implementation

In the previous sections, we discussed the application of variational principle and artificial boundaries to the slotline-bowtie junction. A FORTRAN program was developed based on the theory. The code structure is fairly simple, it consists of a main program and a collection of subroutines. Main body serves as a control unit which calls subroutines whenever necessary. Moreover, declaration and initialization for variables and output of results are done in the main body. A brief description of the function of each subroutine is listed below.

1) MESH: Mesh discretization is done in the subroutine. Vertex coordinates of each element and connectivity array are the final result of the process.

2) V_M: This subroutine has two functions. First, it evaluates and assembles the element matrices of all elements to form a system of equations. Second. it forms the vector of excitation.

3) PML_TEMP: This subroutine defines the numerical value of material tensor for PML layer.

4) VOLUME: Calculation of element matrices $\left[A^e\right]\left[AA^e\right]$.

5) EXCITATION: Element corresponding to excitation are selected to evaluate the C_VECTOR.

6) ASSEMBLY_A: This subroutine is called by anther subroutine VOLUME. Coefficient of each matrix is placed in the specific position of the overall system matrix.

7) ASSEMBLY_C: Similar to ASSEMBLY_A, but this is called by subroutine EXCITATION and is only responsible for the excitation vectors.

8) SURFACE: This accounts for the outermost surface. It evaluates surface element matrices and adds these components to the overall system of equations.

9) ASSEMBLY_B: Called by SURFACE to assemble the surface element matrices to the overall systems of equation.

10) BOUNDARY_CONDITION: Set zero to the edges on the metal surface.

11) SOLVER: The system of equations $[K]\{E\} = \{RHS\}$ is solved by MATLAB matrix solver.

```
C_____________________________________________________
c          Finite element Analysis
c                    of
c          Bowtie-Slotline Junction
C_____________________________________________________
c
c ******** Declaration of variables
      :
      :
c ******** Preparation of Data
      :
           :
c ******** Domain Discretization
      call MESH

c ******** Evaluation of element matrices
c --- (Volume Element matrices)
      call V_M

c --- (Surface Element matrices)
           call SURFACE

c ******** Imposition of boundary conditions
           call BOUNDARY_CONDITION

c ******** Solving the System of equations
      call SOLVER

c ******** Output of result
           :
      :

      END
```

Figure 3.5 Structure outline of the FORTRAN program

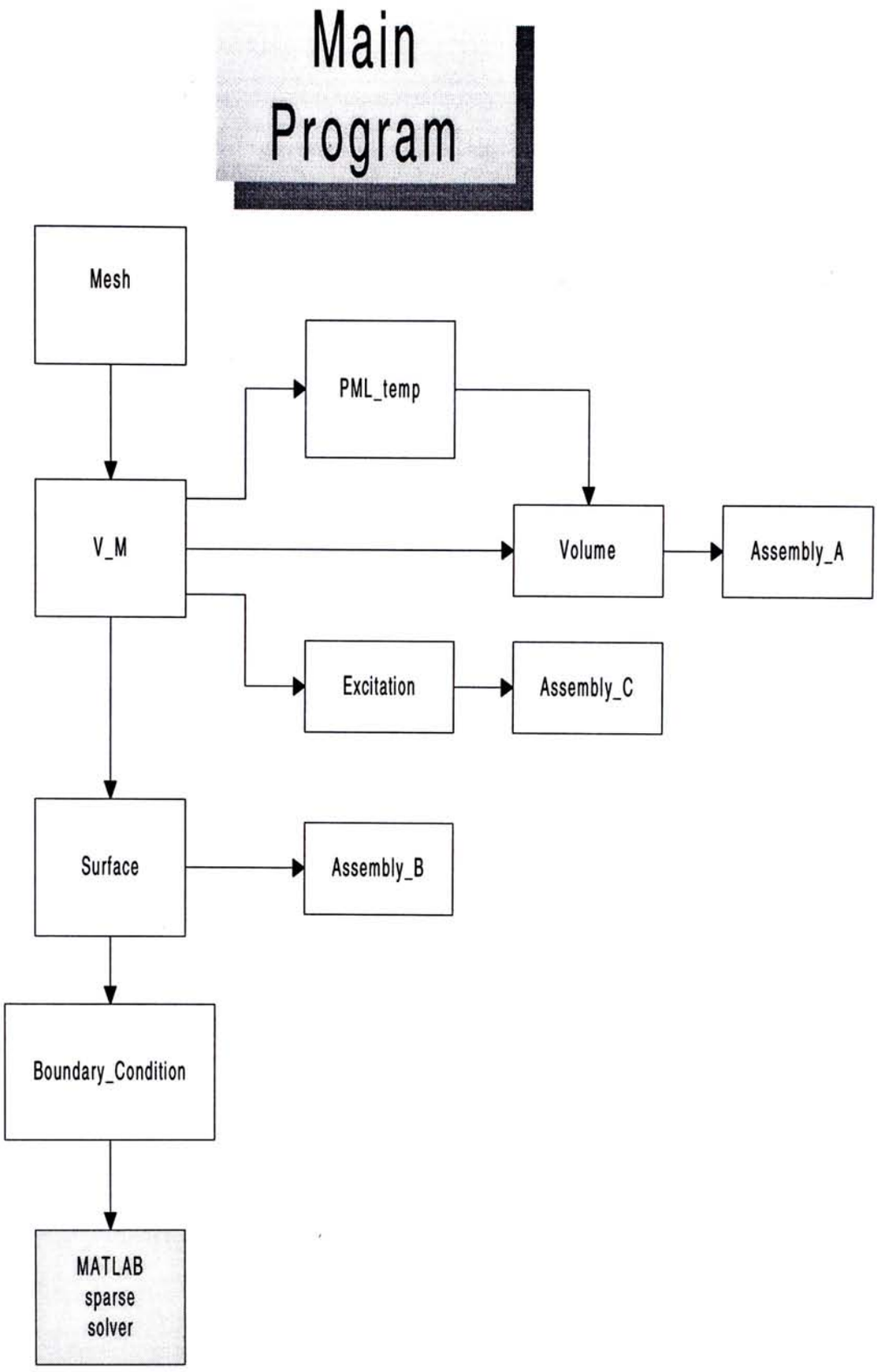

Figure 3. 6 List of subroutines in the FORTRAN code

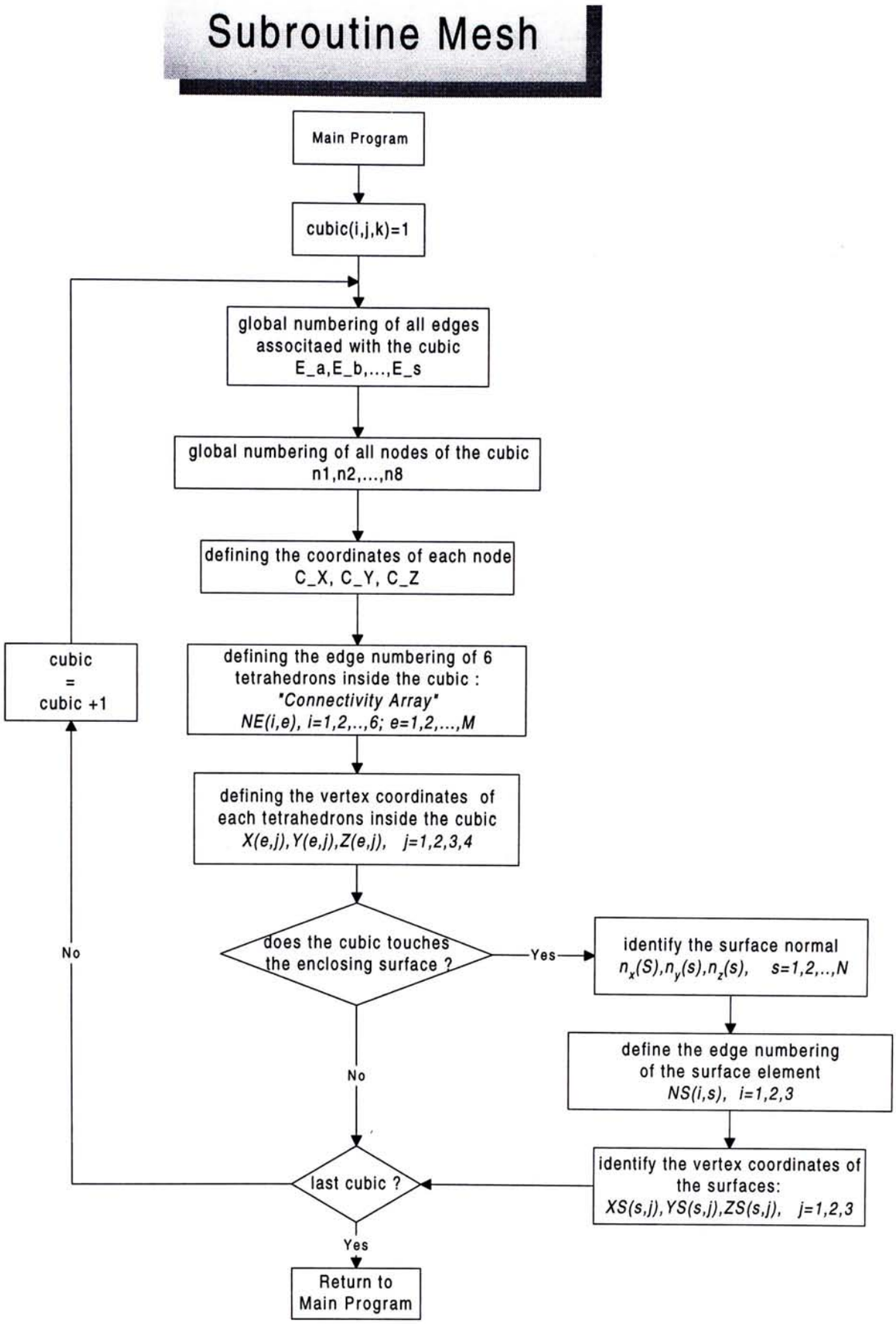

Figure 3. 7 Flowchart of subroutine MESH

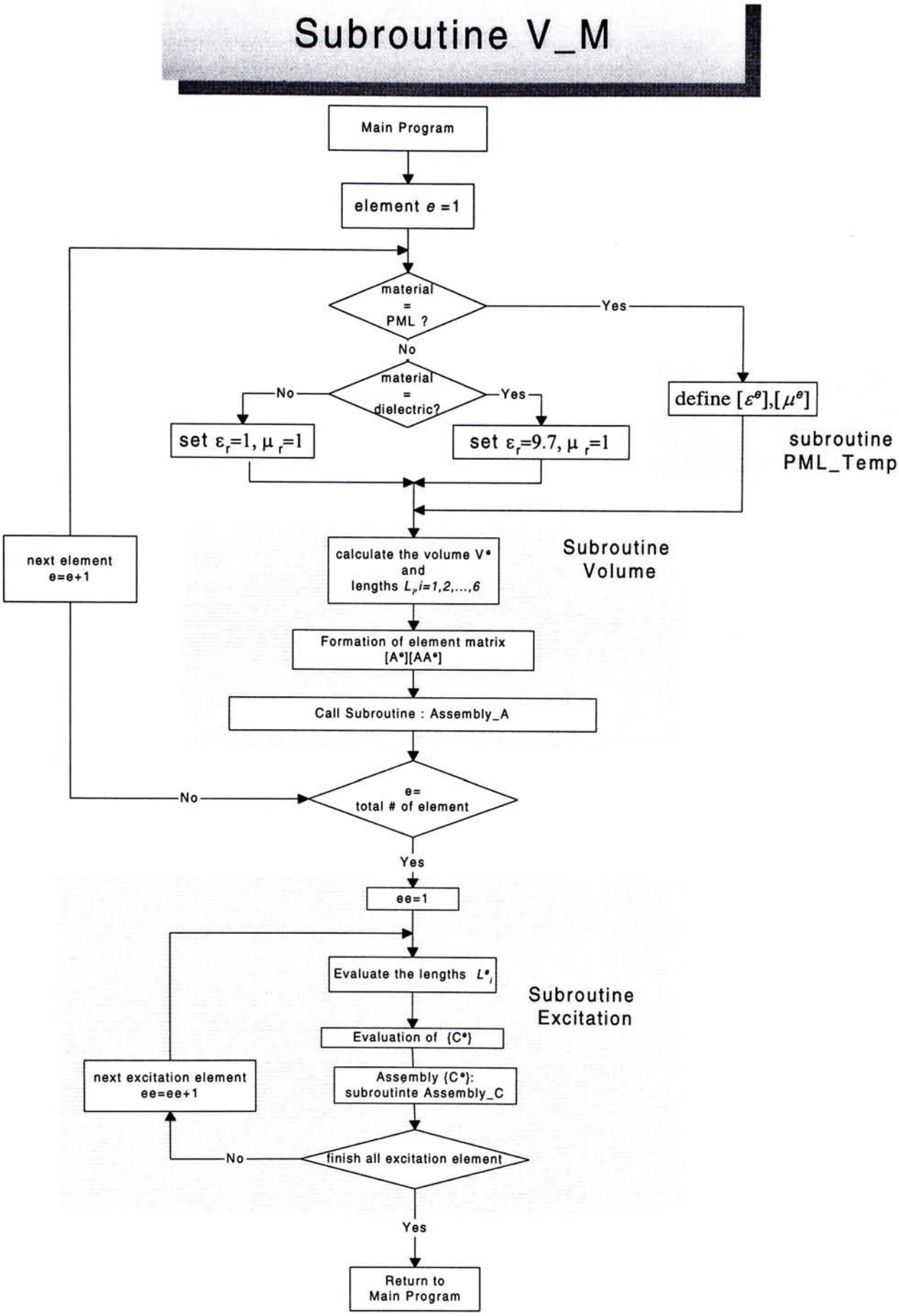

Figure 3. 8 Flowchart of subroutine V_M

Subroutine Surface

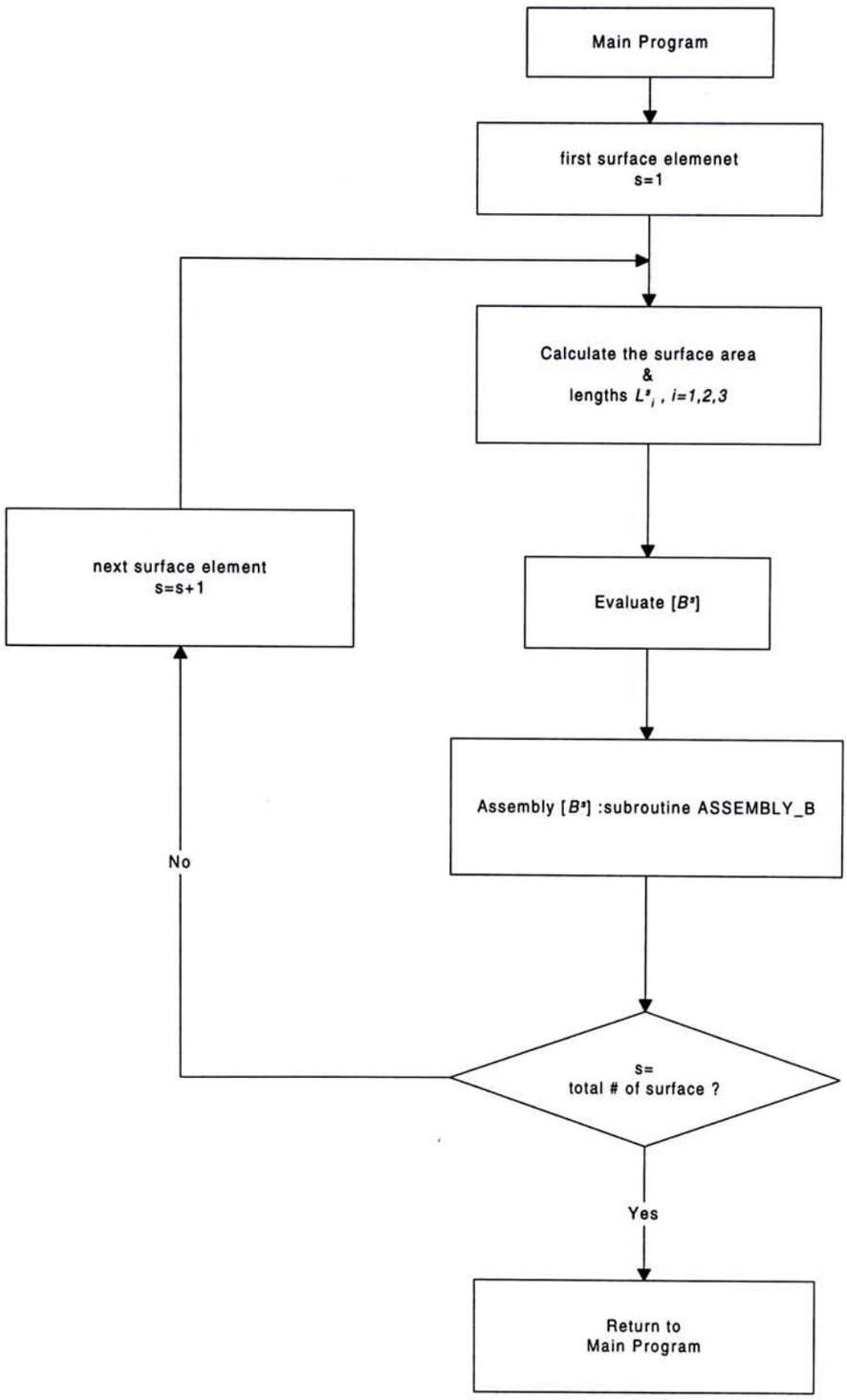

Figure 3. 9 Flowchart of subroutine SURFACE

Chapter Four

Finite Element Simulations

In this project, we developed a finite element program in FORTRAN to simulate the complicated slotline-bowtie junction, as shown in Figure 4.1. Since the slotline-bowtie junction can be treated as a combination of slotline and a tapered opening with bowtie structure. It is advantageous to start the analysis with simple slotline. We examined the field pattern of a slotline with finite length. Then we increased the width of the slotline and examined the field distribution of the taper structure. Finally, we combined the open slotline with a pair of vertical bowtie opening to form the slotline-bowtie junction.

The operating frequency is selected to be 40GHz throughout the research. First order ABC was used to enclose the whole domain and PML is applied to selective surface. The relative permittivity of the dielectric is 9.70. The width and thickness of the slotline are 0.1mm and 0.6mm respectively. In our finite element analysis, the slotline-bowtie hybrid was excited by a simple gap source, in which the electric field of the corresponding edge was defined in advance.

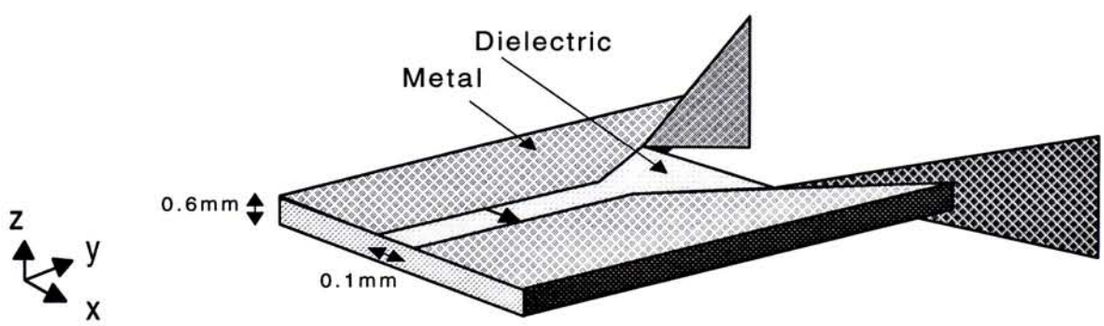

Figure 4. 1 Slotline-bowtie junction

4.1 Slotline

We started our simulation with a slotline of finite length. Figure 4.2 shows the problem setup for the slotline. The excitation point was located at the mid-point of the slotline. In Figure 4.3, as we expected, a standing wave pattern was observed clearly on the slotline plate level along Line 2. Peak value of the standing wave decreases as the distance from the centre increase. The standing wave was terminated at both ends and the magnitude of electric fields dropped rapidly to almost zero in the air. Along Line 1, we observe a strong and narrow peak at the centre of the slot. Along Line 3, we observed the field concentrated on the slotline plate level. These results agree with fundamental slotline theory as described in section 2.4. According to (2.65), the slotline wavelength is 3.2867 mm. In our simulations, the average wavelength obtained is 3.32 mm, as shown in Figure 4.4, where the half wavelength standing wave cycles are measured. The percentage error is about 0.9 %. In fact, better accuracy of the result is possible if we use a finer mesh.

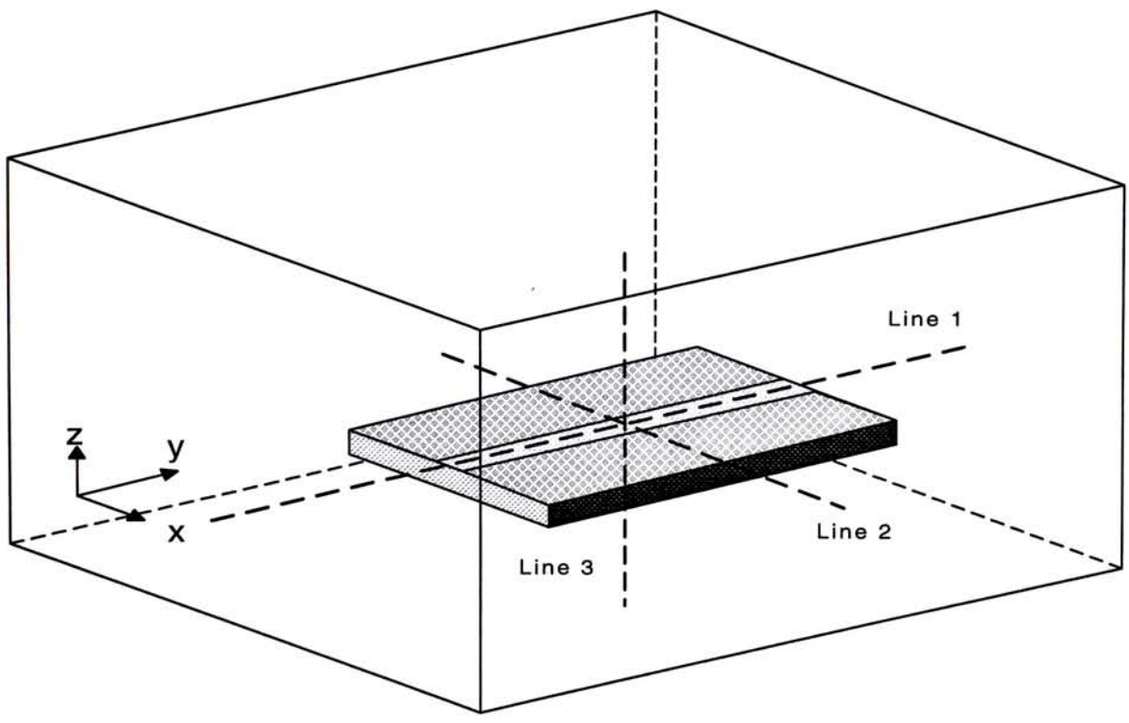

Figure 4. 2 A slotline structure

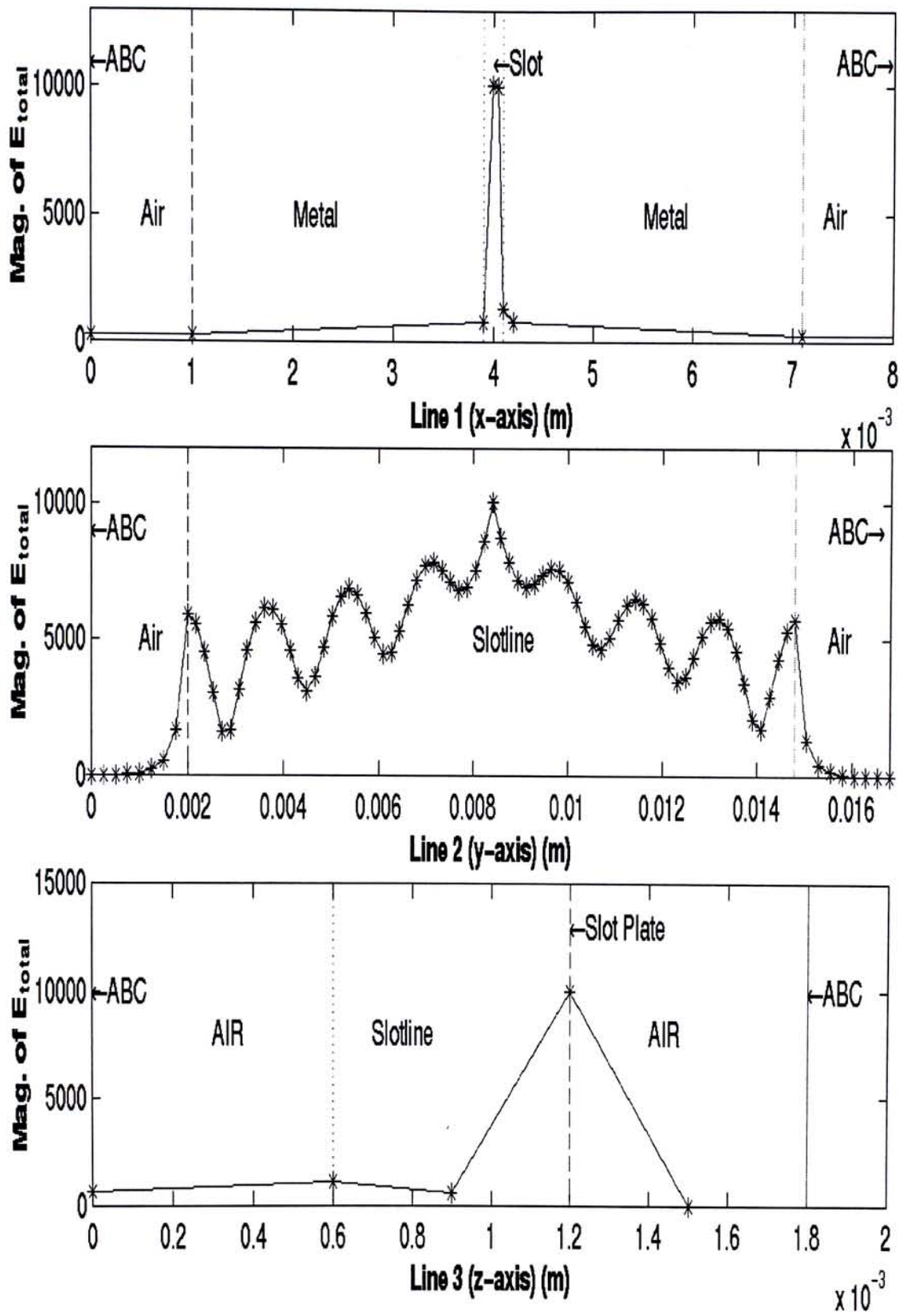

Figure 4. 3 Distribution of electric field of a slotline

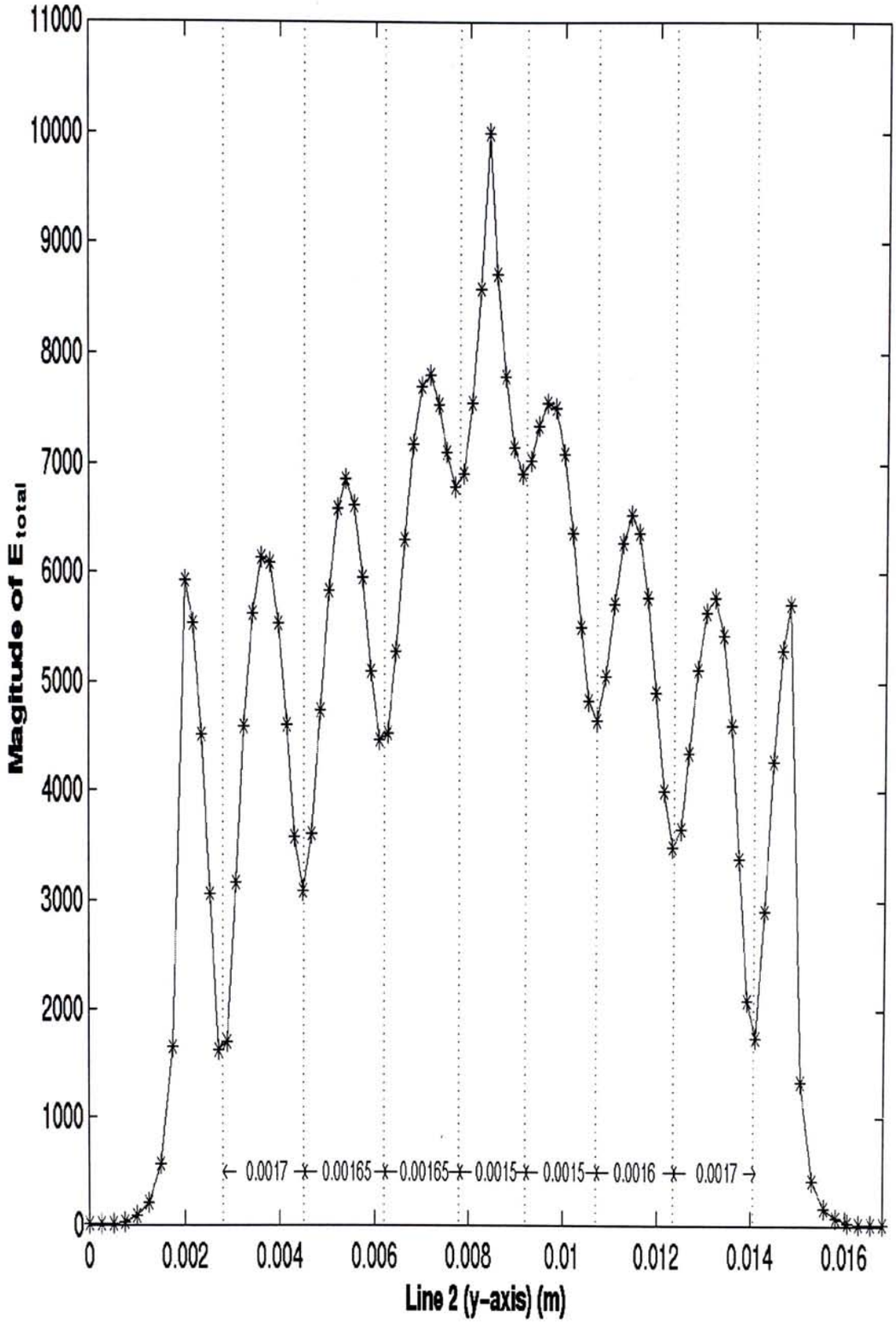

Figure 4. 4 Half wavelength measurements of the slotline

4.2 Artificial Boundary of the domain

In this section, we will discuss the performance of two kinds of artificial boundary of the domain. In an accurate solution, the reflection due to the artificial terminating boundary should be as little as possible.

As a first step, the first order Absorbing Boundary Condition (ABC) was used alone to terminate all the outgoing waves, as shown in Figure 4.5. A horizontal gap excitation was placed at the mid-point of the slotline. The end of the slotline is directly connected to a first order ABC. The standing wave humps show that some reflection exists at the boundary. The characteristic slotline field distribution is shown in the vertical and horizontal plots as well.

Next we look at a slotline with open termination at either end. The separation between the end of the slotline and the ABC was less than 1/3 λ_o. In Figure 4.6, four different "angles of perfect absorption", as measured from boresight (0°, 22.5°, 45° and 60°), of the ABC were tested. Peaks of the standing wave for each absorption angle were located exactly at the same positions. However, we observed that the smaller the angle of perfect absorption, the smaller the standing wave ratio. This is expected because the strongest radiation from a slotline will reach the ABC along the boresight direction.

In addition, we also found that, at 60° ABC, the third peak from centre was higher than second. In other cases, the peak values decrease as a function of the distance from the centre. Since the perfect absorbing angle was the only parameter different in this series of test, we may conclude that the reflection from the ABC interferes with the field in the slotline. For this reason, the perfect absorbing angle

should be set to zero degree. As mentioned before, this is because the main outgoing field should be normal to the ABC due to symmetry.

In the next step, we put Perfectly Matched Layer (PML) between the slotline and the ABC to test the effect of the PML. A very small air gap (0.2mm) was left between the slotline and PML. In Figure 4.7, we observed that the addition of PML did not cause large reflection even though the PML was placed so close to the slotline. Moreover, the field inside the PML decayed more rapidly than that in the air. It was evident that PML was working quite well to absorb the outgoing electromagnetic waves.

It is possible to improve the absorption power of PML by careful selection of the parameters in the PML. In the following series of simulation, the slotline penetrates the PML, reaching up to the ABC termination. The portion of PML penetrated by the dielectric section of the slotline has α = 9.7, corresponding to the dielectric constant of the slotline. In ideal case, the amplitudes should decrease monotonically and no standing wave should be observed. Practically, it was difficult to eliminate all reflection at the domain boundary. It is therefore desirable to reduce the variation of amplitude in the slotline. In Figure 4.8, we applied 8 layers of PML and kept δ_{max}=1.0, only varying the real part(α) of the PML. At α=8.0/9.7 and α=11.0/9.7, strong standing waves were formed in both cases. A significantly better result was found at α = 1.

In Figure 4.9, we fixed the real part and the number of layers of PML. For different δ_{max}, the peak values were quite different. It turned out that the reflection can be minimised by changing the value of δ_{max} and the best result was obtained by setting δ_{max} = 0.8. However, it should be note that too large a value of δ_{max} may lead

to an ill-conditioned matrix. More works should be done to optimise the value of imaginary part.

In addition, we found that the absorption of PML changed when we varied the number of layers in the PML, as shown in Figure 4.10. Surprisingly, 4 layers of PML is best in this case. 8 layers is worst. 12 layers PML was better than 8 layers, but not as good as 4 layers. Therefore, increasing the number of layer in PML do not always guarantee better result.

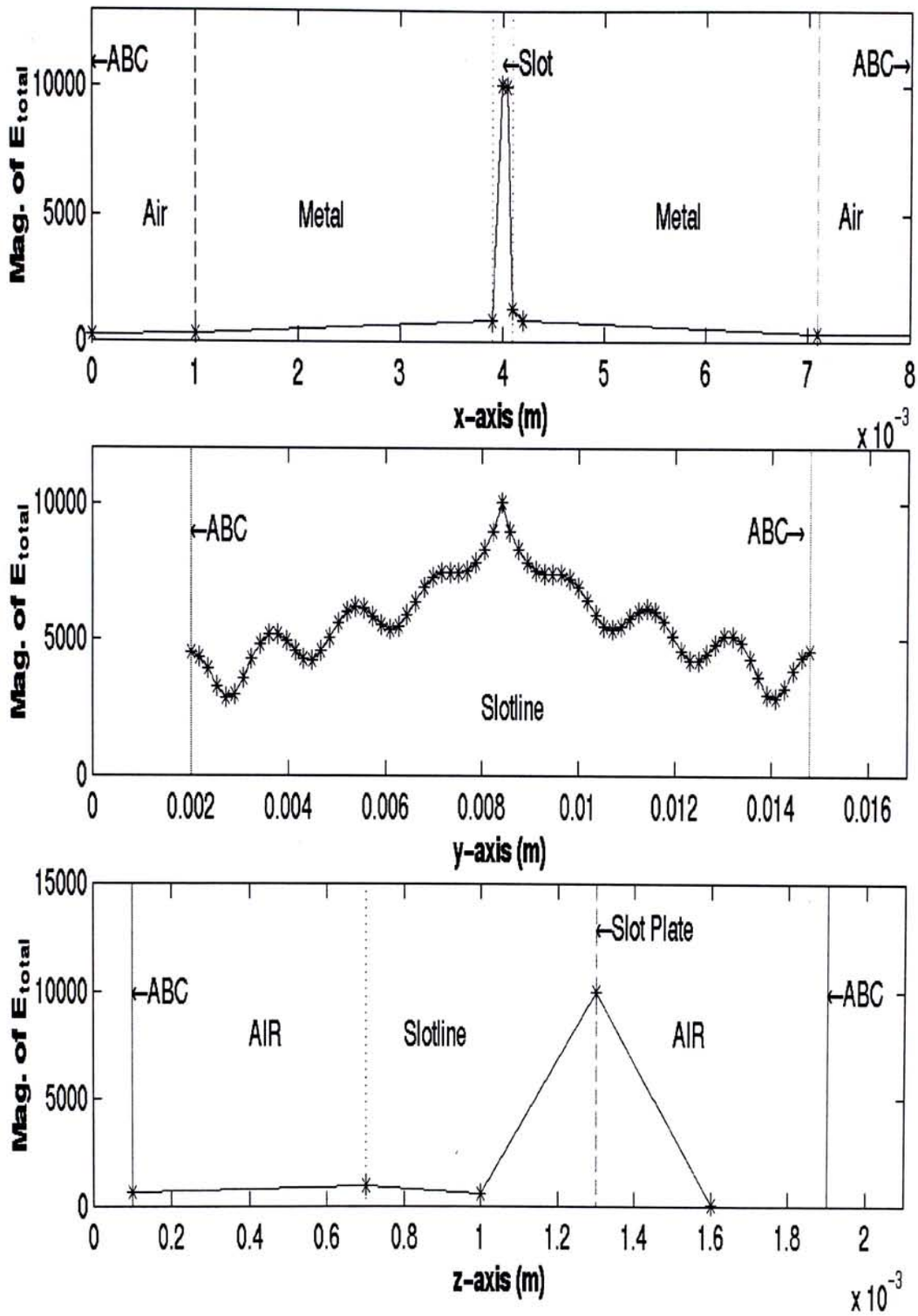

Figure 4. 5 Distribution of electric fields in a slotline

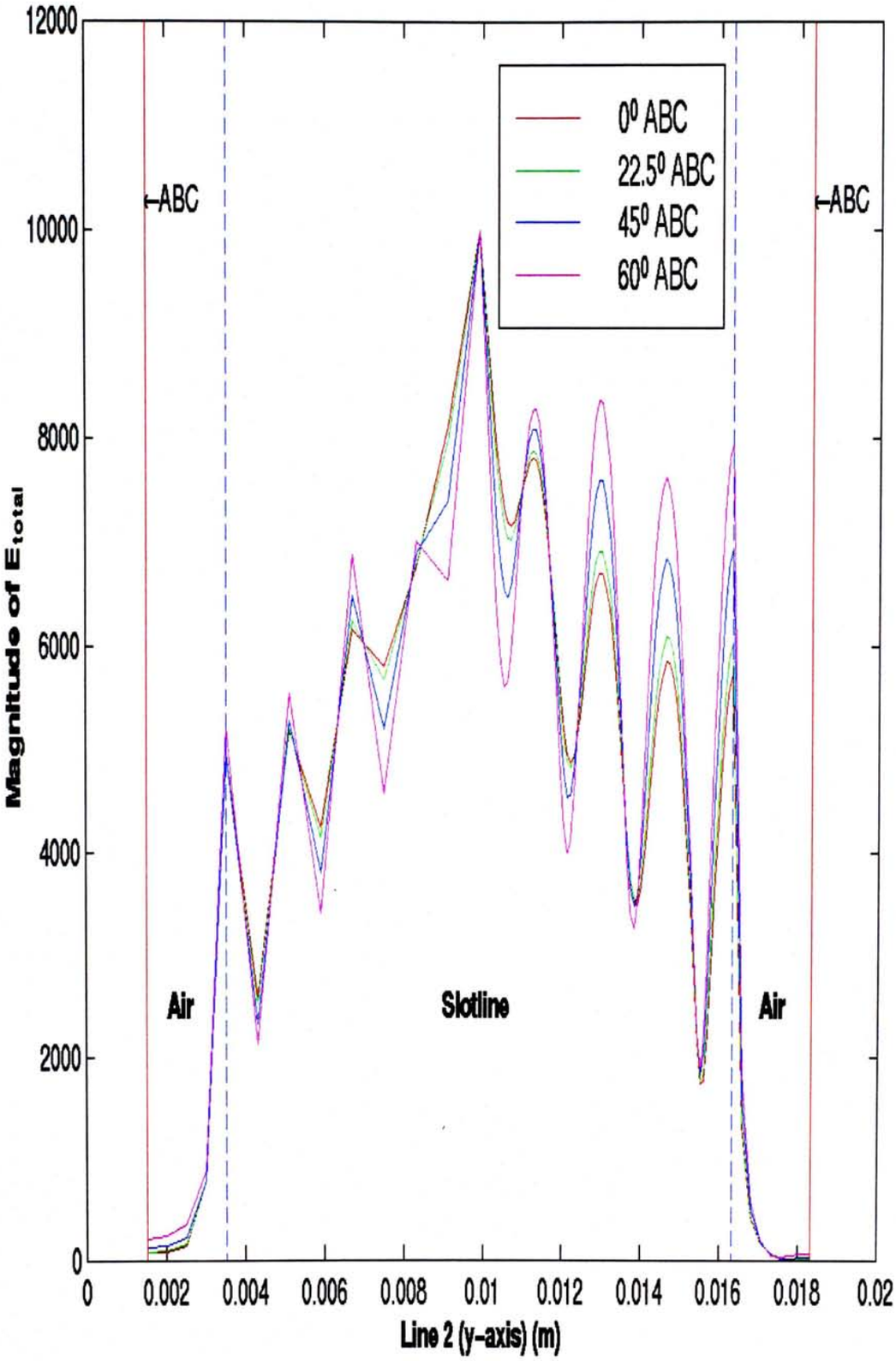

Figure 4. 6 Standing wave pattern of slotline for different perfect absorbing angles of ABC

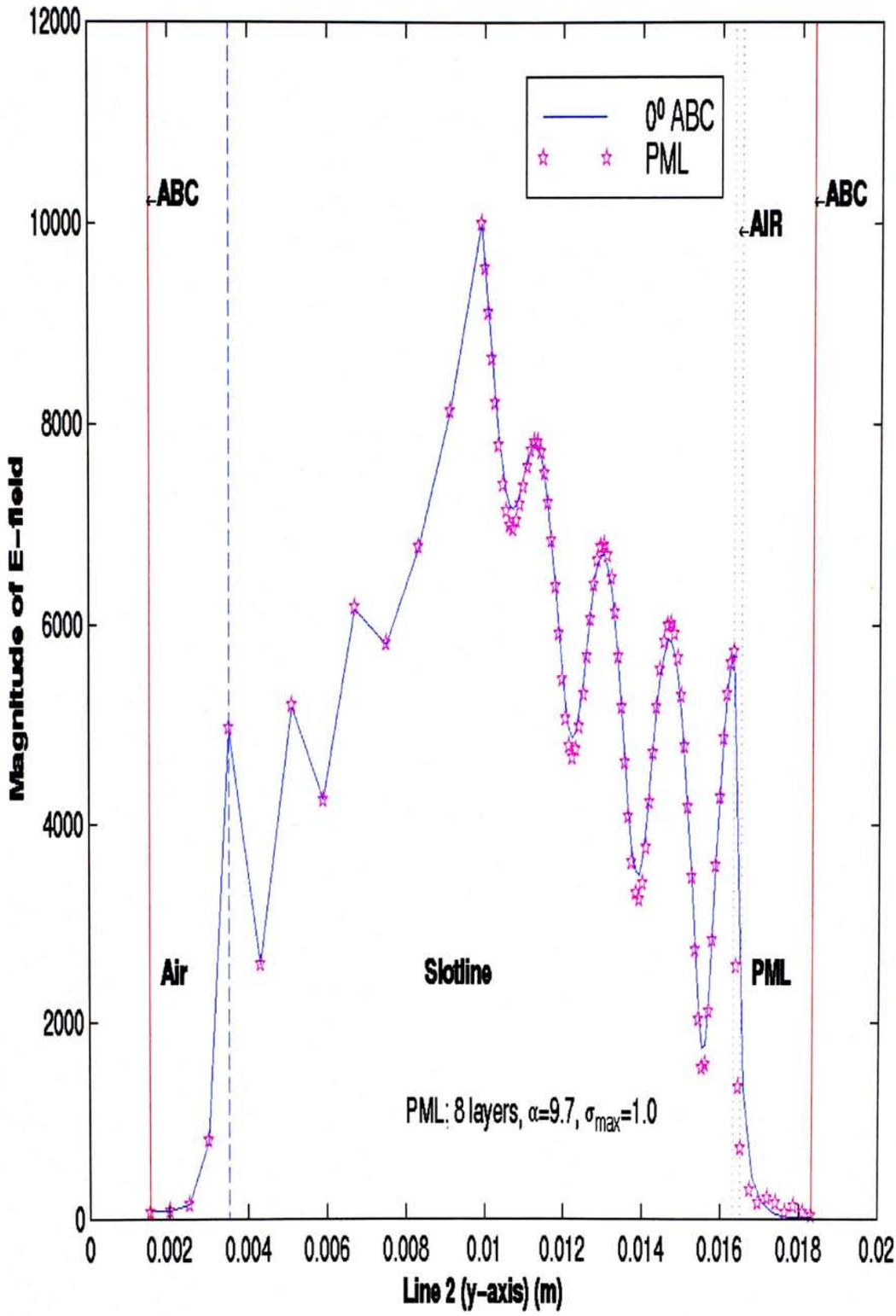

Figure 4. 7 Standing wave pattern of slotline with additional PML in the air gap

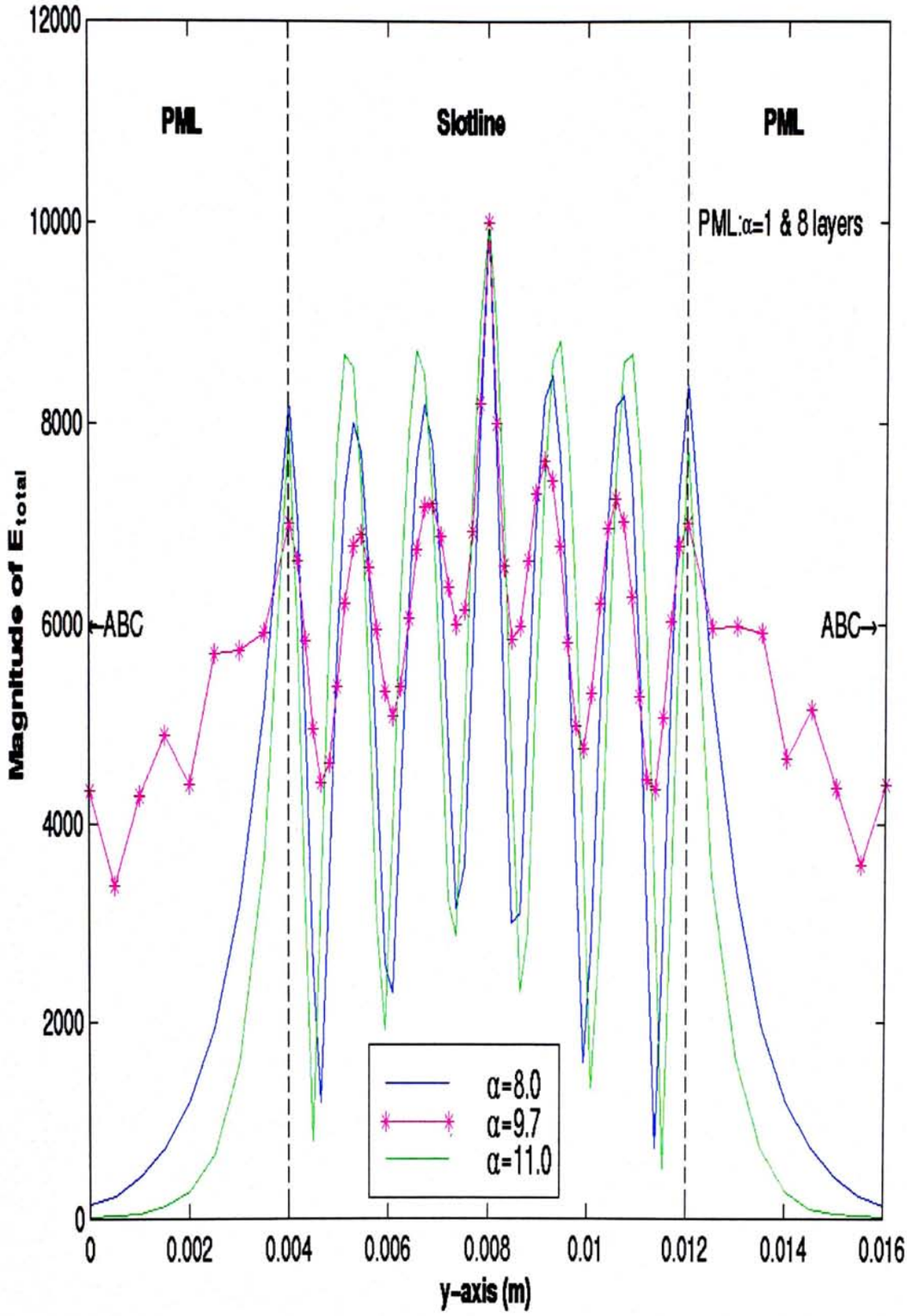

Figure 4. 8 Standing wave pattern of slotline for different values of real part in PML

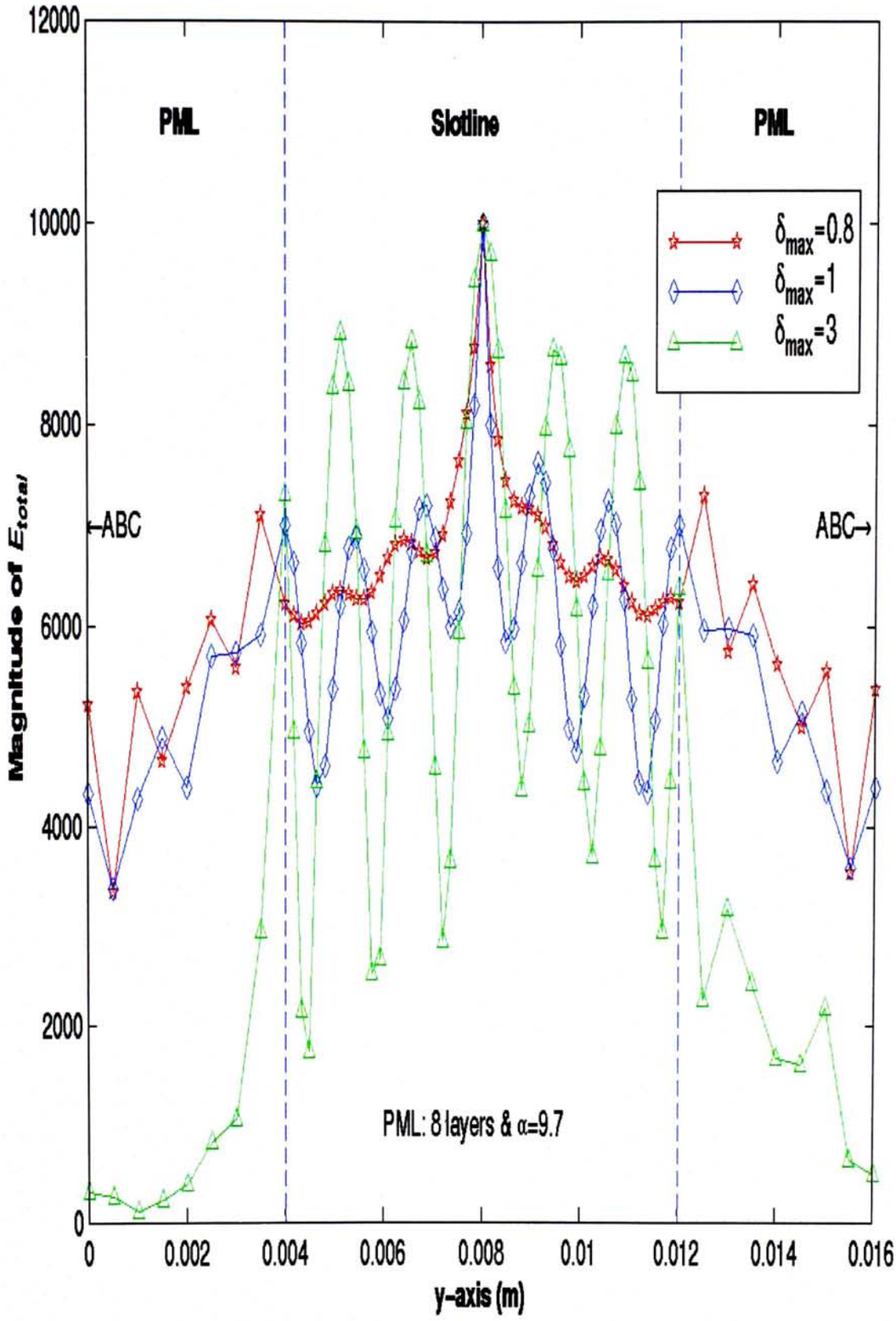

Figure 4. 9 Standing wave pattern of slotline for different values of imaginary part in PML

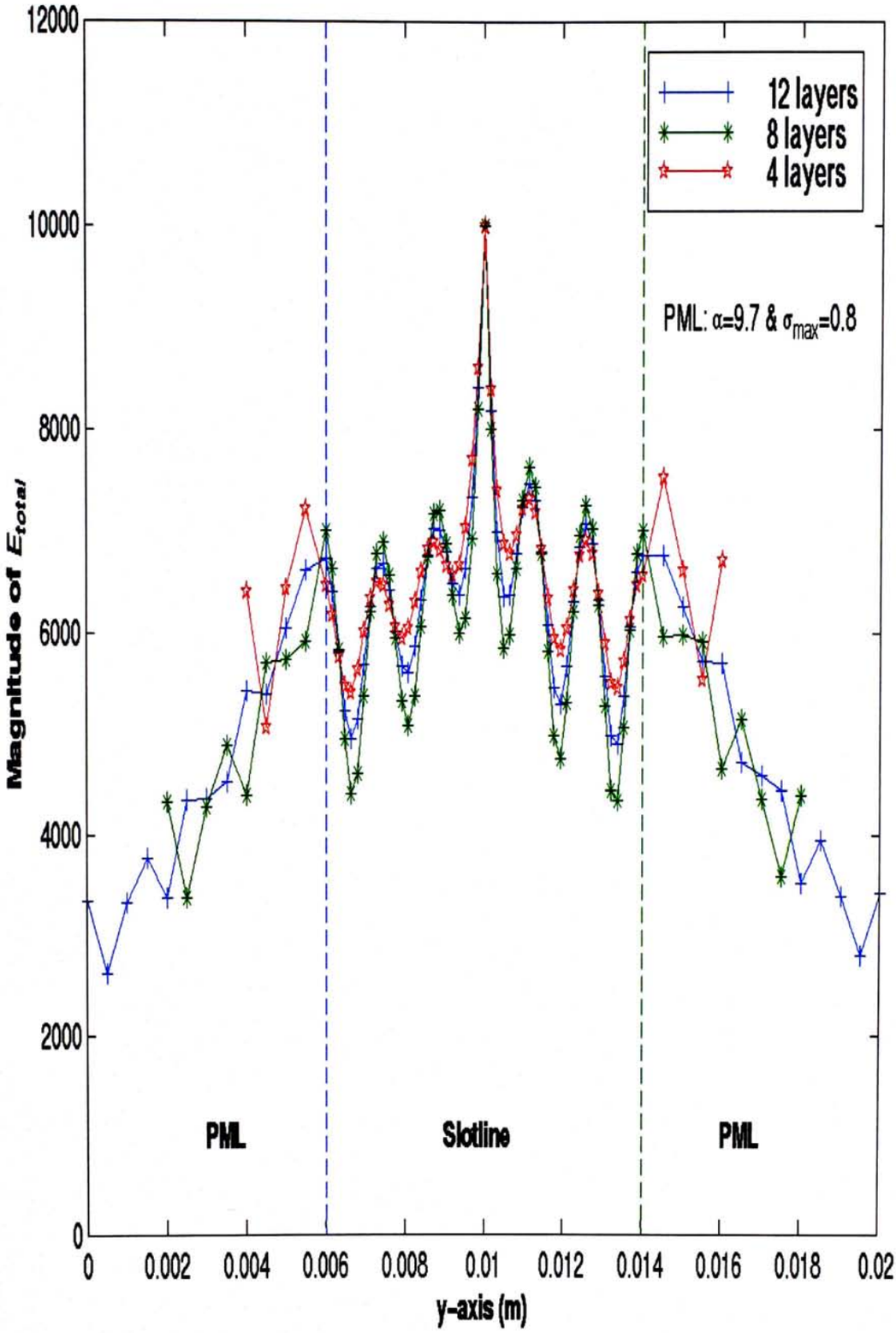

Figure 4. 10 Standing wave pattern of slotline for different numbers of layer in PML

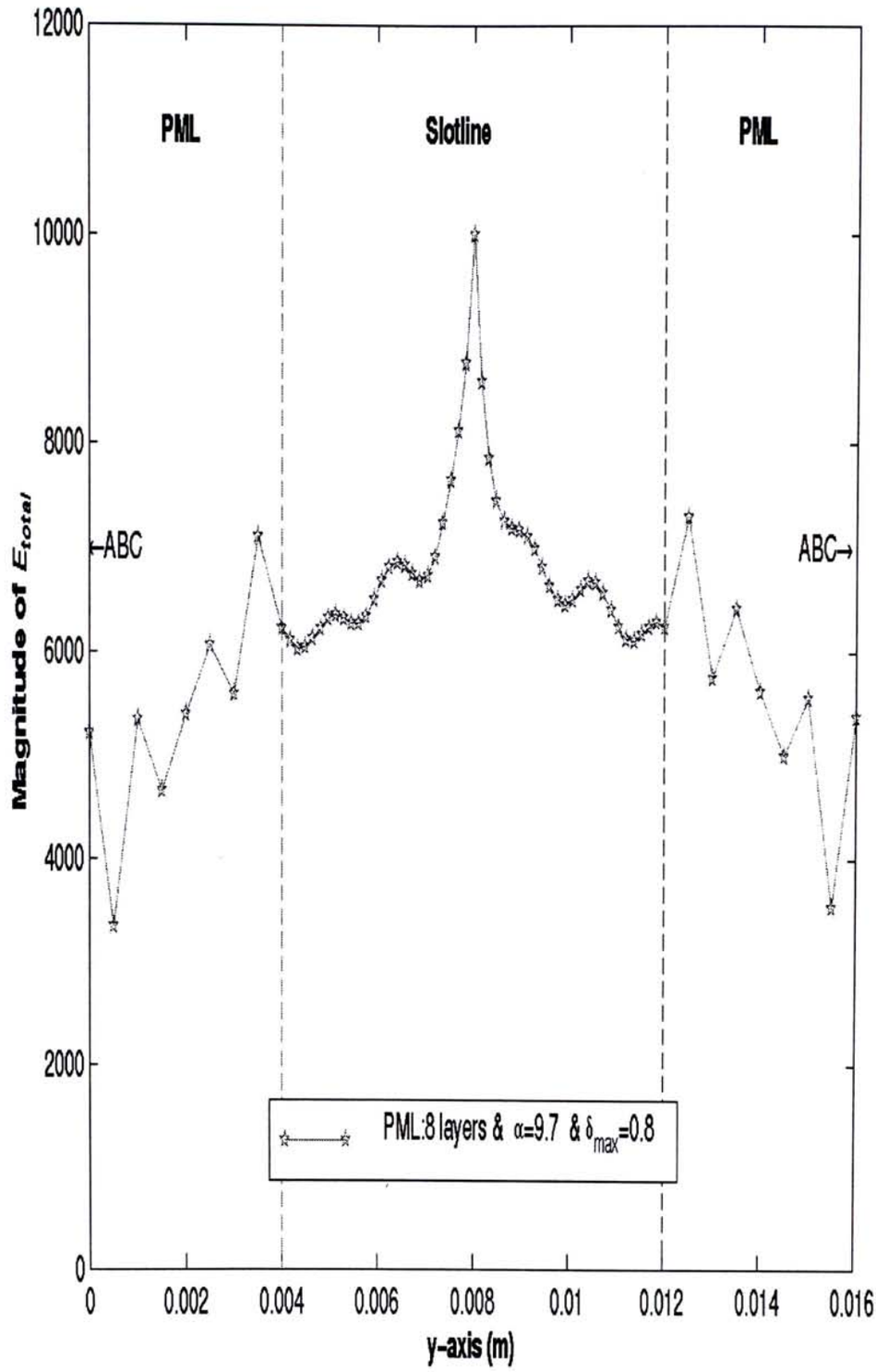

Figure 4. 11 Standing wave pattern of slotline for the best combination of parameters in PML

4.3 Slotline Taper Junction

In this section, we add a tapered opening on the slotline as shown in Figure 4.12. In the opening, the width of slotline increases gradually from the critical width $0.4\lambda_g$.

PML was added between the ABC and the slotline at the other end (without taper). Based on the experience of the slotline, we set the PML as follows: 8 layers in 4mm with α =1 and δ_{max}=0.8. On the other end of the slotline, only ABC was applied to absorb the wave.

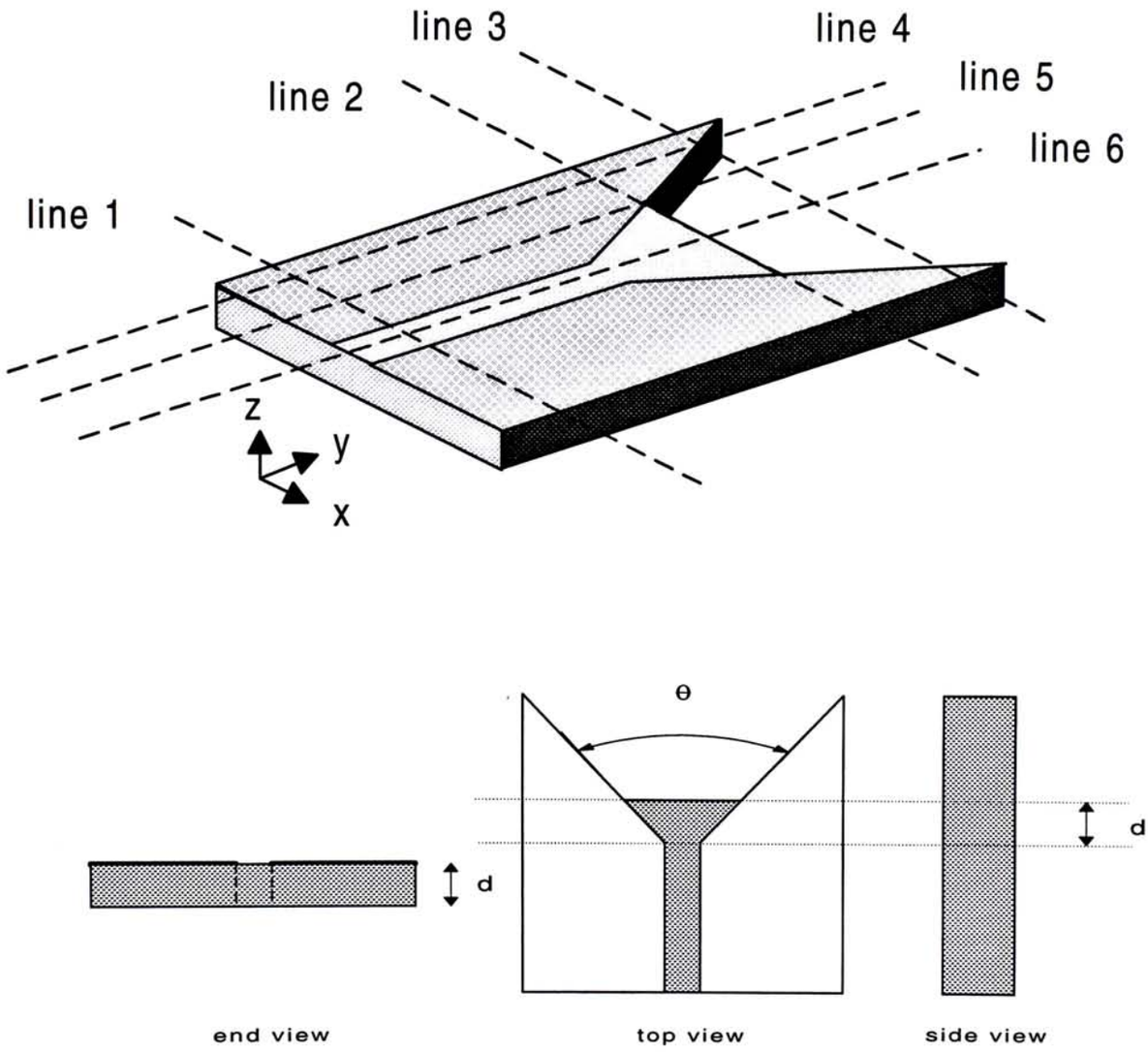

Figure 4. 12 A slotline Taper junction

Figures 4.13 to 20 shows the total electric field and the x, y and z component electric field along the six lines as defined in Figure 4.12. Figures 4.21 and 22 show a 3-dimensional plot of the field distribution of the slotline taper junction.

In Figure 4.23, we fixed the dielectric length d at 1/8 λ_g, i.e. 0.8mm at 40 GHz. We observed a stronger reflection in the slotline as the angle of taper opening increases. On the other hand, in the taper, the field radiates more efficiently into air when the taper angle is small. In fact, the taper angle θ is zero in an infinite slotline and 180° in open terminated slotline. Therefore, the adjustment of taper angle implies a transition from infinitely long to a finite length.

In Figure 4.24 and 25, we performed another set of simulation for different values of dielectric length d (Fig.4.12), while keeping the taper angle at 45°. When d = 0, the standing wave pattern looks like those without tapering. Increasing d from 0 to 1/4 λ_g, the reflection decreases gradually. But the reflection increases again for further increase of d up to 7/16 λ_g. These results agree with experimental observation in [1.1].

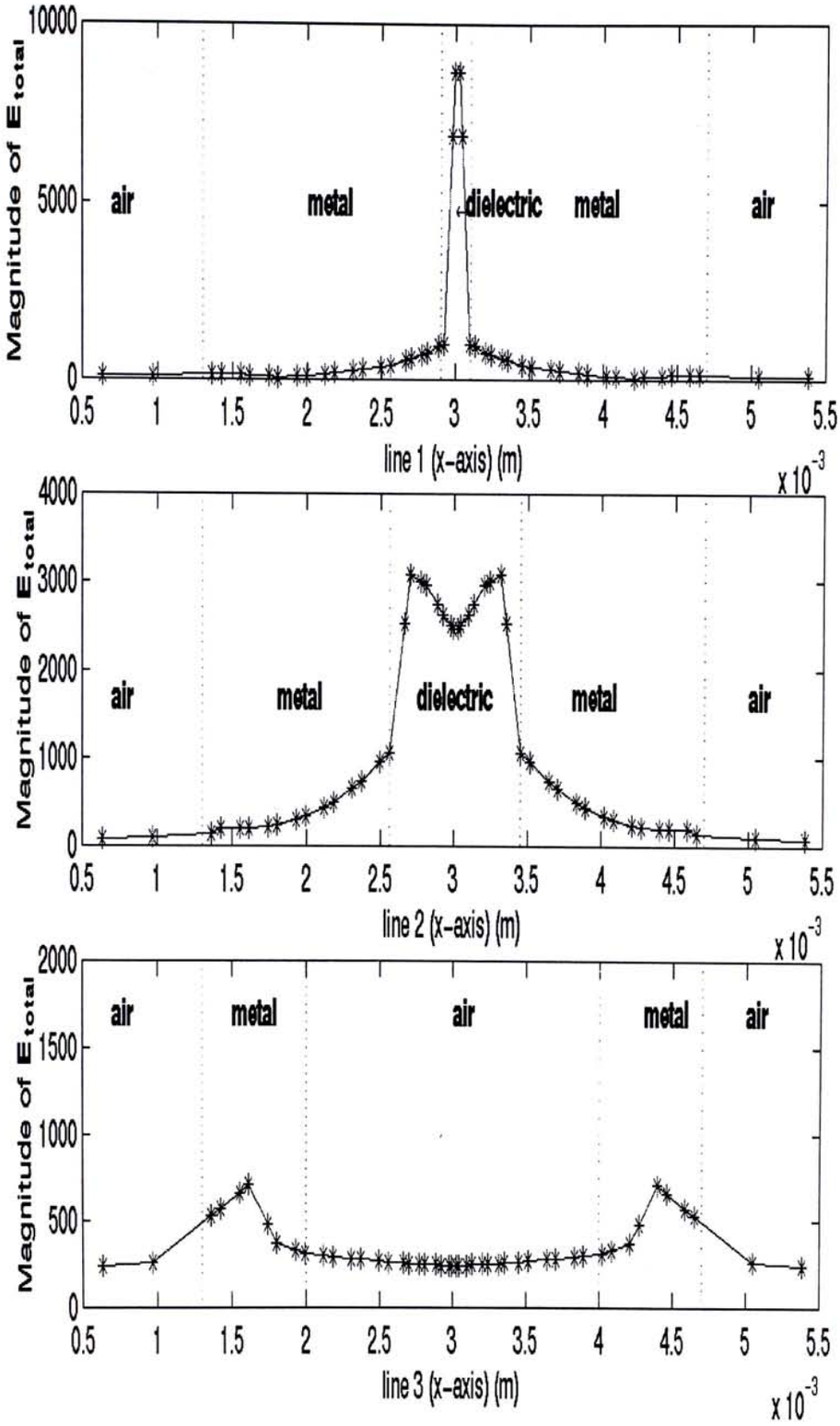

Figure 4. 13 Distribution of electric field of slotline taper opening

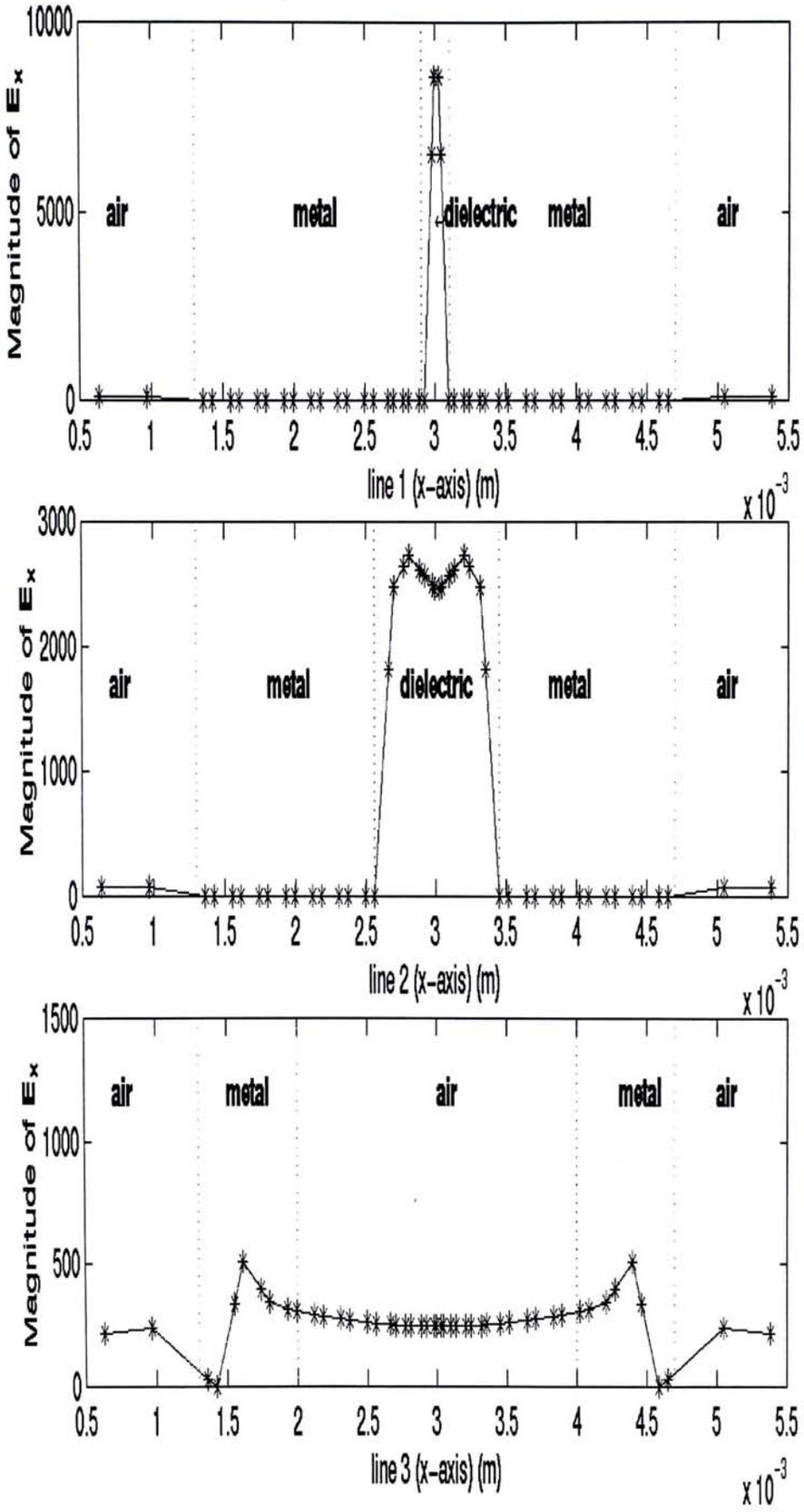

Figure 4. 14 Distribution of electric field of slotline taper opening

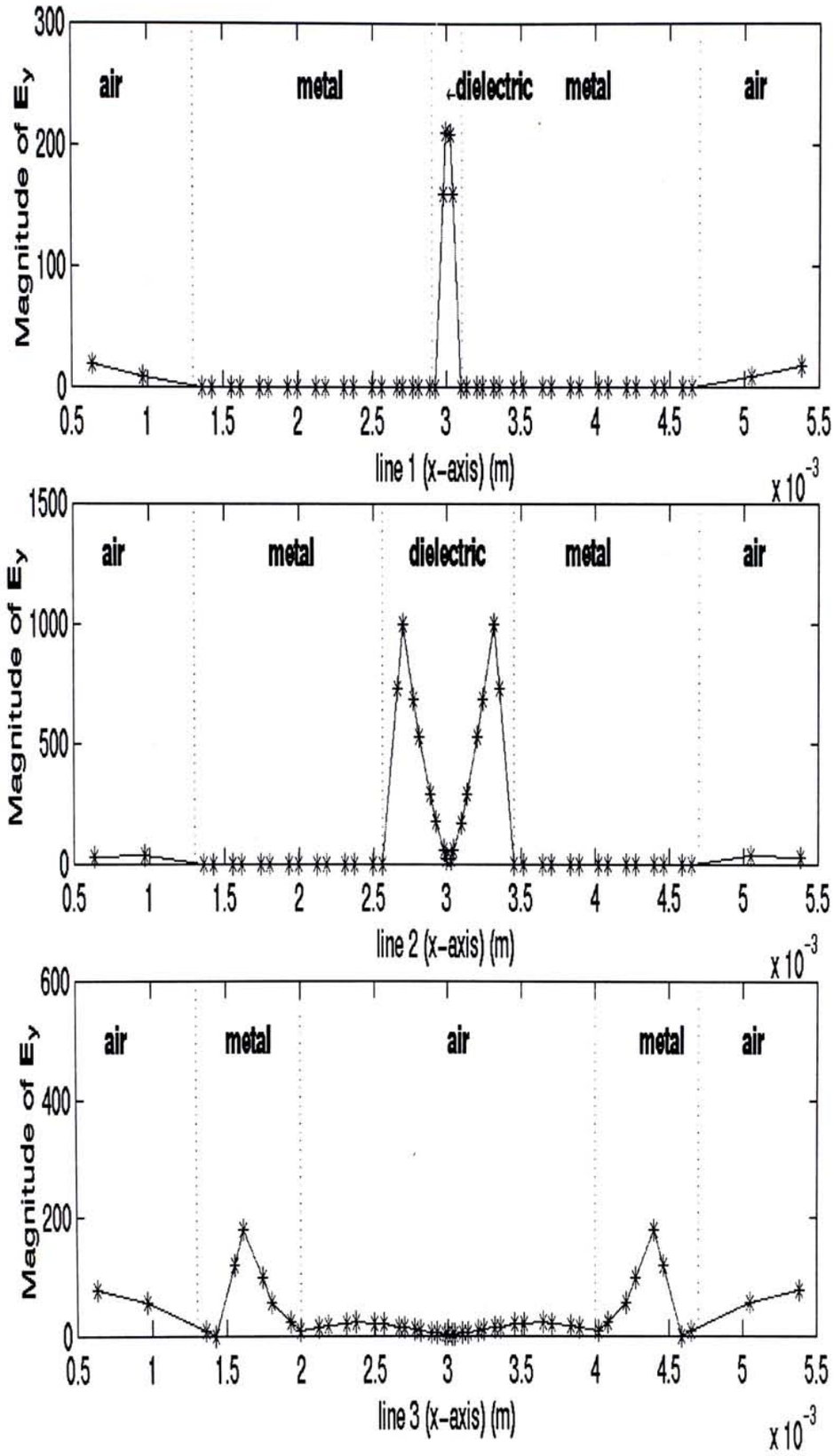

Figure 4. 15 Distribution of electric field of slotline taper opening

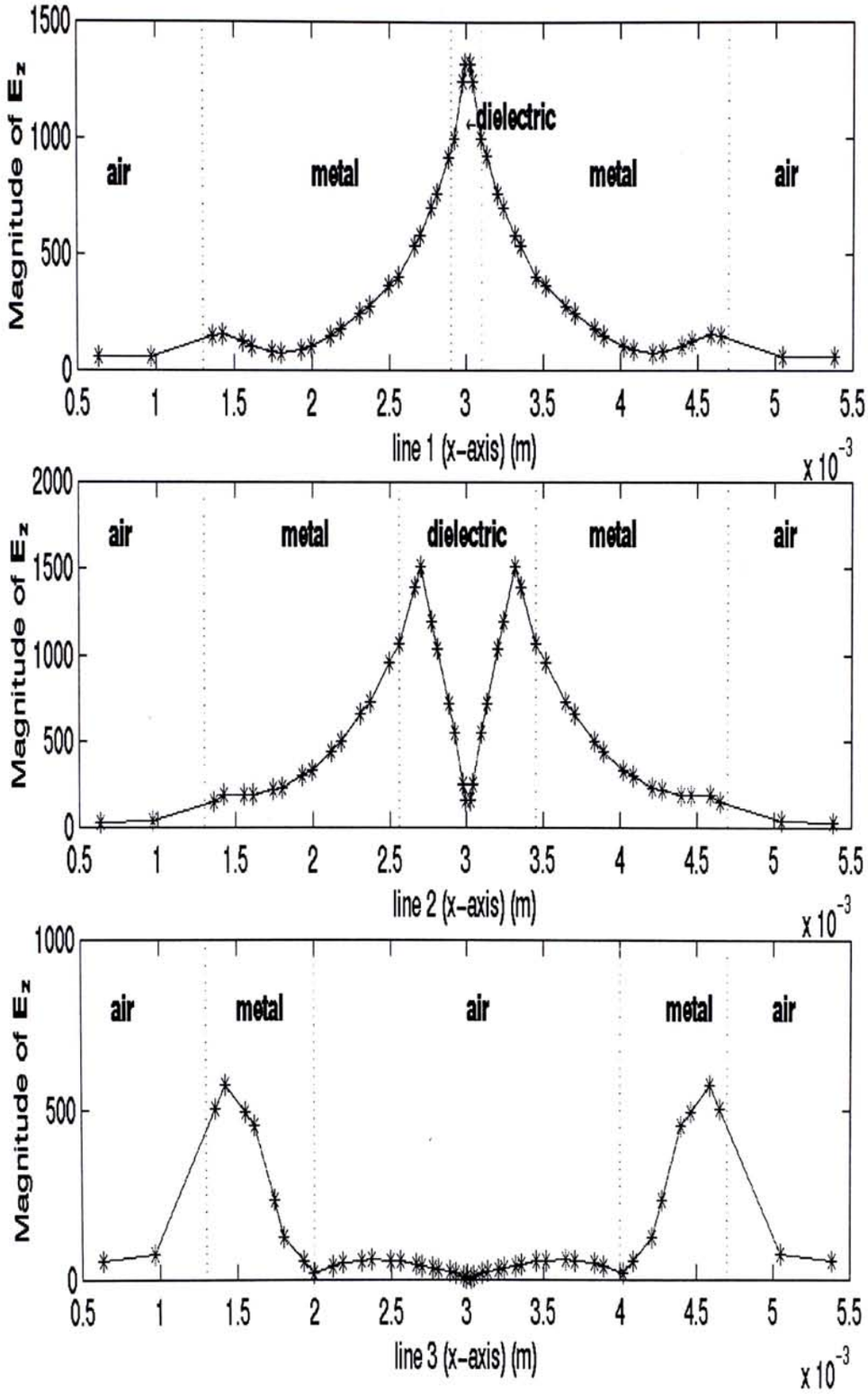

Figure 4. 16 Distribution of electric field of slotline taper opening

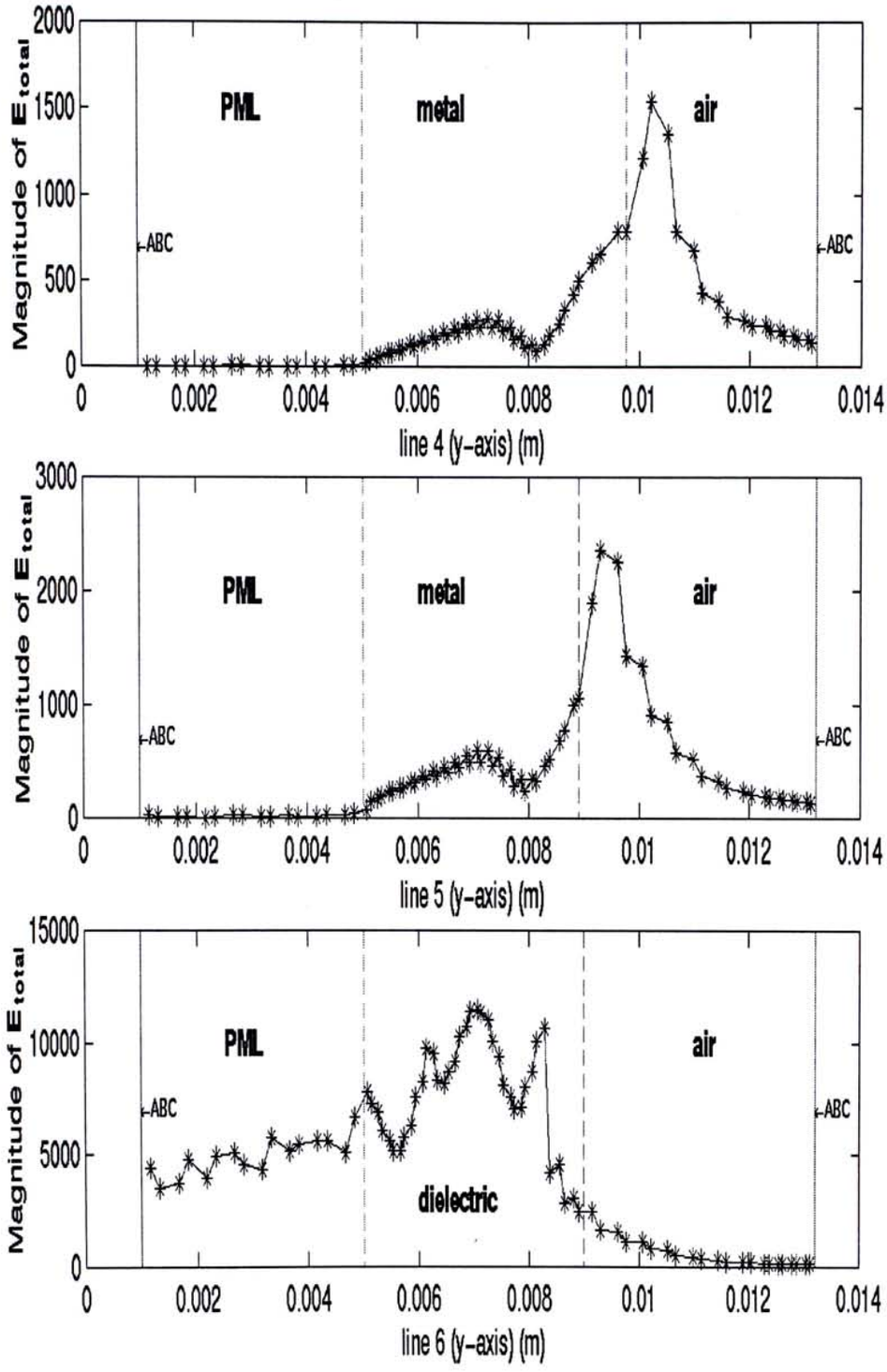

Figure 4. 17 Distribution of electric field of slotline taper opening

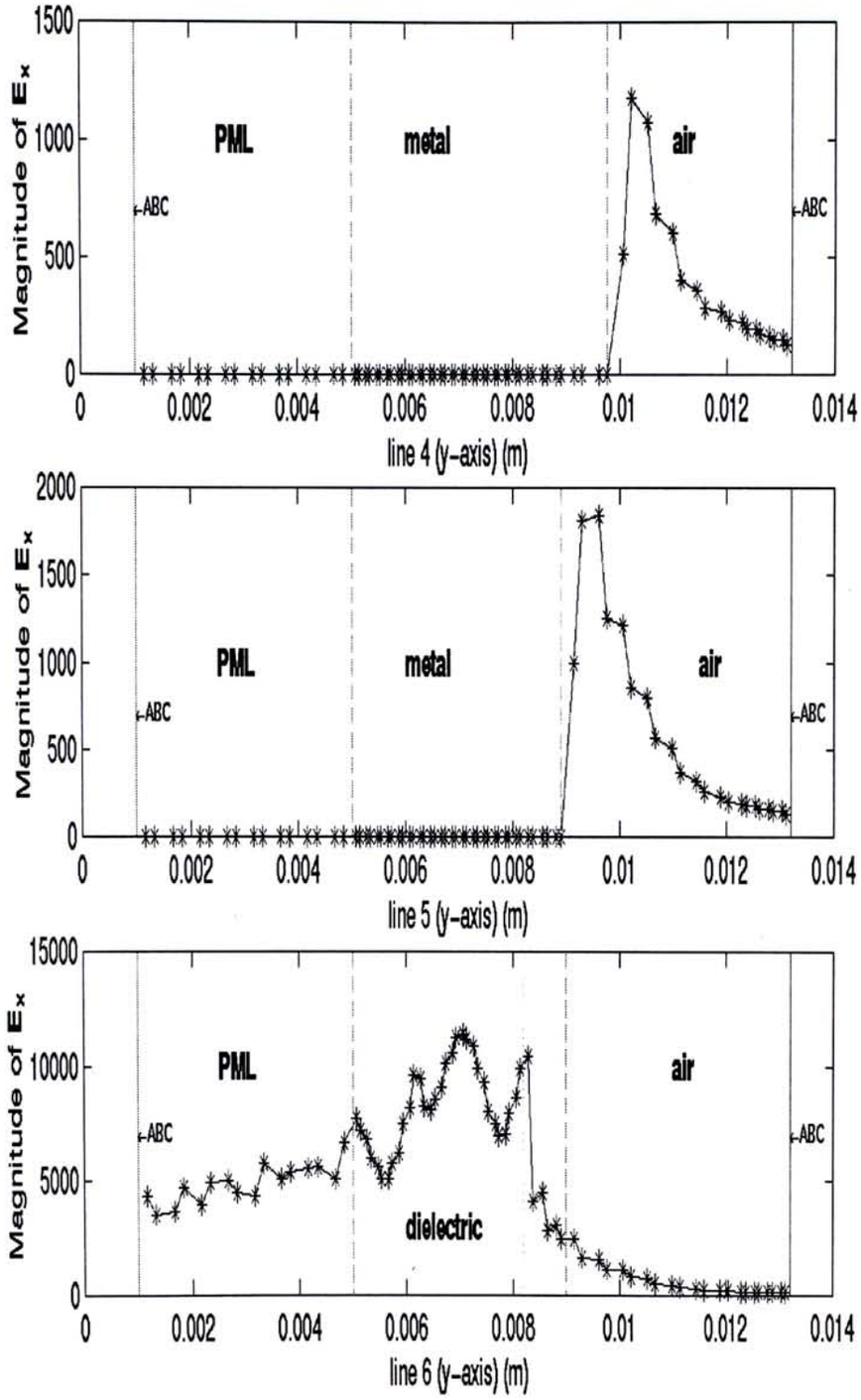

Figure 4. 18 Distribution of electric field of slotline taper opening

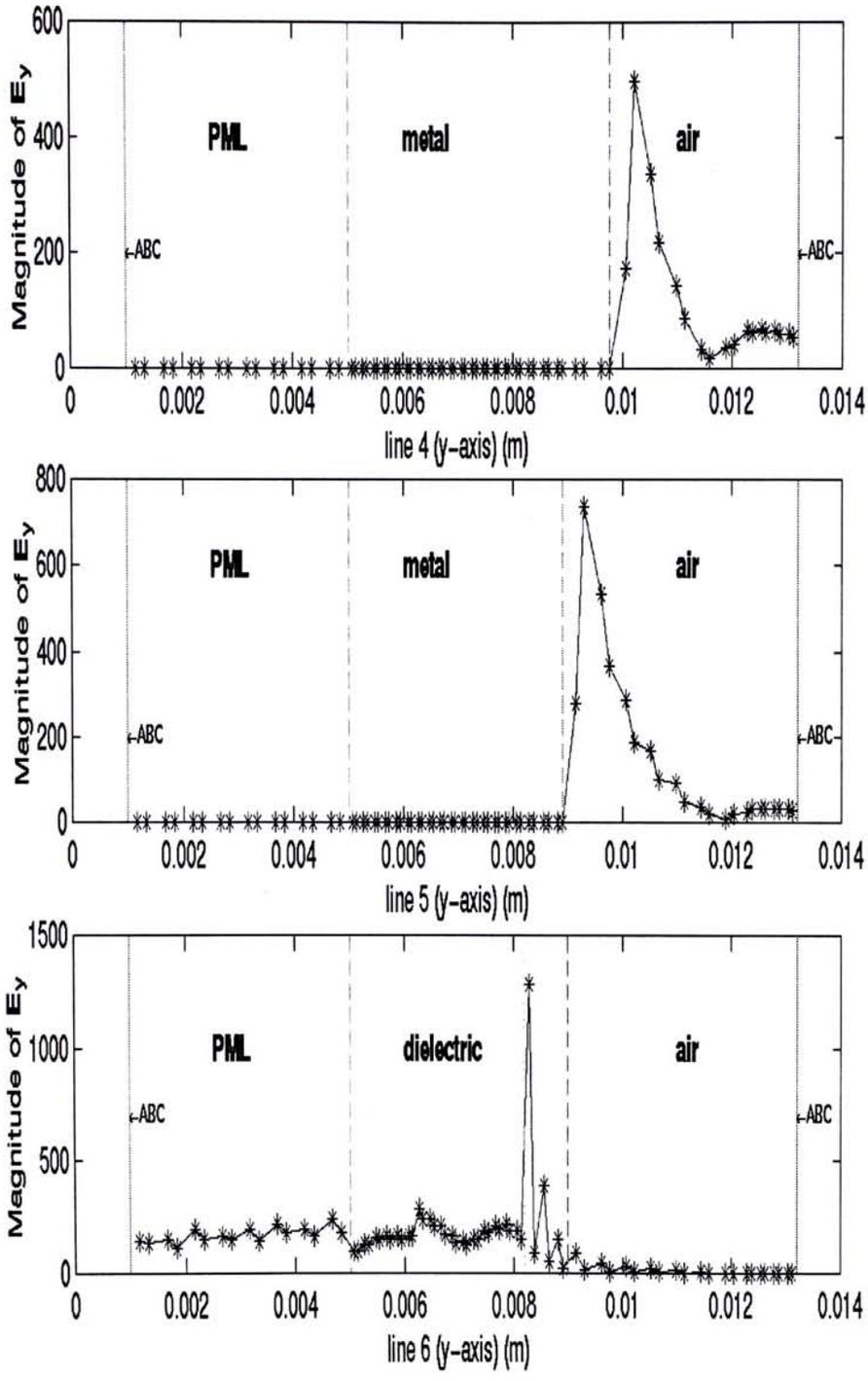

Figure 4. 19 Distribution of electric field of slotline taper opening

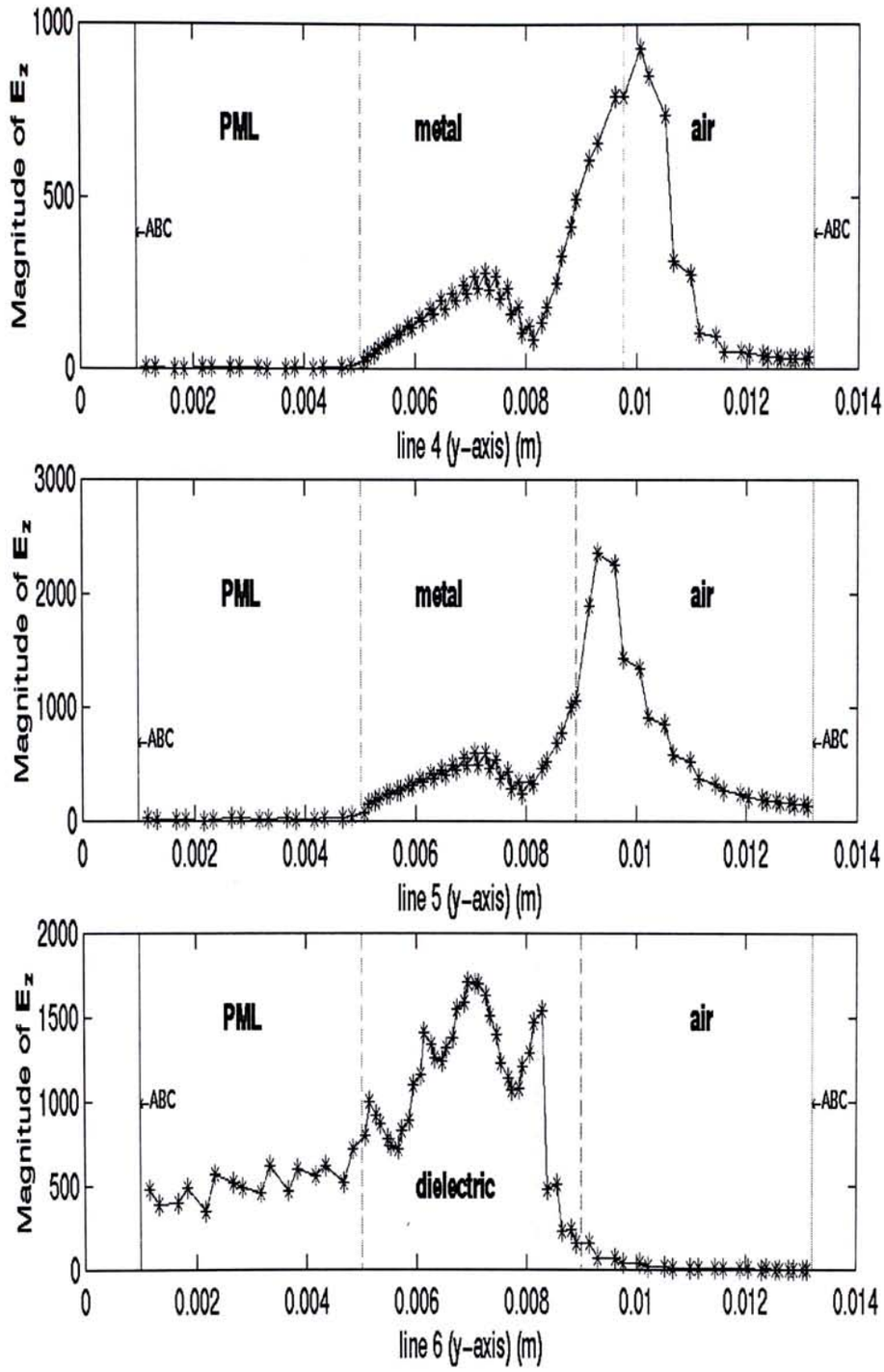

Figure 4. 20 Distribution of electric field of slotline taper opening

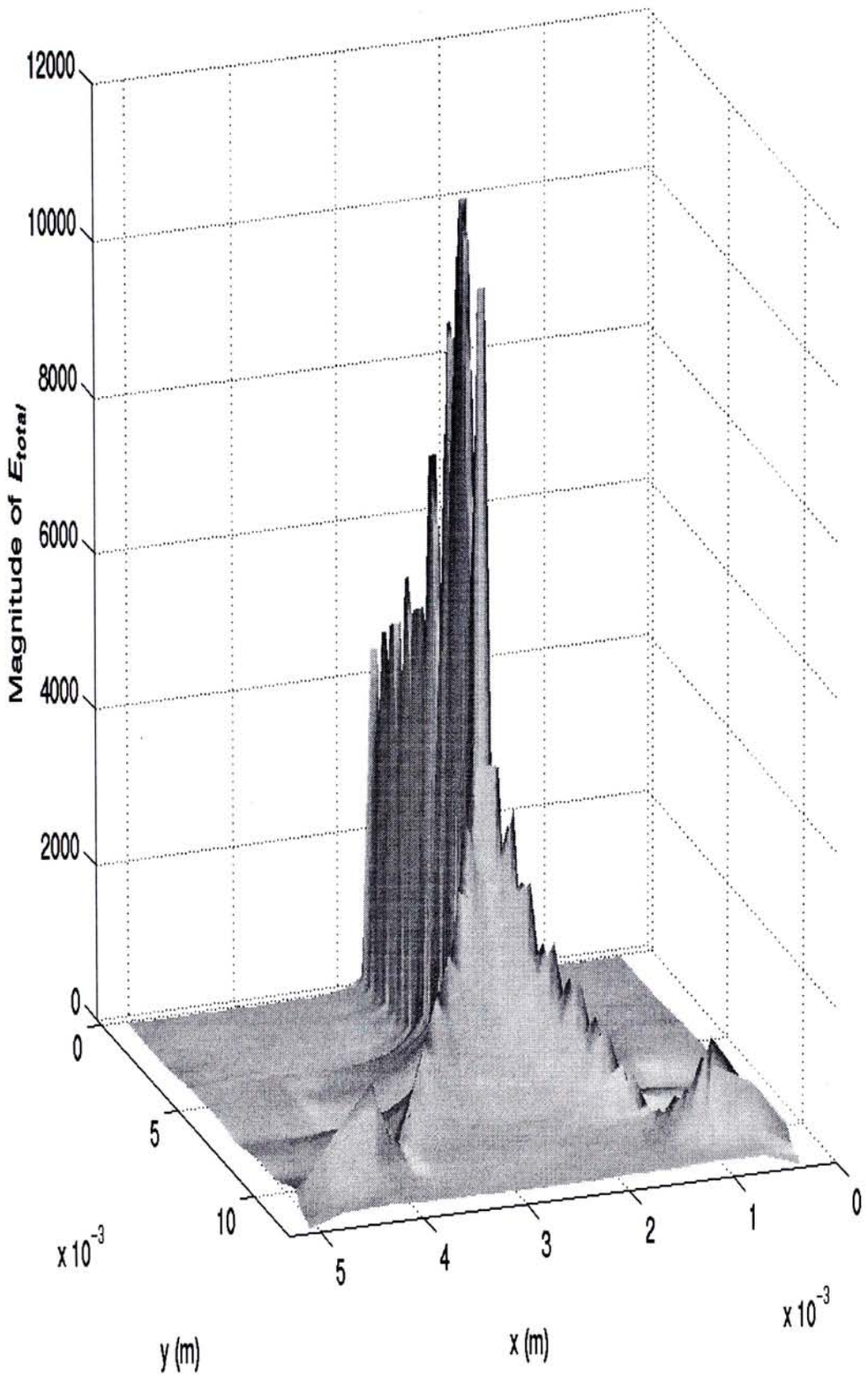

Figure 4. 21 Distribution of electric field of slotline taper opening on the slotline plate level

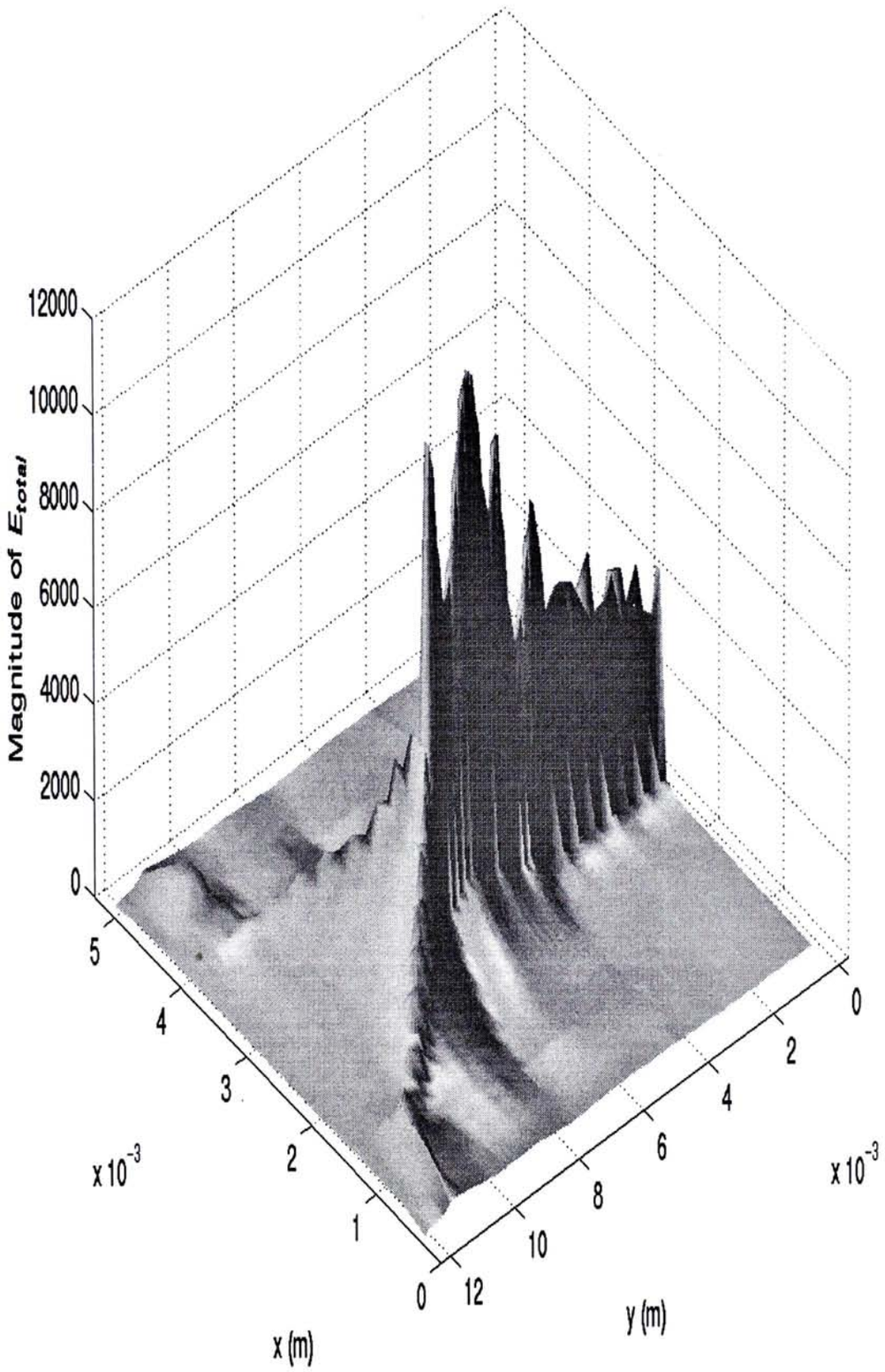

Figure 4. 22 Distribution of electric field of slotline taper opening on the slotline plate level

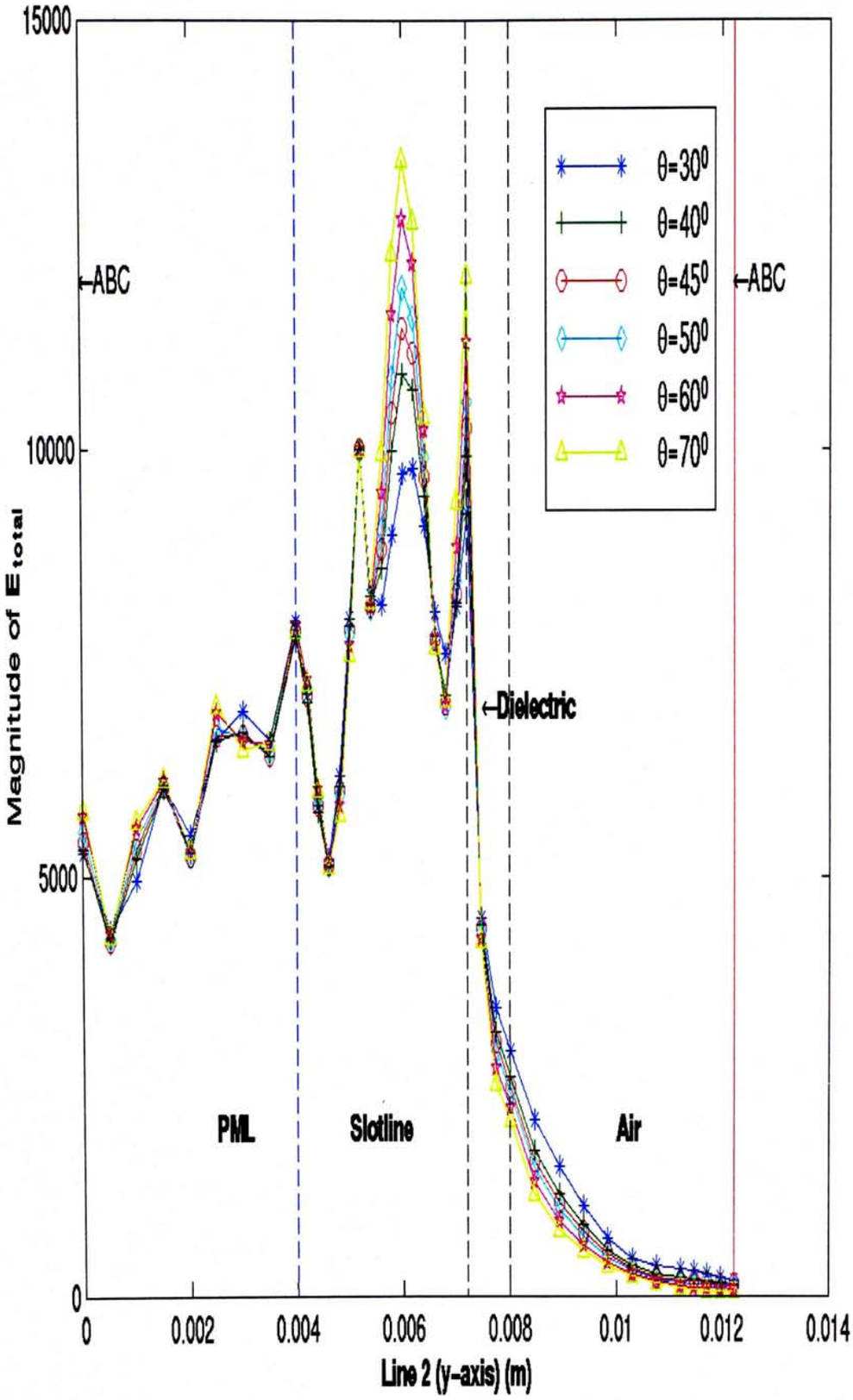

Figure 4. 23 Distribution of electric field of slotline taper opening for various taper angle

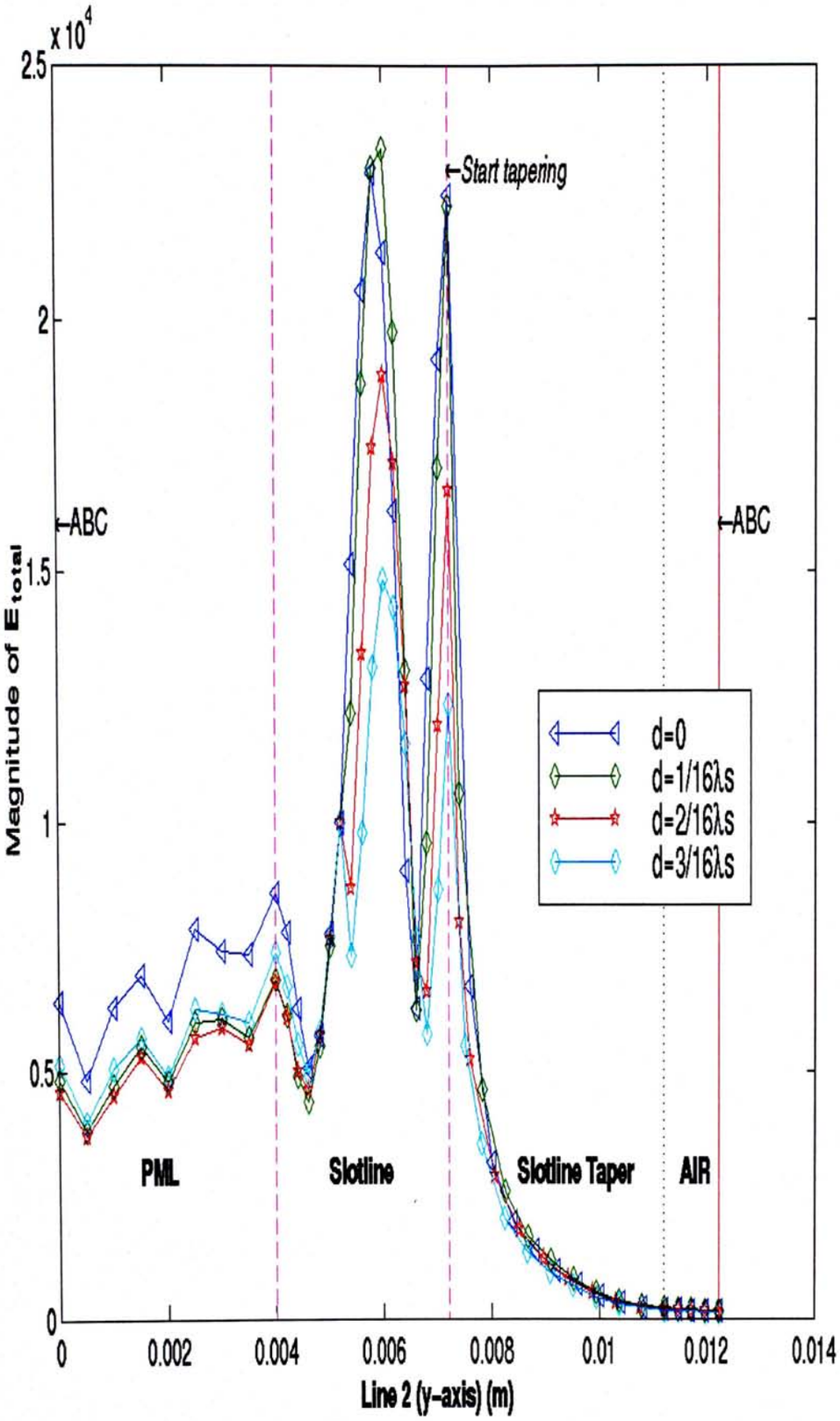

Figure 4. 24 Distribution of electric field of slotline taper opening for various dielectric extension

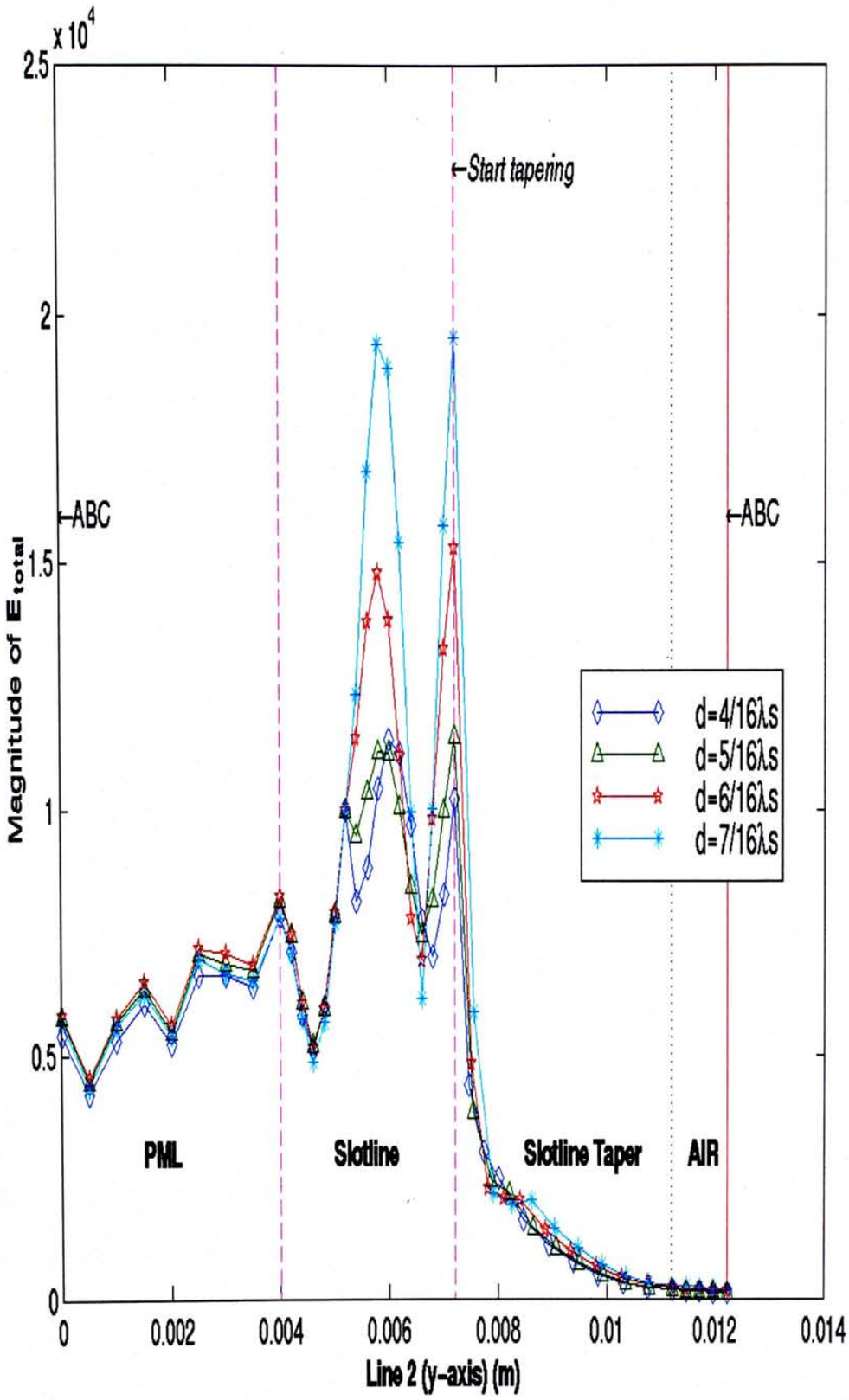

Figure 4. 25 Distribution of electric field of slotline taper opening for various dielectric extension

4.4 Slotline-Bowtie Junction

In this section, we modelled the slotline-bowtie junction as shown in Figures 4.26 and 27. We added two metallic triangles vertically into the slotline taper. In finite element analysis, the number of layer in the mesh must expand vertically to contain the bowtie. As a result, the number of total edge increases significantly and the system matrix becomes very large. The thickness of the slotline is 1.6mm while the flare angles (ϕ, θ) are 45° and 70° respectively. Similar to the case of slotline with bowtie, we added the PML and ABC at one end of the slotline but only ABC on the other.

From Figures 4.28 to 35, the magnitude and x, y, z components of the electric field along various lines on the slotline plate level were plotted. Along y-axis, we clearly observed that the field concentrates on the slot and then radiates outward in the taper.

In Figures 4.36 & 37, the distribution of E-field on the slotline plate level were plotted. The only difference between these two pictures and Figures 21 and 22 is the addition of metallic. Comparing the two graphs, in the region of taper, we found that the wave propagates out much better in the case of the slotline bowtie junction. This result agrees with experimental results. In Figure 4.38, we compare the total electric field of the slotline bowtie junction and the slotline taper junction along line 3. As mentioned before, the fields of the slotline bowtie junction is much stronger. This is also confirmed in another plot of the field along line 6 in Figure 4.39.

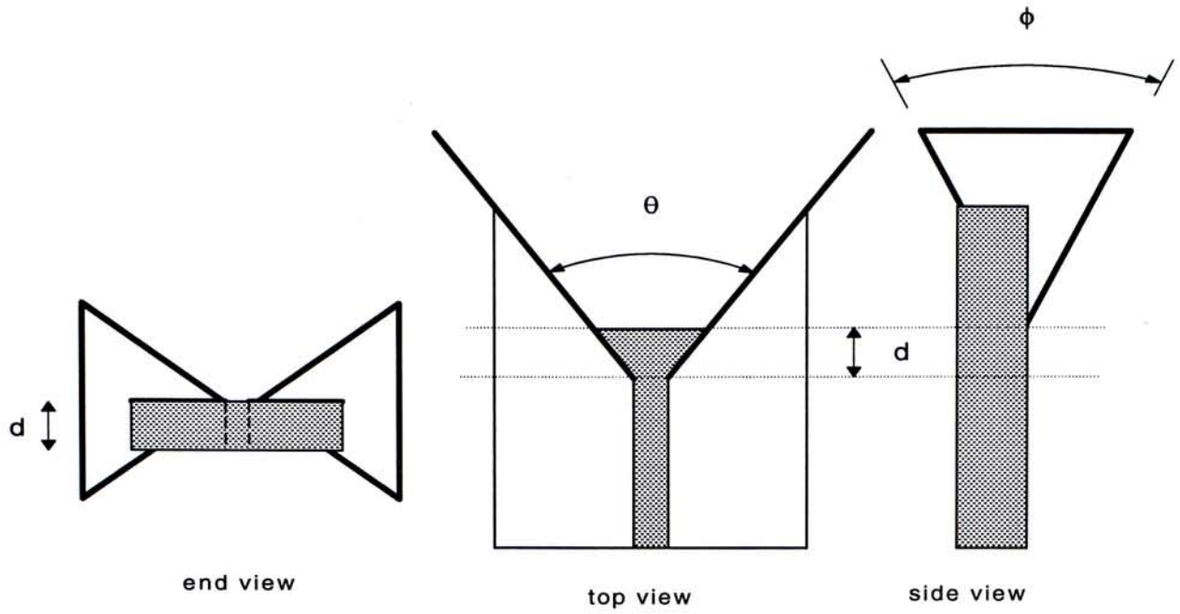

Figure 4. 26 A slotline-bowtie junction

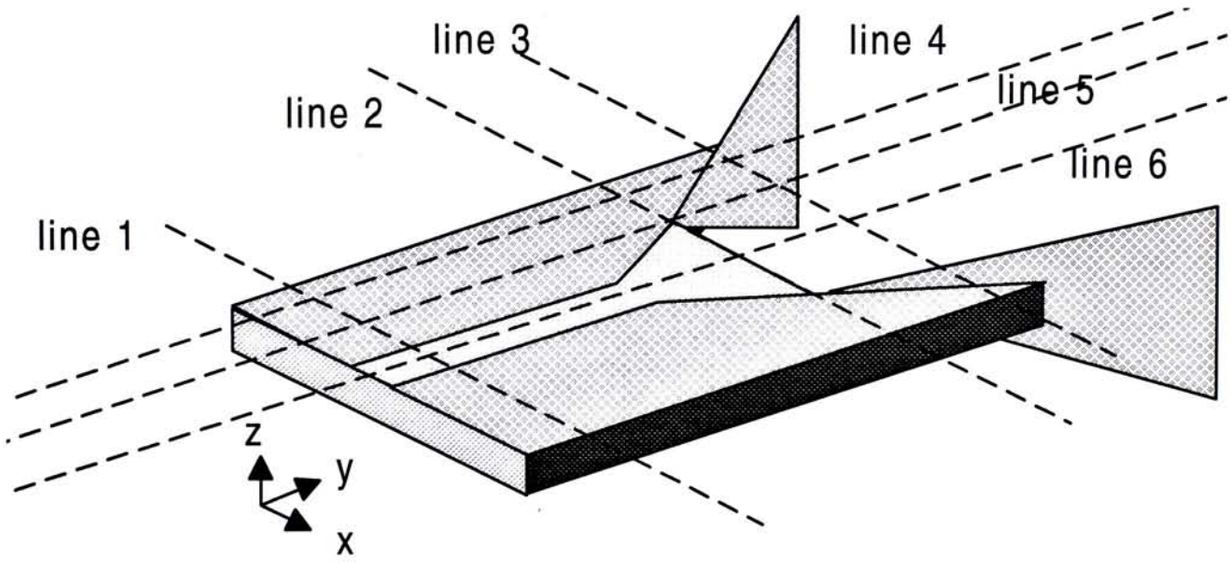

Figure 4. 27 A slotline-bowtie junction

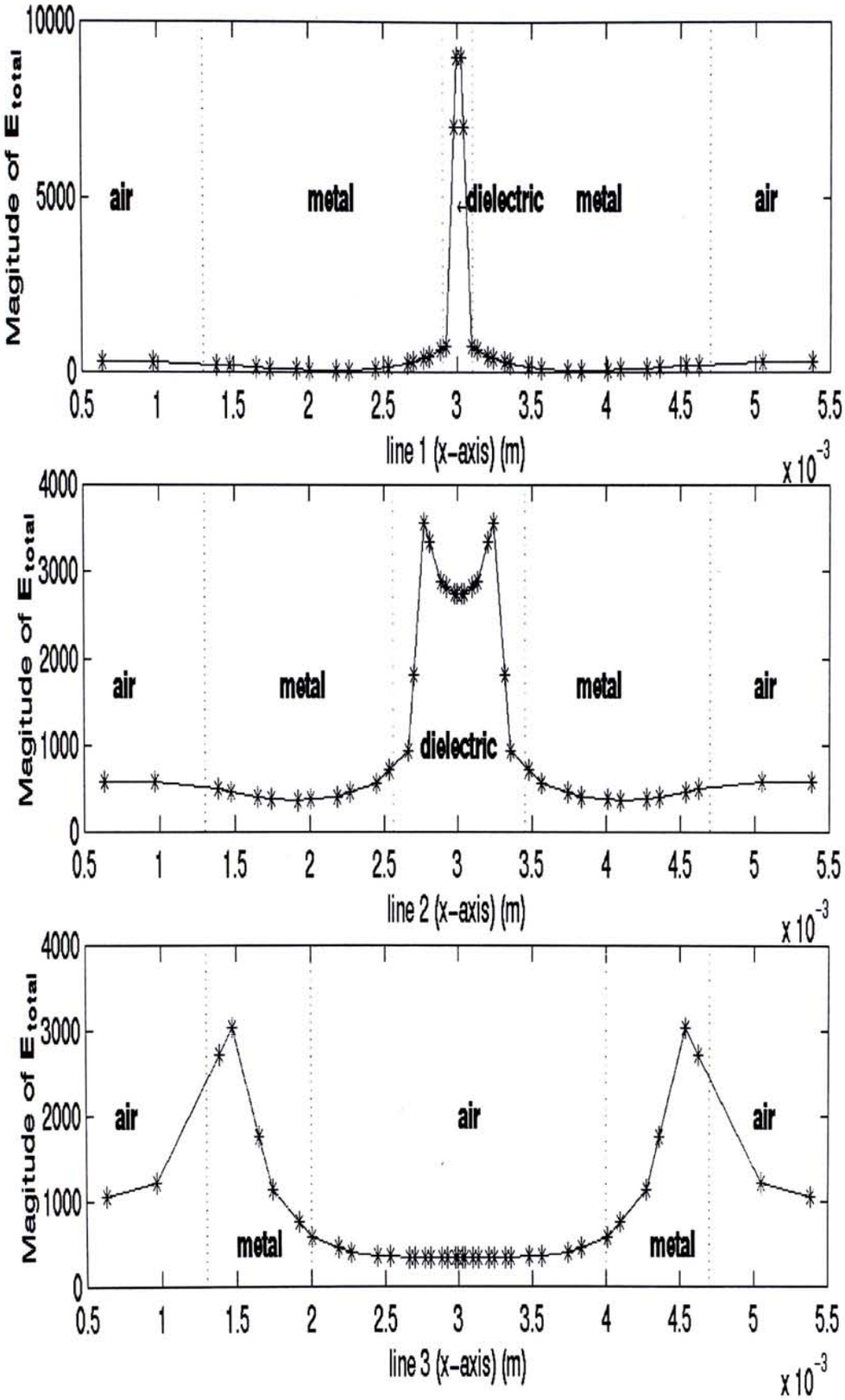

Figure 4. 28 Distribution of electric field of slotline-bowtie junction

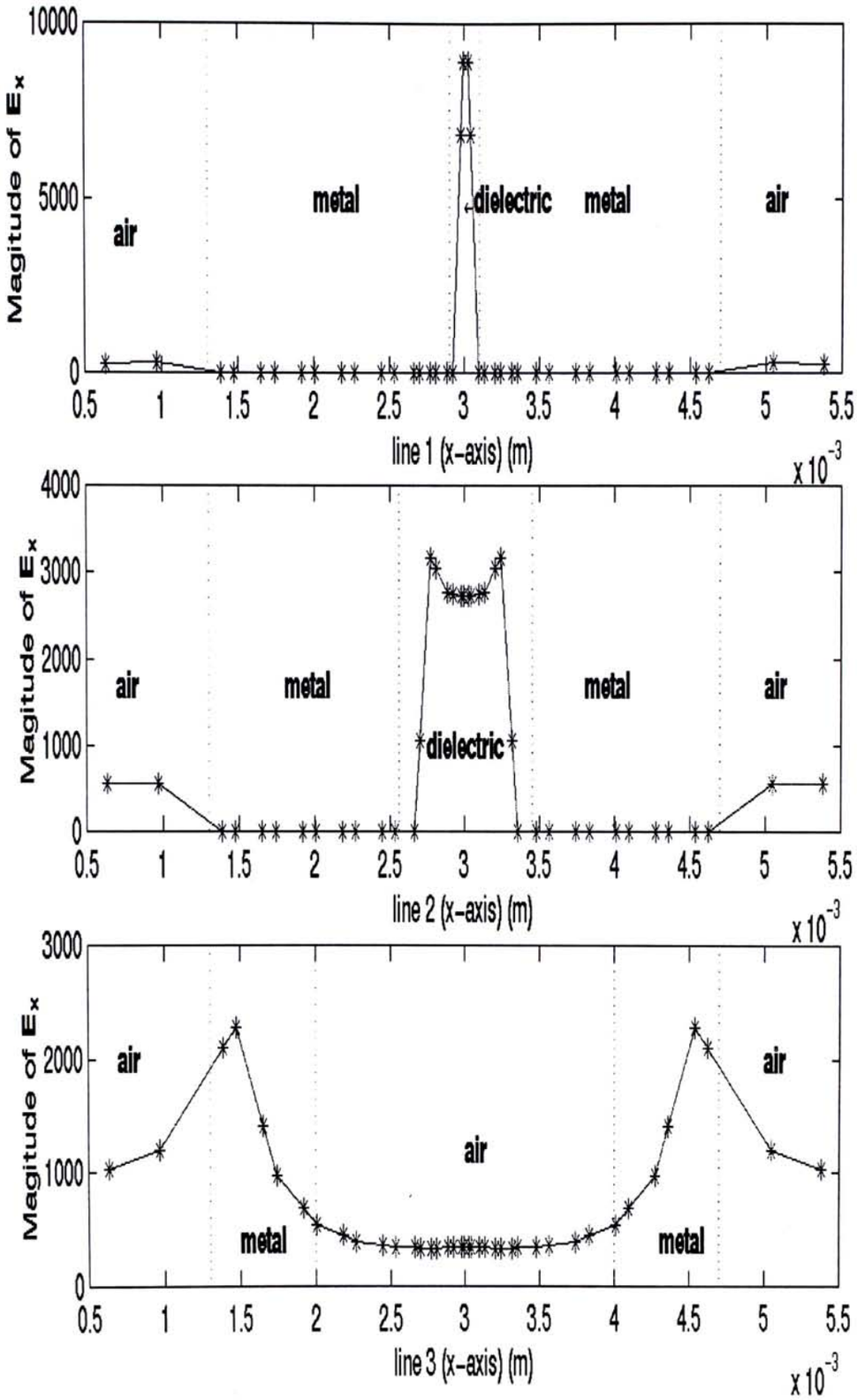

Figure 4. 29 Distribution of electric field of slotline-bowtie junction

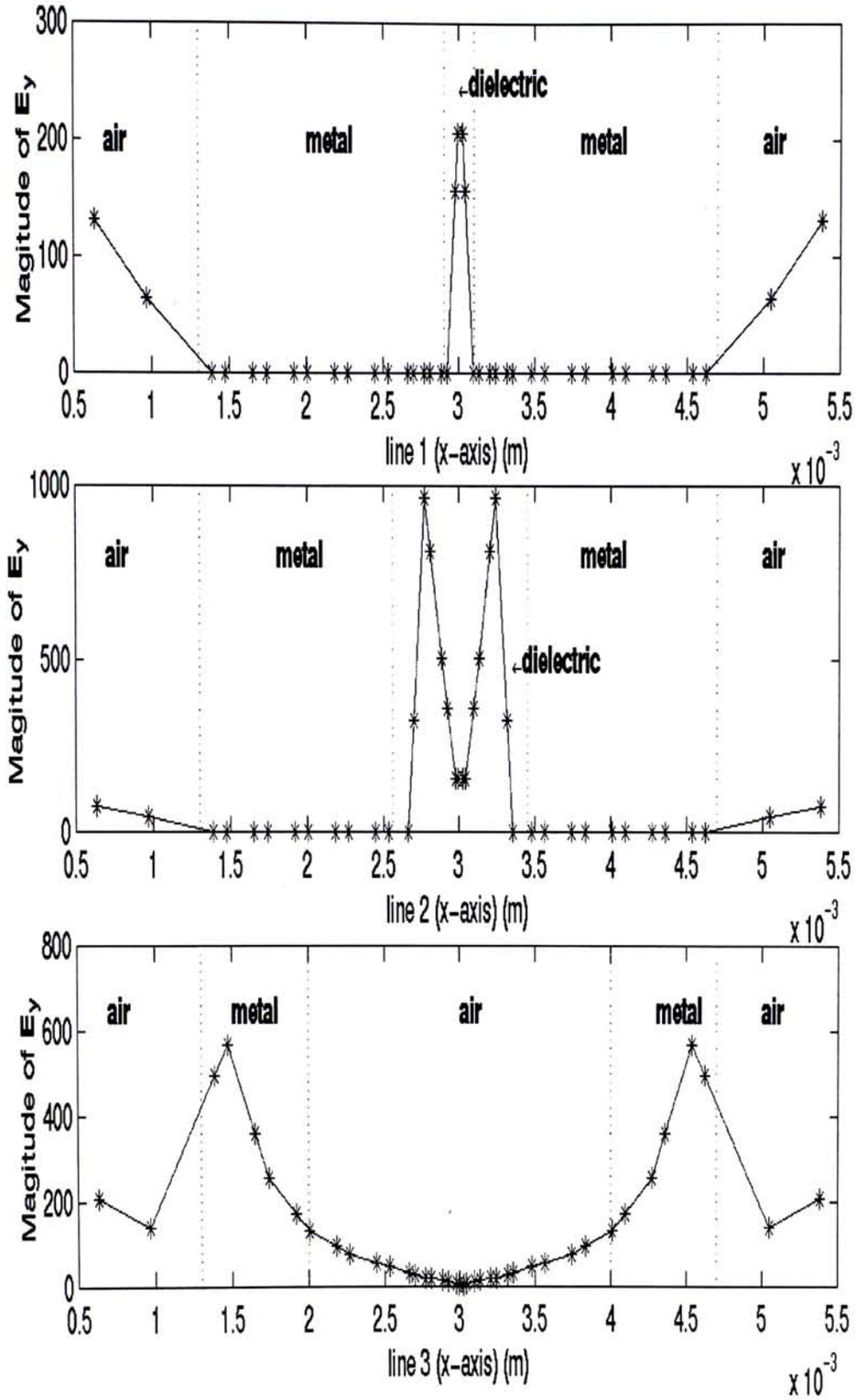

Figure 4. 30 Distribution of electric field of slotline-bowtie junction

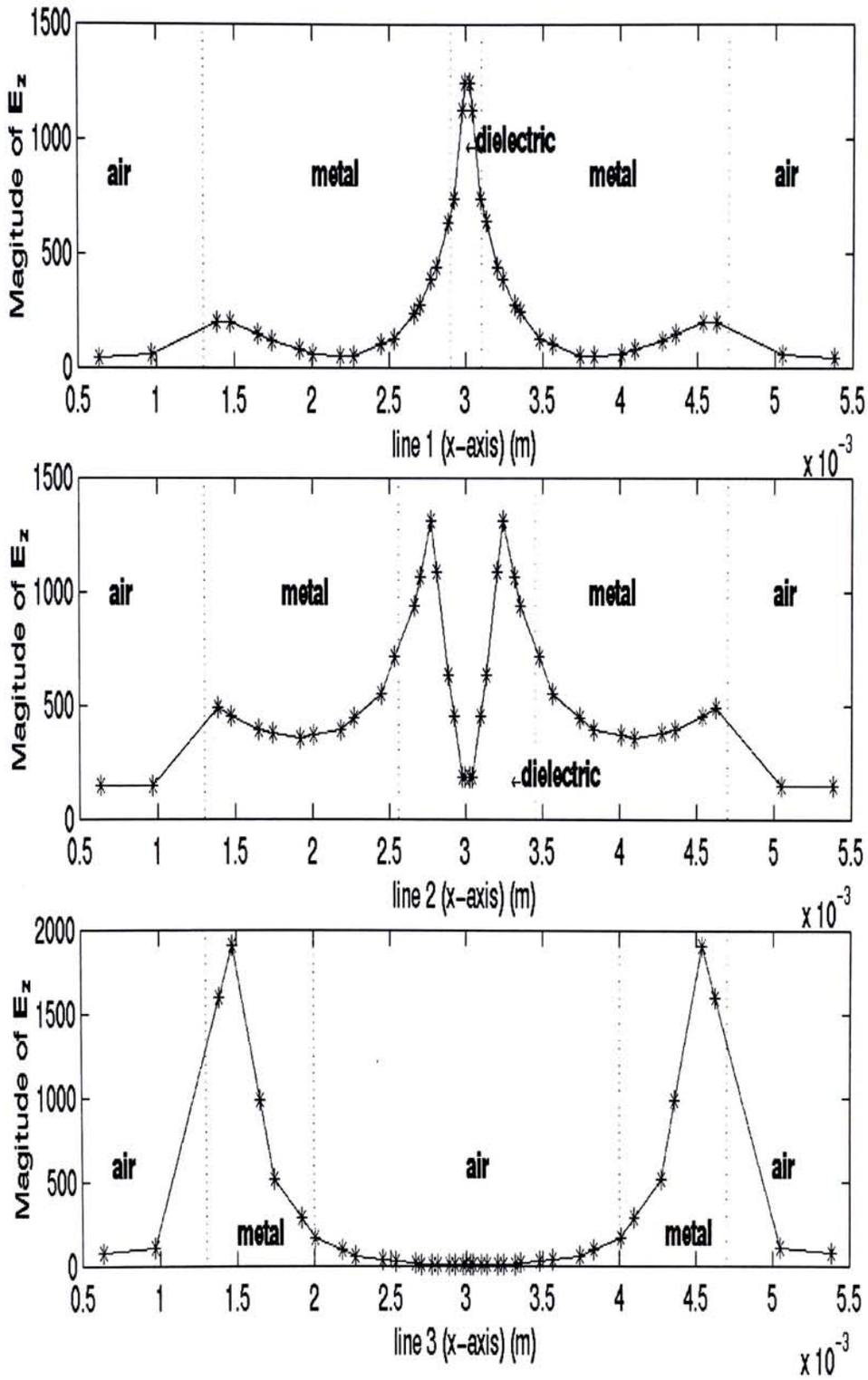

Figure 4. 31 Distribution of electric field of slotline-bowtie junction

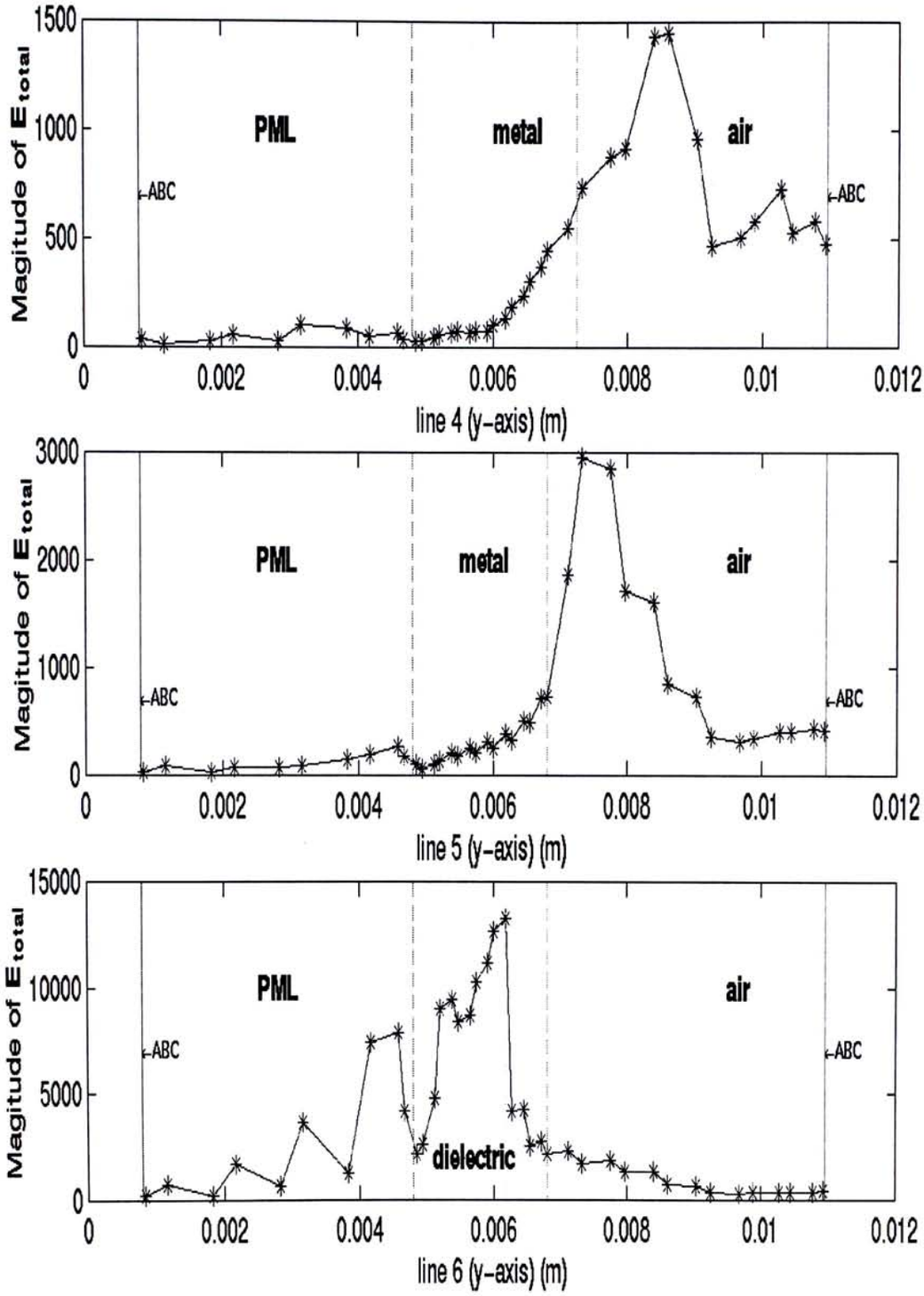

Figure 4. 32 Distribution of electric field of slotline-bowtie junction

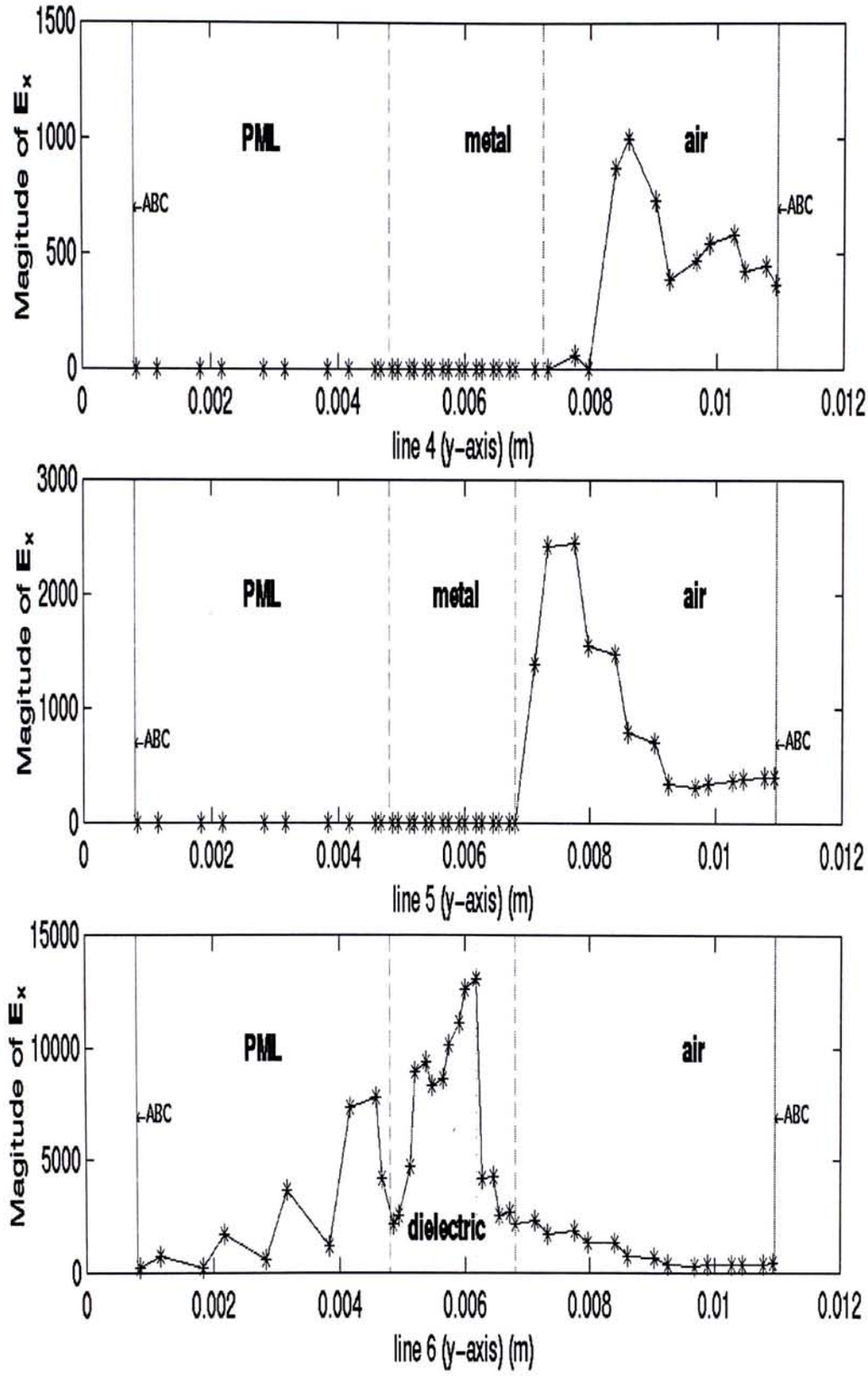

Figure 4. 33 Distribution of electric field of slotline-bowtie junction

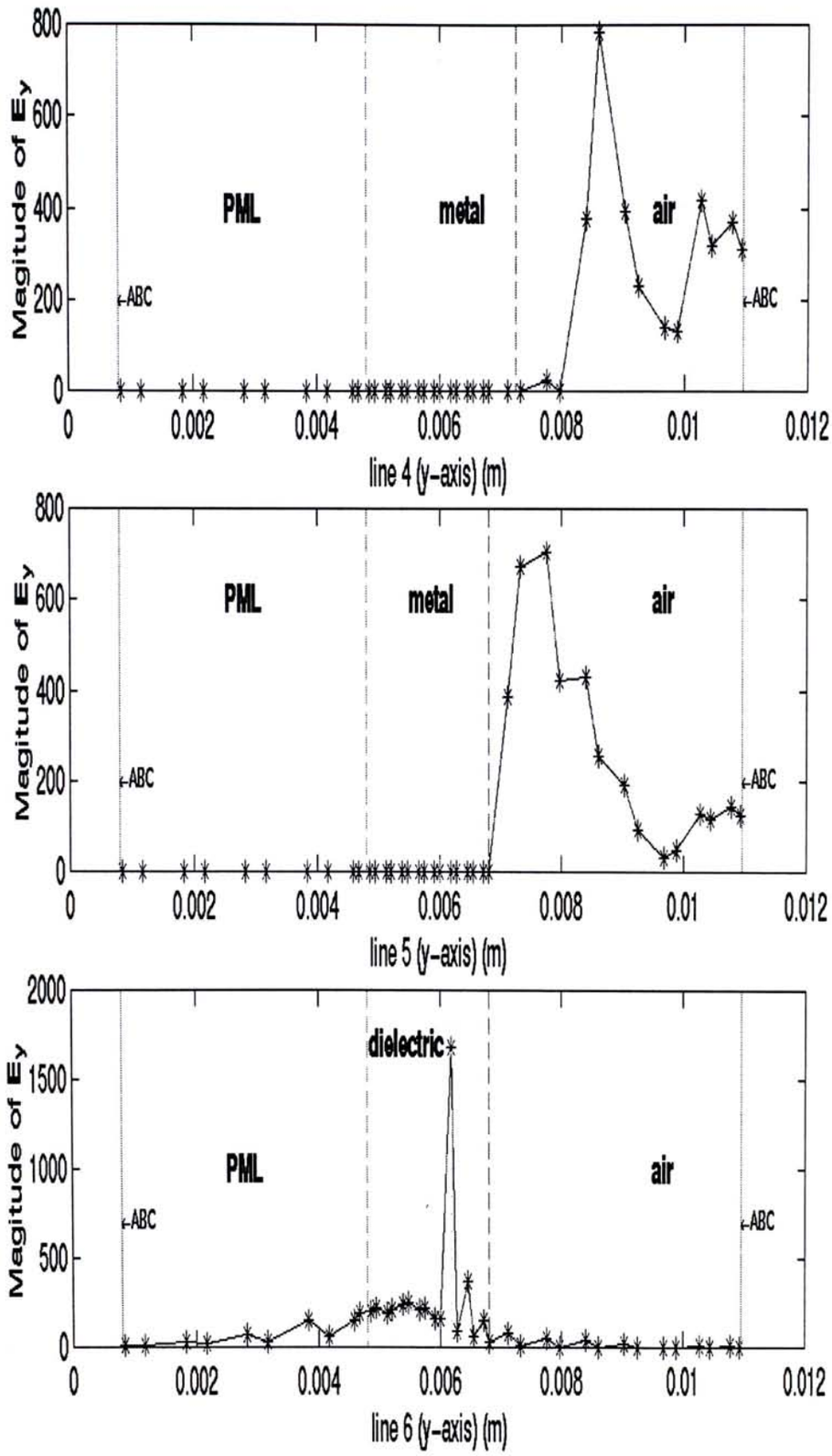

Figure 4. 34 Distribution of electric field of slotline-bowtie junction

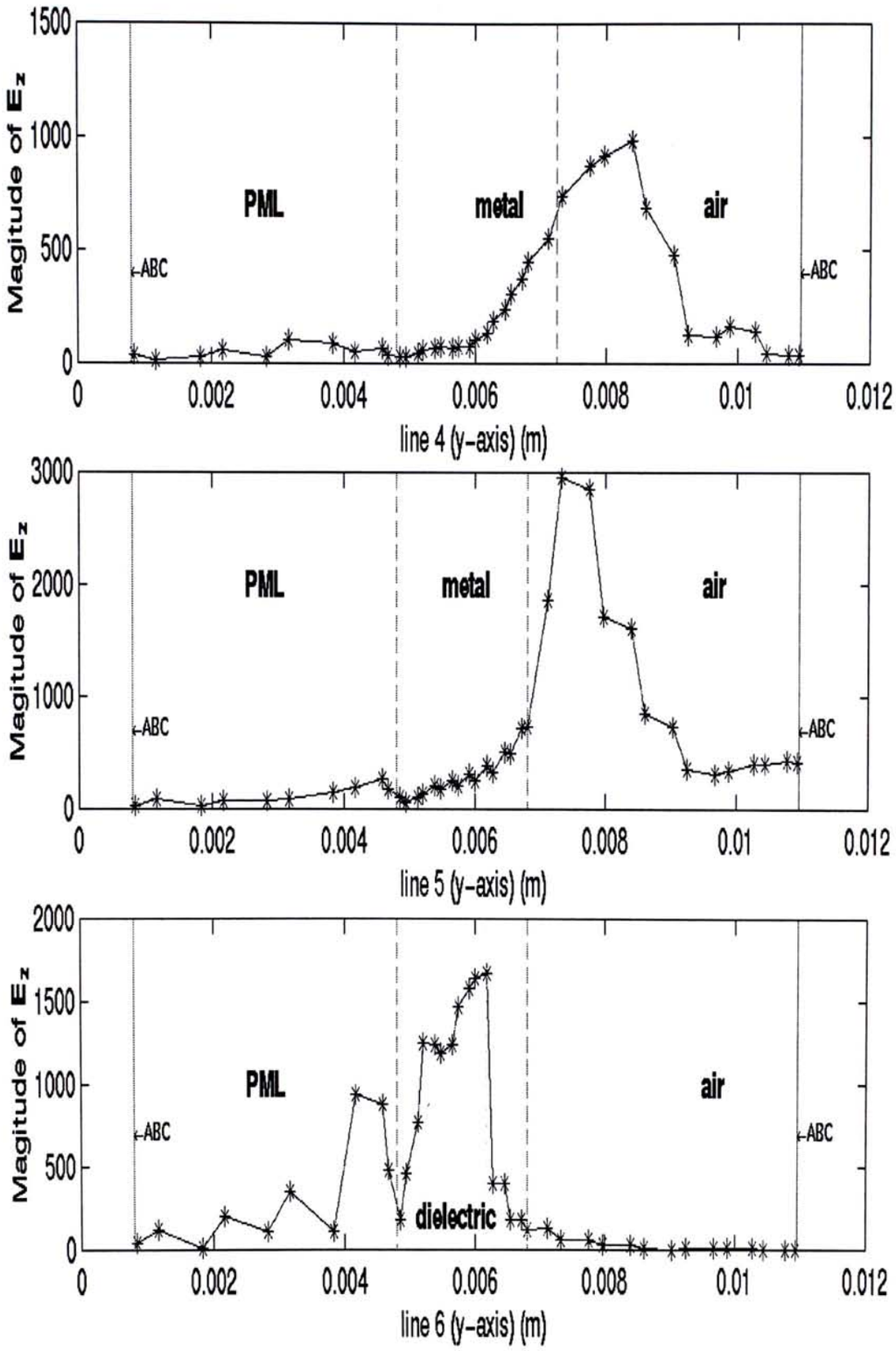

Figure 4. 35 Distribution of electric field of slotline-bowtie junction

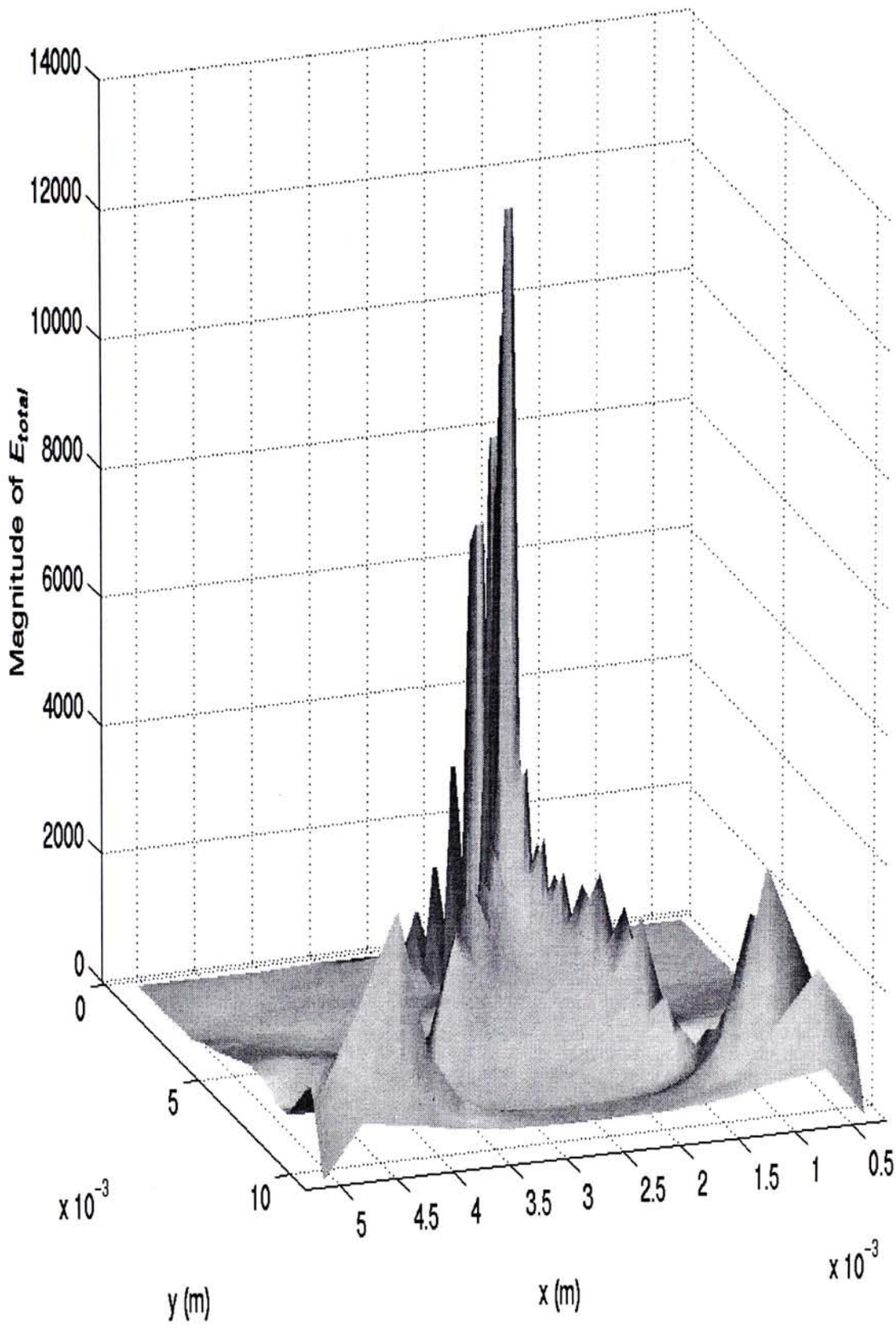

Figure 4. 36 Distribution of electric field of slotline-bowtie junction on the slotline plate level

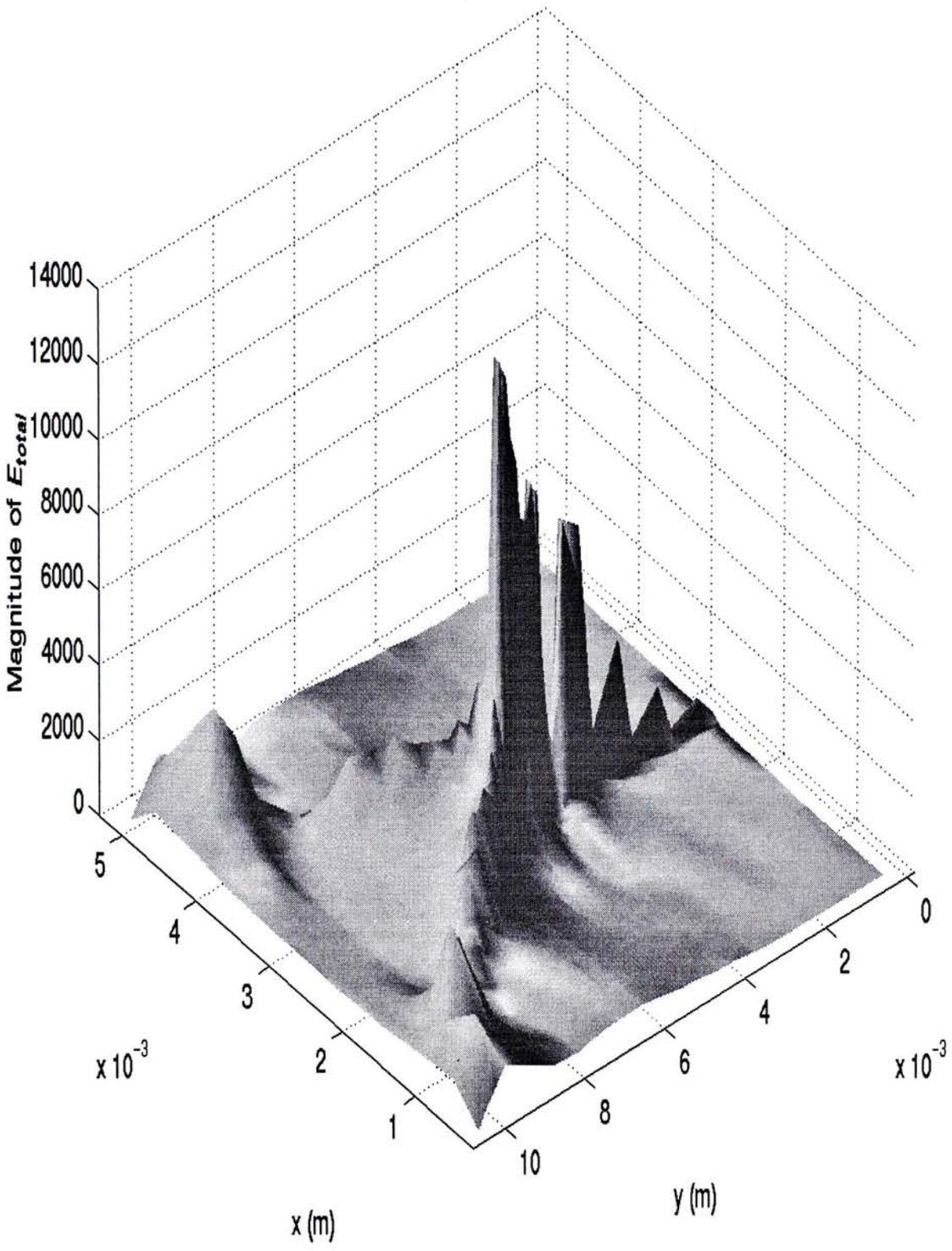

Figure 4. 37 Distribution of electric field of slotline-bowtie junction on the slotline plate level

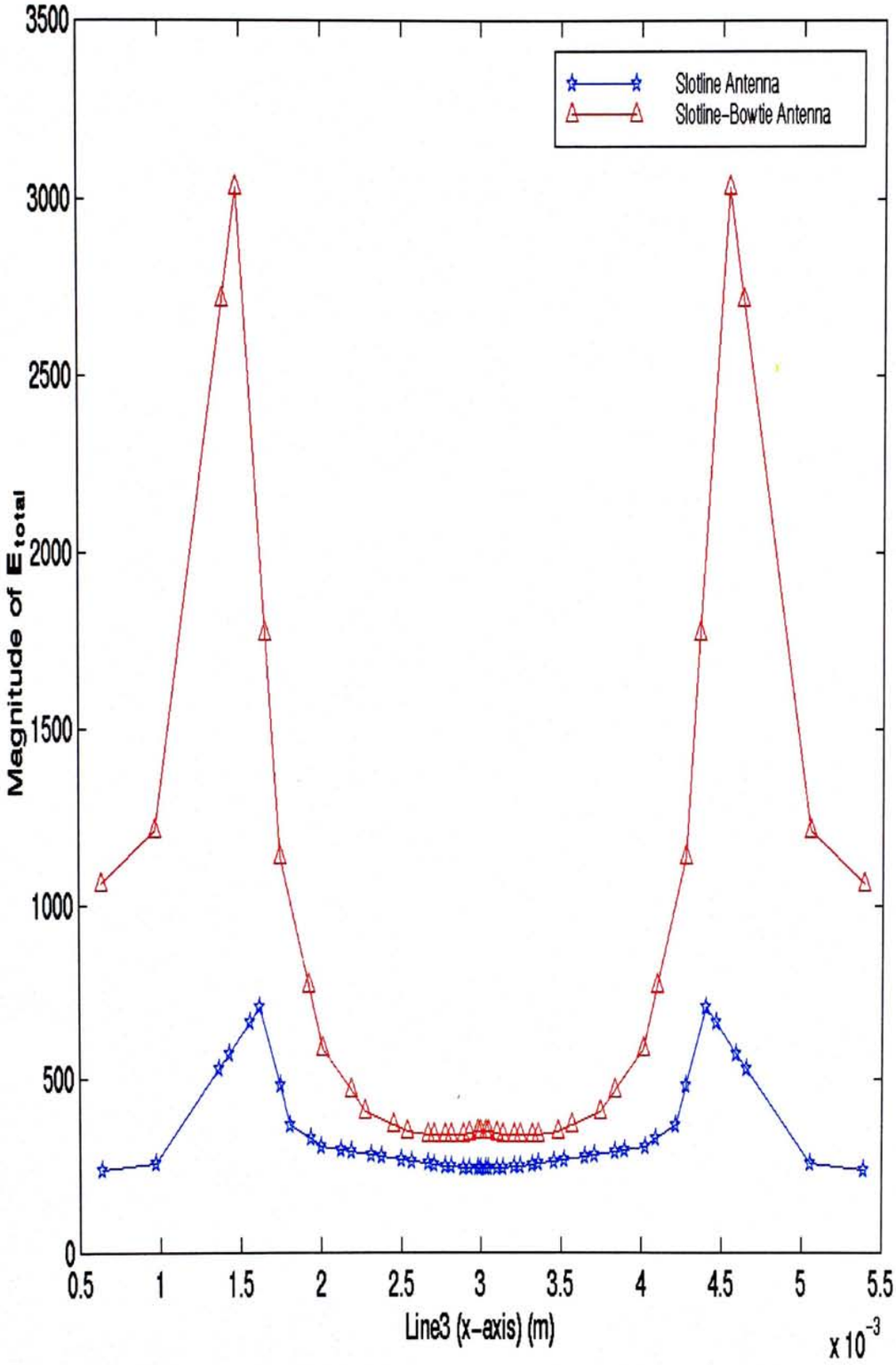

Figure 4. 38 Distribution of electric field on the slotline plate level along line 3

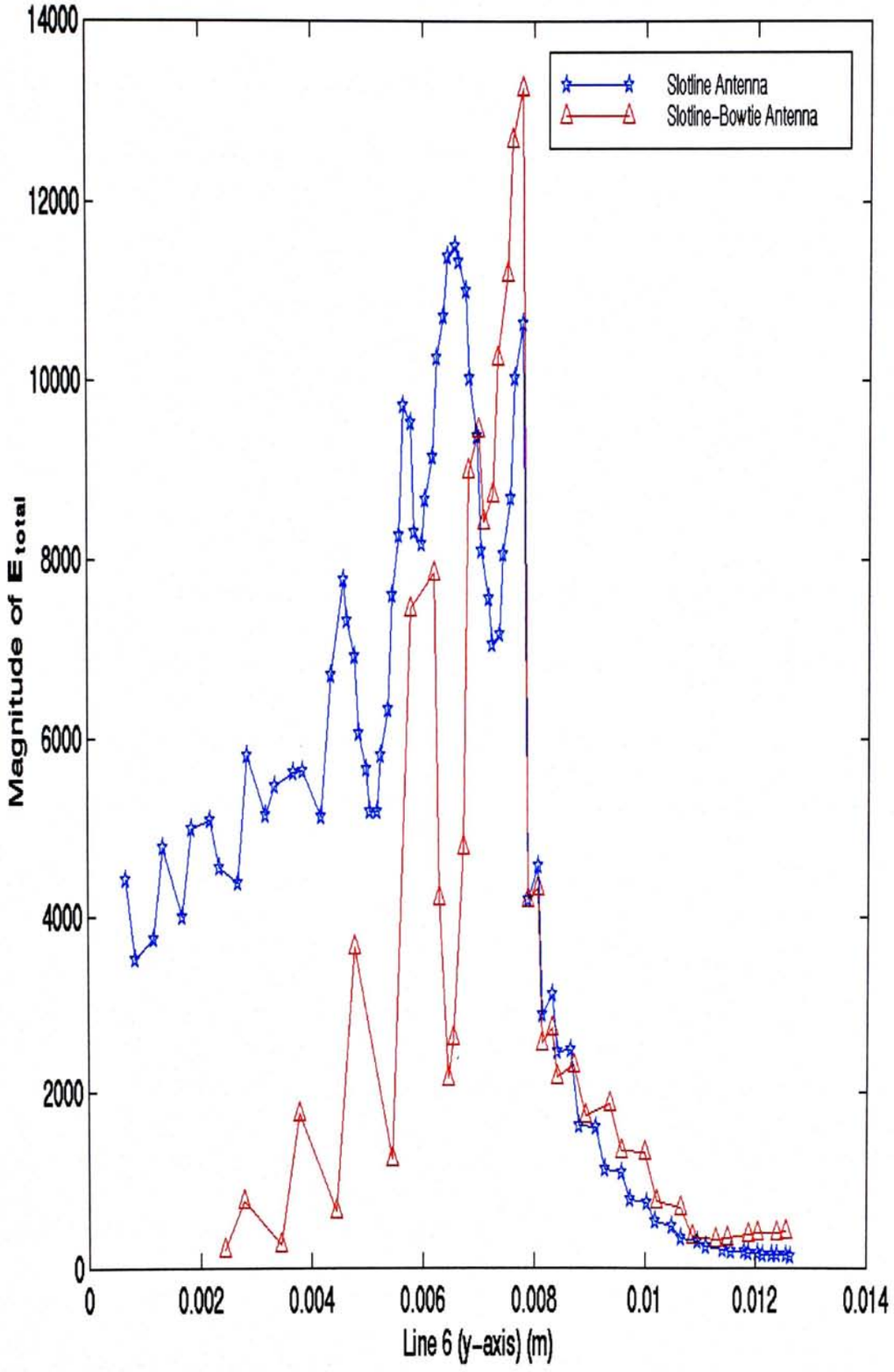

Figure 4. 39 Distribution of electric field on the slotline plate level along line 6

Chapter Five

Conclusion

In this research, we used finite element method to simulate the complicated slotline-bowtie junction. The vector wave equation with boundary conditions was transformed to a functional and solved via Raleigh method. Solution of the problem followed solving of the system of equations.

An artificial fictitious boundary was introduced to absorb all the outgoing fields. ABC and PML have been tested to provide good absorption for a wave excited along the slotline. The best combination of parameters in the PML obtained are as follows: 12 layers of PML and α=1.0 and δ_{max}= 0.8.

Unlike conventional nodal finite element analysis, we employed the new edge elements. The edge element has a special property that its degrees of freedom, instead of being associated with nodes, are related to the edges of the mesh. It is useful in eliminating the occurrence of "spurious modes". Linear triangular and linear tetrahedral elements are used for 2D and 3D respectively.

One important but difficult part in FEM is the mesh discretization. Conventional approach in mesh generation, using Delaunary Triangulation, is too complicated for our study. Instead, a new discretization method was developed in which a rectangular box was cut into six tetrahedrons. It is evident that the new mesh generator works effectively in this project. It is capable of modelling different flare angles of the slotline-bowtie structure. Also, local mesh refinement is possible so that the total edge number can be reduced, the memory minimised and the computation speeded up. Moreover, it is extremely fast, usually takeing less than two seconds However, our mesh generator is not flexible enough to handle objects with round

corners or curved surfaces. Intensive manual input is necessary to define the geometry before any run.

We used MATLAB 5.1 to solve the large system of equations. It takes the full advantages of the sparsity of the matrix and makes use of some powerful algorithms to solve the large sparse matrix. It is capable of solving the problems that only supercomputer can handle with full matrix solver.

Finite element method has been used to successfully model the complicated slotline-bowtie junction for the first time. We also studied the slotline and the slotline with tapered opening. The percentage error in slotline guided wavelength is only 0.9%. These results obtained agree with empirical measurements carried out at the Ohio State University in 1990. For example, the optimal amount of dielectric extension beyond the slotline opening was experimentally determined to be one quarter of a wavelength. We verified that conclusion in this study.

Future Work

In this research, we laid a good foundation for studying the slotline-bowtie hybrid (SHB) antenna. As a next step, we can enhance the radiation of the antenna by optimising the geometric parameters of the slotline-bowtie hybrid. Besides, we have some suggestions for further work to improve the accuracy of the finite element analysis.

1 *PML*:

In section 4.1.2, we found the absorption of PML is strongly related to the combination of the parameters in the PML, such as real part, imaginary part as well as the number of the layer in the PML. In this investigation, we focused on the case that

the incident angle is 90°. In front of the slotline-bowtie hybrid, waves propagate in all directions and we should have taken care of other incident angles. It is advisable to do more work to optimise these parameters, especially for the surface in front of the slotline-bowtie.

2 *Combination of Y-Y microstrip to slotline transition*:

In this project, the slotline-bowtie junction was isolated to examine one section of the radiation behaviour of the antenna. The hybrid was excited by a gap source at a particular frequency. However, in a real antenna, the feed will be an improved Y-Y microstrip to slotline transition which is a broad band source. In a complete study of the slotline-bowtie antenna, we can combine two structures in a single simulation.

3 *Order of polynomial of the finite elements*:

Some researchers pointed out that higher order edge elements performed better than linear ones in terms of accuracy, rate of convergence and mesh density, etc. In this project, second order edge elements can be used in selective region. It may be useful in reducing the total number of edges. The trade-off is the complication in formulation and implementation.

4 *Slotline-Bowtie Antenna*:

In the analysis of the whole antenna, we need to divide the domain into many layers. The size of the system of equations increases rapidly with the number of layers. At the same time, the requirement of memory and time increases quickly. Right now,

we are limited by the capability of the computer in our department. When larger and faster computers come out, this antenna will be more amenable to analysis.

Appendix 1

In this appendix, we attempt to derive expressions for piecewise functions to represent the element trial functions. The unknown quantity ϕ, in element e, is approximated by polynomial

$$\tilde{\phi}^e = \alpha_1^e + \alpha_2^e + \alpha_3^e y + \alpha_4^e z + \alpha_5^e xy + \alpha_6^e yz + \ldots\ldots$$

where α_i^e are coefficients associated with that element. For simplicity, we retain few low order terms and omit all higher orders. This is a good approximation provided the function do vary smoothly and the element size is small enough.

The use of low order polynomials is a popular choice in finite element method due to the ease of formulation and evaluation of element matrices. However, it is evident that, as the order increase, the rate of convergence become faster and/or the mesh density can be decrease[A1.1].

A1.1) 2-Dimensional: Linear Triangle Elements

The unknown function $\tilde{\phi}^s$ within surface element s is approximated as

$$\phi^s \approx \tilde{\phi}^s = a^s + b^s x + c^s y \qquad \text{(A1.1)}$$

where a^s, b^s and c^s are constant coefficients to be determined. Enforcing (A1.1) at the three nodes of the triangle, it becomes

$$\phi_1^s = a^s + b^s x_1^s + c^s y_1^s$$
$$\phi_2^s = a^s + b^s x_2^s + c^s y_2^s$$
$$\phi_3^s = a^s + b^s x_3^s + c^s y_3^s$$

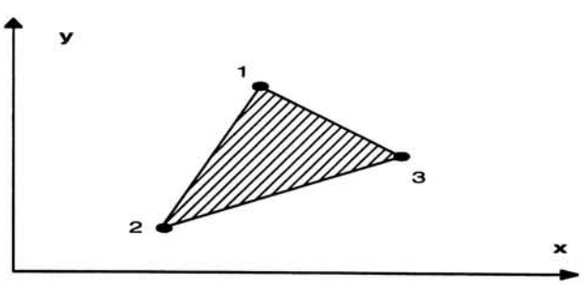

Figure A1.1 The triangular element.

Solving for the constant coefficients a^s, b^s and c^s in terms of nodal values ϕ_j^s, and substituting them back into (A1.1) yields

$$\phi^s(x,y)=\sum_{j=1}^{3} L_j^s(x,y)\phi_j^s \qquad j=1,2,3$$

where $L_j^s(x,y)$ is a *Lagrange Interpolation Polynomial.*

$$L_j^s=\frac{1}{2\Delta^s}(a_j^s+b_j^s x+c_j^s y)$$

in which

$$a_1^s=x_2^s y_3^s-y_2^s x_3^s \qquad a_2^s=x_3^s y_1^s-y_3^s x_1^s \qquad a_3^s=x_1^s y_2^s-y_1^s x_2^s$$
$$b_1^s=y_2^s-y_3^s \qquad b_2^s=y_3^s-y_1^s \qquad b_3^e=y_1^e-y_2^e$$
$$c_1^s=x_3^s-x_2^s \qquad c_2^s=x_1^s-x_3^s \qquad c_3^s=x_2^s-x_1^s$$

and

$$\Delta^s=\frac{1}{2}\begin{vmatrix}1 & x_1^s & y_1^s\\ 1 & x_2^s & y_2^s\\ 1 & x_3^s & y_3^s\end{vmatrix}$$

Similarly, we can obtain the surface interpolation function for *xz* and *yz* plane.

However, it is convenient to write the shape function uniformly as

$$\phi^s=\sum_{j=1}^{3} L_j^s\phi_j^s \qquad j=1,2,3 \qquad \text{(A1.2)}$$

and

$$L_j^s=\frac{1}{2\Delta^s}(a_j^s+b_j^s x+c_j^s y+d_j^s z) \qquad \text{(A1.3)}$$

where

<u>*xy plane*</u>:

$$a_1^s=x_2^s y_3^s-y_2^s x_3^s \qquad b_1^s=y_2^s-y_3^s \qquad c_1^s=x_3^s-x_2^s \qquad d_1^s=0$$
$$a_2^s=x_3^s y_1^s-y_3^s x_1^s \qquad b_2^s=y_3^s-y_1^s \qquad c_2^s=x_1^s-x_3^s \qquad d_2^s=0$$
$$a_3^s=x_1^s y_2^s-y_1^s x_2^s \qquad b_3^s=y_1^s-y_2^s \qquad c_3^s=x_2^s-x_1^s \qquad d_3^s=0$$

xz- plane

$$a_1^s = x_2^s z_3^s - y_2^s z_3^s \qquad b_1^s = z_2^s - z_3^s \qquad c_1^s = 0 \qquad d_1^s = x_3^s - x_2^s$$
$$a_2^s = x_3^s z_1^s - y_3^s z_1^s \qquad b_2^s = z_3^s - z_1^s \qquad c_2^s = 0 \qquad d_2^s = x_1^s - x_3^s$$
$$a_3^s = x_1^s z_2^s - y_1^s z_2^s \qquad b_3^s = z_1^s - z_2^s \qquad c_3^s = 0 \qquad d_3^s = x_2^s - x_1^s$$

yz- plane

$$a_1^s = y_2^s z_3^s - y_3^s z_2^s \qquad b_1^s = 0 \qquad c_1^s = z_2^s - z_3^s \qquad d_1^s = y_3^s - y_2^s$$
$$a_2^s = y_3^s z_1^s - y_1^s z_3^s \qquad b_2^s = 0 \qquad c_2^s = z_3^s - z_1^s \qquad d_2^s = y_1^s - y_3^s$$
$$a_3^s = y_1^s z_2^s - y_2^s z_1^s \qquad b_3^s = 0 \qquad c_3^s = z_1^s - z_2^s \qquad d_3^s = y_2^s - y_1^s$$

and the area of surface element is

$$\Delta^s = \frac{1}{2}\sqrt{\begin{array}{r}\left[(x_1^s - x_2^s)(y_3^s - y_2^s) - (x_3^s - x_2^s)(y_1^s - y_2^s)\right]^2 \\ +\left[(x_3^s - x_2^s)(z_1^s - z_2^s) - (x_1^s - x_2^s)(z_3^s - z_2^s)\right]^2 \\ +\left[(y_1^s - y_2^s)(z_3^s - z_2^s) - (y_3^s - y_2^s)(z_1^s - z_2^s)\right]^2\end{array}}$$

A1.2) 3 Dimensional: Linear tetrahedral element:

In a three dimensional element, a linear trial function is

$$\phi^e(x,y,z) = a^e + b^e x + c^e y + d^e z \qquad \text{(A1.4)}$$

where the coefficients a^e, b^e, c^e and d^e can be determined by enforcing (A1.4) at the four nodes of the element. Denoting the value of ϕ at the j th node as ϕ_j^e, we have

$$\phi_1^e = a^e + b^e x_1^e + c^e y_1^e + d^e z_1^e$$
$$\phi_2^e = a^e + b^e x_2^e + c^e y_2^e + d^e z_2^e$$
$$\phi_3^e = a^e + b^e x_3^e + c^e y_3^e + d^e z_3^e$$
$$\phi_4^e = a^e + b^e x_4^e + c^e y_4^e + d^e z_4^e$$

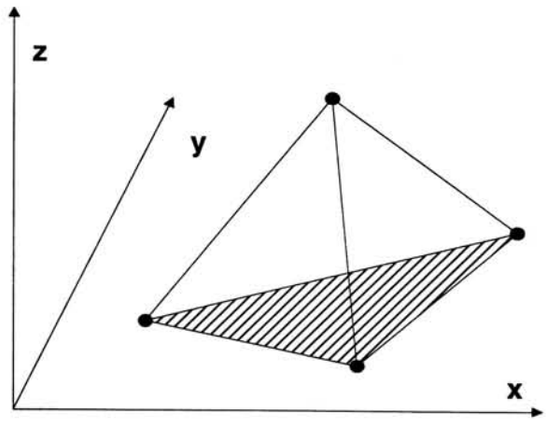

Figure A1.2 A tetrahedral element

from which we have

$$a^e = \frac{1}{6V^e}\begin{vmatrix} \phi_1^e & \phi_2^e & \phi_3^e & \phi_4^e \\ x_1^e & x_2^e & x_3^e & x_4^e \\ y_1^e & y_2^e & y_3^e & y_4^e \\ z_1^e & z_2^e & z_3^e & z_4^e \end{vmatrix} = \frac{1}{6V^e}(a_1^e\phi_1^e + a_2^e\phi_2^e + a_3^e\phi_3^e + a_4^e\phi_4^e)$$

$$b^e = \frac{1}{6V^e}\begin{vmatrix} 1 & 1 & 1 & 1 \\ \phi_1^e & \phi_2^e & \phi_3^e & \phi_4^e \\ y_1^e & y_2^e & y_3^e & y_4^e \\ z_1^e & z_2^e & z_3^e & z_4^e \end{vmatrix} = \frac{1}{6V^e}(b_1^e\phi_1^e + b_2^e\phi_2^e + b_3^e\phi_3^e + b_4^e\phi_4^e)$$

$$c^e = \frac{1}{6V^e}\begin{vmatrix} 1 & 1 & 1 & 1 \\ x_1^e & x_1^e & x_1^e & x_1^e \\ \phi_1^e & \phi_2^e & \phi_3^e & \phi_4^e \\ z_1^e & z_2^e & z_3^e & z_4^e \end{vmatrix} = \frac{1}{6V^e}(c_1^e\phi_1^e + c_2^e\phi_2^e + c_3^e\phi_3^e + c_4^e\phi_4^e)$$

$$d^e = \frac{1}{6V^e}\begin{vmatrix} 1 & 1 & 1 & 1 \\ x_1^e & x_1^e & x_1^e & x_1^e \\ y_1^e & y_2^e & y_3^e & y_4^e \\ \phi_1^e & \phi_2^e & \phi_3^e & \phi_4^e \end{vmatrix} = \frac{1}{6V^e}(d_1^e\phi_1^e + d_2^e\phi_2^e + d_3^e\phi_3^e + d_4^e\phi_4^e)$$

where

$$\begin{aligned}
a_1^e &= x_2^e(y_3^e z_4^e - z_3^e y_4^e) - x_3^e(y_2^e z_4^e - y_4^e z_2^e) + x_4^e(y_2^e z_3^e - y_3^e z_2^e) \\
a_2^e &= -x_1^e(y_3^e z_4^e - z_3^e y_4^e) + x_3^e(y_1^e z_4^e - y_4^e z_1^e) - x_4^e(y_1^e z_3^e - y_3^e z_1^e) \\
a_3^e &= x_1^e(y_2^e z_4^e - z_2^e y_4^e) - x_2^e(y_1^e z_4^e - y_4^e z_1^e) + x_4^e(y_1^e z_2^e - y_2^e z_1^e) \\
a_4^e &= -x_1^e(y_2^e z_3^e - z_2^e y_3^e) + x_2^e(y_1^e z_3^e - y_3^e z_1^e) - x_3^e(y_1^e z_2^e - y_2^e z_1^e)
\end{aligned}$$

$$\begin{aligned}
b_1^e &= -y_3^e z_4^e + y_4^e z_3^e + y_2^e z_4^e - y_4^e z_2^e - y_2^e z_3^e + y_3^e z_2^e \\
b_2^e &= y_3^e z_4^e - y_4^e z_3^e - y_1^e z_4^e + y_4^e z_1^e + y_1^e z_3^e - y_3^e z_1^e \\
b_3^e &= -y_2^e z_4^e + y_4^e z_2^e + y_1^e z_4^e - y_4^e z_1^e - y_1^e z_2^e + y_2^e z_1^e \\
b_4^e &= y_2^e z_3^e - y_3^e z_2^e - y_1^e z_3^e + y_3^e z_1^e + y_1^e z_2^e - y_2^e z_1^e
\end{aligned}$$

$$\begin{aligned}
c_1^e &= x_3^e z_4^e - x_4^e z_3^e - x_2^e z_4^e + x_4^e z_2^e + x_2^e z_3^e - x_3^e z_2^e \\
c_2^e &= -x_3^e z_4^e + x_4^e z_3^e + x_1^e z_4^e - x_4^e z_1^e - x_1^e z_3^e + x_3^e z_1^e \\
c_3^e &= x_2^e z_4^e - x_4^e z_2^e - x_1^e z_4^e + x_4^e z_1^e + x_1^e z_2^e - x_2^e z_1^e \\
c_4^e &= -x_2^e z_3^e + x_3^e z_2^e + x_1^e z_3^e - x_3^e z_1^e - x_1^e z_2^e + x_2^e z_1^e
\end{aligned}$$

$$
\begin{aligned}
d_1^e &= -x_3^e y_4^e + x_4^e y_3^e + x_2^e y_4^e - x_4^e y_2^e - x_2^e y_3^e + x_3^e y_2^e \\
d_2^e &= \quad x_3^e y_4^e - x_4^e y_3^e - x_1^e y_4^e + x_4^e y_1^e + x_1^e y_3^e - x_3^e y_1^e \\
d_3^e &= -x_2^e y_4^e + x_4^e y_2^e + x_1^e y_4^e - x_4^e y_1^e - x_1^e y_2^e + x_2^e y_1^e \\
d_4^e &= \quad x_2^e y_3^e - x_3^e y_2^e - x_1^e y_3^e + x_3^e y_1^e + x_1^e y_2^e - x_2^e y_1^e
\end{aligned}
$$

$$
\begin{aligned}
V^e = \tfrac{1}{6}[\ & x_2^e(y_3^e z_4^e - z_3^e y_4^e) - y_2^e(x_3^e z_4^e - z_3^e x_4^e) + z_2^e(x_3^e y_4^e - x_4^e y_3^e) \\
& - x_1^e(y_3^e z_4^e - z_3^e y_4^e) + y_1^e(x_3^e z_4^e - z_3^e x_4^e) - z_1^e(x_3^e y_4^e - x_4^e y_3^e) \\
& + x_1^e(y_2^e z_4^e - z_2^e y_4^e) - y_1^e(x_2^e z_4^e - z_2^e x_4^e) + z_1^e(x_2^e y_4^e - x_4^e y_2^e) \\
& - x_1^e(y_2^e z_3^e - z_2^e y_3^e) + y_1^e(x_2^e z_3^e - z_2^e x_3^e) - z_1^e(x_2^e y_3^e - x_3^e y_2^e)\ ]
\end{aligned}
$$

Substituting the expressions for a_j^e, b_j^e, c_j^e and d_j^e back into (A1.4), we obtain

$$
\boxed{\phi^e(x,y,z) = \sum_{j=1}^{4} L_j^e(x,y,z)\phi_j^e} \qquad \text{(A1.5)}
$$

where the interpolation functions $L_j^e(x, y, z)$ are expressed as

$$
\boxed{L_j^e(x,y,z) = \frac{1}{6V^e}(a_j^e + b_j^e x + c_j^e y + d_j^e z)} \qquad j = 1, 2, 3, 4 \quad \text{(A1.6)}
$$

Appendix 2

This appendix provides a detail description of all matrix entries. We used tetrahedral edge element to explicitly evaluate the element matrices $[A^e]$, $[AA^e]$ and $[B^e]$ as well as the column vector $\{C^e\}$. Linear edge element shape functions used are

Two dimensional:

$$\vec{N}_i^s = l_i^s (L_{i1}^s \nabla L_{i2}^s - L_{i2}^s \nabla L_{i1}^s) \qquad i=1,2,3$$

$$L_j^s = \frac{1}{2\Delta^s}(a_j^s + b_j^s x + c_j^s y) \qquad j=1,2,3$$

Edge	*Node i1*	*Node i2*
1	1	2
2	2	3
3	3	1

Three dimensional:

$$\vec{N}_i^e = l_i^e (L_{i1}^e \nabla L_{i2}^e - L_{i2}^e \nabla L_{i1}^e) \qquad i=1,2,...,6$$

$$L_j^e(x, y, z) = \frac{1}{6V^e}(a_j^e + b_j^e x + c_j^e y + d_j^e z) \qquad j=1,2,3,4$$

Edge i	*Node i1*	*Node i2*
1	1	2
2	1	3
3	1	4
4	2	3
5	4	2
6	3	4

The reader is referred to Appendix 1 for the expression of the element coefficients ($a_j^s, b_j^s, c_j^s, d_j^s$ and $a_j^e, b_j^e, c_j^e, d_j^e$).

A2.1) Evaluation of $\left[A^e\right]$

$$A_{ij}^e = \iiint_V (\nabla \times \vec{N}_i^e) \cdot \ddot{\mu}_r^{e^{-1}} \cdot (\nabla \times \vec{N}_j^e) dV \qquad i, j = 1, 2 \ldots\ldots 6$$

Note that

$$\nabla \times \vec{N}_i^e = \nabla \times l_i^e \left[L_{i1}^e \nabla L_{i2}^e - L_{i2}^e \nabla L_{i1}^e \right]$$

$$= 2 l_i^e (\nabla L_{i1}^e \times \nabla L_{i2}^e)$$

$$= \frac{2 l_i^e}{\left(6V^e\right)} \left[\hat{i} (c_{i1}^e d_{i2}^e - c_{i2}^e d_{i1}^e) - \hat{j} (b_{i1}^e d_{i2}^e - b_{i2}^e d_{i1}^e) + \hat{k} (b_{i1}^e c_{i2}^e - b_{i2}^e c_{i1}^e) \right]$$

Therefore,

$$A_{ij}^e = \frac{4 l_i^e l_j^e}{1296 (V^e)^3} \Bigg[\frac{1}{\ddot{\mu}_{r\,xx}^e} (c_{i1}^e d_{i2}^e - c_{i2}^e d_{i1}^e)(c_{j1}^e d_{j2}^e - c_{j2}^e d_{j1}^e)$$

$$+ \frac{1}{\ddot{\mu}_{r\,yy}^e} (b_{i1}^e d_{i2}^e - b_{i2}^e d_{i1}^e)(b_{j1}^e d_{j2}^e - b_{j2}^e d_{j1}^e)$$

$$+ \frac{1}{\ddot{\mu}_{r\,zz}^e} (b_{i1}^e c_{i2}^e - b_{i2}^e c_{i1}^e)(b_{j1}^e c_{j2}^e - b_{j2}^e c_{j1}^e) \Bigg]$$

In general,

$$A_{ij}^e = A_{ji}^e \qquad i, j = 1,2,\ldots,6$$

A2.2) Evaluation of $\left[AA^e\right]$

$$AA_{ij}^e = -k_0^2 \cdot \iiint_V \vec{N}_i^e \cdot \ddot{\varepsilon}_r \cdot \vec{N}_j^e dV \qquad i, j = 1, 2 \ldots\ldots 6$$

We first calculate the quantity

$$\vec{N}_i^e \cdot \ddot{\varepsilon}_r^e \cdot \vec{N}_j^e = l_i^e l_j^e \left[(L_{i1}^e \nabla L_{i2}^e - L_{i2}^e \nabla L_{i1}^e) \cdot \ddot{\varepsilon}_r^e \cdot (L_{j1}^e \nabla L_{j1}^e - L_{j2}^e \nabla L_{i1}^e) \right]$$

$$= \frac{l_i^e l_j^e}{(6V^e)^2} \left[L_{i1}^e L_{j1}^e f_{i2,j2} - L_{i1}^e L_{j2}^e f_{i2,j1} - L_{i2}^e L_{j1}^e f_{i1,j2} - L_{i2}^e L_{j2}^e f_{i1,j1} \right]$$

since the dyadic relative permittivity $\ddot{\varepsilon}_r^e$ is assumed to be diagonal tensor, we define

$$f_{I,II} = \varepsilon_{xx}^e b_I^e b_{II}^e + \varepsilon_{yy}^e c_I^e c_{II}^e + \varepsilon_{zz}^e d_I^e d_{II}^e \qquad I,II = 1,2,\ldots,6$$

then the matrix coefficient can be rewritten as

$$AA_{ij}^e = -k_0^2 \cdot \frac{l_i^e l_j^e}{(6V^e)^2}[\quad f_{i2,j2}\iiint_{V^e} L_{i1}^e L_{j1}^e dV - f_{i2,j1}\iiint_{V^e} L_{i1}^e L_{j2}^e dV$$
$$- f_{i1,j2}\iiint_{V^e} L_{i2}^e L_{j1}^e dV - f_{i1,j1}\iiint_{V^e} L_{i2}^e L_{j2}^e dV\ ]$$

With the aid of an useful formula [A2.1] to be used in this procedure is

$$\iiint_{V^e} \left(L_1^e\right)^a \left(L_2^e\right)^b \left(L_3^e\right)^c \left(L_4^e\right)^d dV = \frac{a!b!c!d!}{(a+b+c+d+3)!} 6V^e$$

Thus

$$AA_{11}^e = \frac{-k_0^2 (l_1^e)^2}{360V^e}(f_{22} - f_{12} + f_{11})$$

$$AA_{12}^e = \frac{-k_0^2 l_1^e l_2^e}{720V^e}(2f_{23} - f_{21} - f_{13} + f_{11})$$

$$AA_{13}^e = \frac{-k_0^2 l_1^e l_3^e}{720V^e}(2f_{24} - f_{21} - f_{14} + f_{11})$$

$$AA_{14}^e = \frac{-k_0^2 l_1^e l_4^e}{720V^e}(f_{23} - f_{22} - 2f_{13} + f_{12})$$

$$AA_{15}^e = \frac{-k_0^2 l_1^e l_5^e}{720V^e}(f_{22} - f_{24} - f_{12} + 2f_{14})$$

$$AA_{16}^e = \frac{-k_0^2 l_1^e l_5^e}{720V^e}(f_{24} - f_{23} - f_{14} + f_{13})$$

$$AA_{22}^e = \frac{-k_0^2 (l_2^e)^2}{360V^e}(f_{33} - f_{13} + f_{11})$$

$$AA_{23}^e = \frac{-k_0^2 l_2^e l_3^e}{720V^e}(2f_{34} - f_{13} - f_{14} + f_{11})$$

$$AA_{24}^{e} = \frac{-k_0^2 l_2^e l_4^e}{360V^e}(f_{33} - f_{23} - f_{13} + 2f_{12})$$

$$AA_{25}^{e} = \frac{-k_0^2 l_2^e l_5^e}{720V^e}(f_{23} - f_{34} - f_{12} + f_{14})$$

$$AA_{26}^{e} = \frac{-k_0^2 l_2^e l_6^e}{720V^e}(f_{34} - f_{33} - 2f_{14} + f_{13})$$

$$AA_{33}^{e} = \frac{-k_0^2 (l_3^e)^2}{360V^e}(f_{44} - f_{14} + f_{11})$$

$$AA_{34}^{e} = \frac{-k_0^2 l_3^e l_4^e}{720V^e}(f_{34} - f_{24} - f_{13} + f_{12})$$

$$AA_{35}^{e} = \frac{-k_0^2 l_3^e l_5^e}{720V^e}(f_{24} - f_{44} - 2f_{12} + f_{14})$$

$$AA_{36}^{e} = \frac{-k_0^2 l_3^e l_6^e}{720V^e}(f_{44} - f_{34} - f_{14} + 2f_{13})$$

$$AA_{44}^{e} = \frac{-k_0^2 (l_4^e)^2}{360V^e}(f_{33} - f_{23} + f_{22})$$

$$AA_{45}^{e} = \frac{-k_0^2 l_4^e l_5^e}{720V^e}(f_{23} - 2f_{34} - f_{22} + f_{24})$$

$$AA_{46}^{e} = \frac{-k_0^2 l_4^e l_6^e}{720V^e}(f_{34} - f_{33} - 2f_{24} + f_{23})$$

$$AA_{55}^{e} = \frac{-k_0^2 (l_5^e)^2}{360V^e}(f_{22} - f_{24} + f_{44})$$

$$AA_{56}^{e} = \frac{-k_0^2 l_5^e l_6^e}{720V^e}(f_{24} - 2f_{23} - f_{44} + f_{34})$$

$$AA_{66}^{e} = \frac{-k_0^2 (l_6^e)^2}{360V^e}(f_{44} - f_{34} + f_{33})$$

In general,

$$AA_{ij}^{e} = AA_{ji}^{e} \qquad i, j = 1,2,\ldots,6$$

A2.3) Evaluation of $\left[B^s\right]$

$$B_{ij}^s = jk_0 \cos\theta_i \iint_S (\hat{n}\times\vec{N}_i^s)(\hat{n}\times\vec{N}_j^s)dS$$

Note that the normal vector of the element can be written as

$\hat{n} = n_x\hat{i} + n_y\hat{j} + n_k\hat{k}$. Consider

$$\Gamma_{ij}^s = (\hat{n}\times\vec{N}_i^s)\cdot(\hat{n}\times\vec{N}_j^s)$$

$$\begin{aligned}
&= \frac{l_i^s l_j^s}{(2\Delta^s)^2}\times[\ (n_x^2+n_z^2)(L_{i1}^s c_{i2}^s - L_{i2}^s c_{i1}^s)(L_{j1}^s c_{j2}^s - L_{j2}^s c_{j1}^s)\\
&\quad +(n_x^2+n_y^2)(L_{i1}^s d_{i2}^s - L_{i2}^s d_{i1}^s)(L_{j1}^s d_{j2}^s - L_{j2}^s d_{j1}^s)\\
&\quad +(n_y^2+n_z^2)(L_{i1}^s b_{i2}^s - L_{i2}^s b_{i1}^s)(L_{j1}^s b_{j2}^s - L_{j2}^s b_{j1}^s)\\
&\quad -n_y n_z(L_{i1}^s c_{i2}^s - L_{i2}^s c_{i1}^s)(L_{j1}^s d_{j2}^s - L_{j2}^s d_{j1}^s)+(L_{i1}^s d_{i2}^s - L_{i2}^s d_{i1}^s)(L_{j1}^s c_{j2}^s - L_{j2}^s c_{j1}^s)\\
&\quad -n_x n_z(L_{i1}^s b_{i2}^s - L_{i2}^s b_{i1}^s)(L_{j1}^s d_{j2}^s - L_{j2}^s d_{j1}^s)+(L_{i1}^s d_{i2}^s - L_{i2}^s d_{i1}^s)(L_{j1}^s b_{j2}^s - L_{j2}^s b_{j1}^s)\\
&\quad -n_y n_z(L_{i1}^s b_{i2}^s - L_{i2}^s b_{i1}^s)(L_{j1}^s c_{j2}^s - L_{j2}^s c_{j1}^s)+(L_{i1}^s c_{i2}^s - L_{i2}^s c_{i1}^s)(L_{j1}^s b_{j2}^s - L_{j2}^s b_{j1}^s)\ \ ]
\end{aligned}$$

another useful formula to be used in this procedure [A2.1] is

$$\iiint_s \left(L_1^s\right)^l\left(L_2^s\right)^m\left(L_3^s\right)^n dS = \frac{l!m!n!}{(l+m+n+2)!}2\Delta^s$$

Finally,

$$\begin{aligned}
B_{11}^s &= \frac{jk_0\cos\theta_a\left(l_1^s\right)^2}{24\Delta^s}\times[\ \ (n_y^2+n_z^2)(b_1^{s\,2}+b_2^{s\,2}-b_1^s b_2^s)\\
&\quad +(n_x^2+n_z^2)(c_1^{s\,2}+c_2^{s\,2}-c_1^s c_2^s)\\
&\quad +(n_x^2+n_y^2)(d_1^{s\,2}+d_2^{s\,2}-d_1^s d_2^s)\\
&\quad -n_y n_z(2c_1^s d_1^s+2c_2^s d_2^s-c_1^s d_2^s-c_2^s d_1^s)\\
&\quad -n_x n_z(2b_1^s d_1^s+2b_2^s d_2^s-b_1^s d_2^s-b_2^s d_1^s)\\
&\quad -n_x n_y(2b_1^s c_1^s+2b_2^s c_2^s-b_1^s c_2^s-b_2^s c_1^s)\ \ ]
\end{aligned}$$

$$\begin{aligned}
B_{12}^s &= \frac{jk_0\cos\theta_a l_1^s l_2^s}{48\Delta^s}\times[\ \ (n_y^2+n_z^2)(b_2^s b_3^s-b_2^{s\,2}-2b_1^s b_3^s+b_1^s b_2^s)\\
&\quad +(n_x^2+n_z^2)(c_2^s c_3^s-c_2^{s\,2}-2c_1^s c_3^s+c_1^s c_2^s)\\
&\quad +(n_x^2+n_y^2)(d_2^s d_3^s-d_2^{s\,2}-2d_1^s d_3^s+d_1^s d_2^s)\\
&\quad -n_y n_z(c_2^s d_3^s+c_3^s d_2^s-2c_2^s d_2^s-2c_1^s d_3^s-2c_3^s d_1^s+c_1^s d_2^s+c_2^s d_1^s)\\
&\quad -n_x n_z(b_2^s d_3^s+b_3^s d_2^s-2b_2^s d_2^s-2b_1^s d_3^s-2b_3^s d_1^s+b_1^s d_2^s+b_2^s d_1^s)\\
&\quad -n_x n_y(b_2^s c_3^s+b_3^s c_2^s-2b_2^s c_2^s-2b_1^s c_3^s-2b_3^s c_1^s+b_1^s c_2^s+b_2^s c_1^s)\ \ ]
\end{aligned}$$

$$B_{13}^s = \frac{jk_0 \cos\theta_a l_1^s l_3^s}{48\Delta^s} \times \Big[\quad (n_y^2 + n_z^2)(b_1^s b_2^s - b_1^{s\,2} - 2b_2^s b_3^s + b_1^s b_3^s)$$
$$+(n_x^2 + n_z^2)(c_1^s c_2^s - c_1^{s\,2} - 2c_2^s c_3^s + c_1^s c_3^s)$$
$$+(n_x^2 + n_y^2)(d_1^s d_2^s - d_1^{s\,2} - 2d_2^s d_3^s + d_1^s d_3^s)$$
$$-n_y n_z(c_2^s d_1^s + c_1^s d_2^s - 2c_1^s d_1^s - 2c_2^s d_3^s - 2c_3^s d_2^s + c_1^s d_3^s + c_3^s d_1^s)$$
$$-n_x n_z(b_2^s d_1^s + b_1^s d_2^s - 2b_1^s d_1^s - 2b_2^s d_3^s - 2b_3^s d_2^s + b_1^s d_3^s + b_3^s d_1^s)$$
$$-n_x n_y(b_2^s c_1^s + b_1^s c_2^s - 2b_1^s c_1^s - 2b_2^s c_3^s - 2b_3^s c_2^s + b_1^s c_3^s + b_3^s c_1^s) \quad \Big]$$

$$B_{22}^s = \frac{jk_0 \cos\theta_a (l_2^s)^2}{24\Delta^s} \times \Big[\quad (n_y^2 + n_z^2)(b_2^{s\,2} + b_3^{s\,2} - b_2^s b_3^s)$$
$$+(n_x^2 + n_z^2)(c_2^{s\,2} + c_3^{s\,2} - c_2^s c_3^s)$$
$$+(n_x^2 + n_y^2)(d_2^{s\,2} + d_3^{s\,2} - d_2^s d_3^s)$$
$$-n_y n_z(2c_2^s d_2^s + 2c_3^s d_3^s - c_2^s d_3^s - c_3^s d_2^s)$$
$$-n_x n_z(2b_2^s d_2^s + 2b_3^s d_3^s - b_2^s d_3^s - b_3^s d_2^s)$$
$$-n_x n_y(2b_2^s c_2^s + 2b_3^s c_3^s - b_2^s c_3^s - b_3^s c_2^s) \quad \Big]$$

$$B_{23}^s = \frac{jk_0 \cos\theta_a l_2^s l_3^s}{48\Delta^s} \times \Big[\quad (n_y^2 + n_z^2)(b_1^s b_3^s - b_3^{s\,2} - 2b_1^s b_2^s + b_2^s b_3^s)$$
$$+(n_x^2 + n_z^2)(c_1^s c_3^s - c_3^{s\,2} - 2c_1^s c_2^s + c_2^s c_3^s)$$
$$+(n_x^2 + n_y^2)(d_1^s d_3^s - d_3^{s\,2} - 2d_1^s d_2^s + d_2^s d_3^s)$$
$$-n_y n_z(c_3^s d_1^s + c_1^s d_3^s - 2c_3^s d_3^s - 2c_1^s d_2^s - 2c_2^s d_1^s + c_2^s d_3^s + c_3^s d_2^s)$$
$$-n_x n_z(b_3^s d_1^s + b_1^s d_3^s - 2b_3^s d_3^s - 2b_1^s d_2^s - 2b_2^s d_1^s + b_2^s d_3^s + b_3^s d_2^s)$$
$$-n_x n_y(b_3^s c_1^s + b_1^s c_3^s - 2b_3^s c_3^s - 2b_1^s c_2^s - 2b_2^s c_1^s + b_2^s c_3^s + b_3^s c_2^s) \quad \Big]$$

$$B_{33}^s = \frac{jk_0 \cos\theta_a (l_3^s)^2}{24\Delta^s} \Big[\quad (n_y^2 + n_z^2)(b_1^{s\,2} + b_3^{s\,2} - b_1^s b_3^s)$$
$$+(n_x^2 + n_z^2)(c_1^{s\,2} + c_3^{s\,2} - c_1^s c_3^s)$$
$$+(n_x^2 + n_y^2)(d_1^{s\,2} + d_3^{s\,2} - d_1^s d_3^s)$$
$$-n_x n_z(2b_1^s d_1^s + 2b_3^s d_3^s - b_1^s d_3^s - b_3^s d_1^s)$$
$$-n_y n_z(2c_1^s d_1^s + 2c_3^s d_3^s - c_1^s d_3^s - c_3^s d_1^s)$$
$$-n_x n_y(2b_1^s c_1^s + 2b_3^s c_3^s - b_1^s c_3^s - b_3^s c_1^s) \quad \Big]$$

In general,

$$B_{ij}^s = B_{ji}^s \qquad i,j=1,2,3$$

A2.4) Evaluation of $\{C^e\}$

$$C_i^e = -j\mu_0\omega_0 \iiint_V \vec{N}^e \cdot \vec{J} dV \qquad i = 1,2,\ldots,6$$

Assume that the current density $\vec{J}$ is parallel to x axis, i.e., $\vec{J} = I\hat{i}$,where I denotes the magnitude of the current. Thus the vector entries are given as

$$\boxed{c_i^e = \frac{-jk_0 Z_0 I}{24} l_i^e (b_{i2}^e - b_{i1}^e)} \qquad i=1,2,\ldots,6$$

Appendix 3

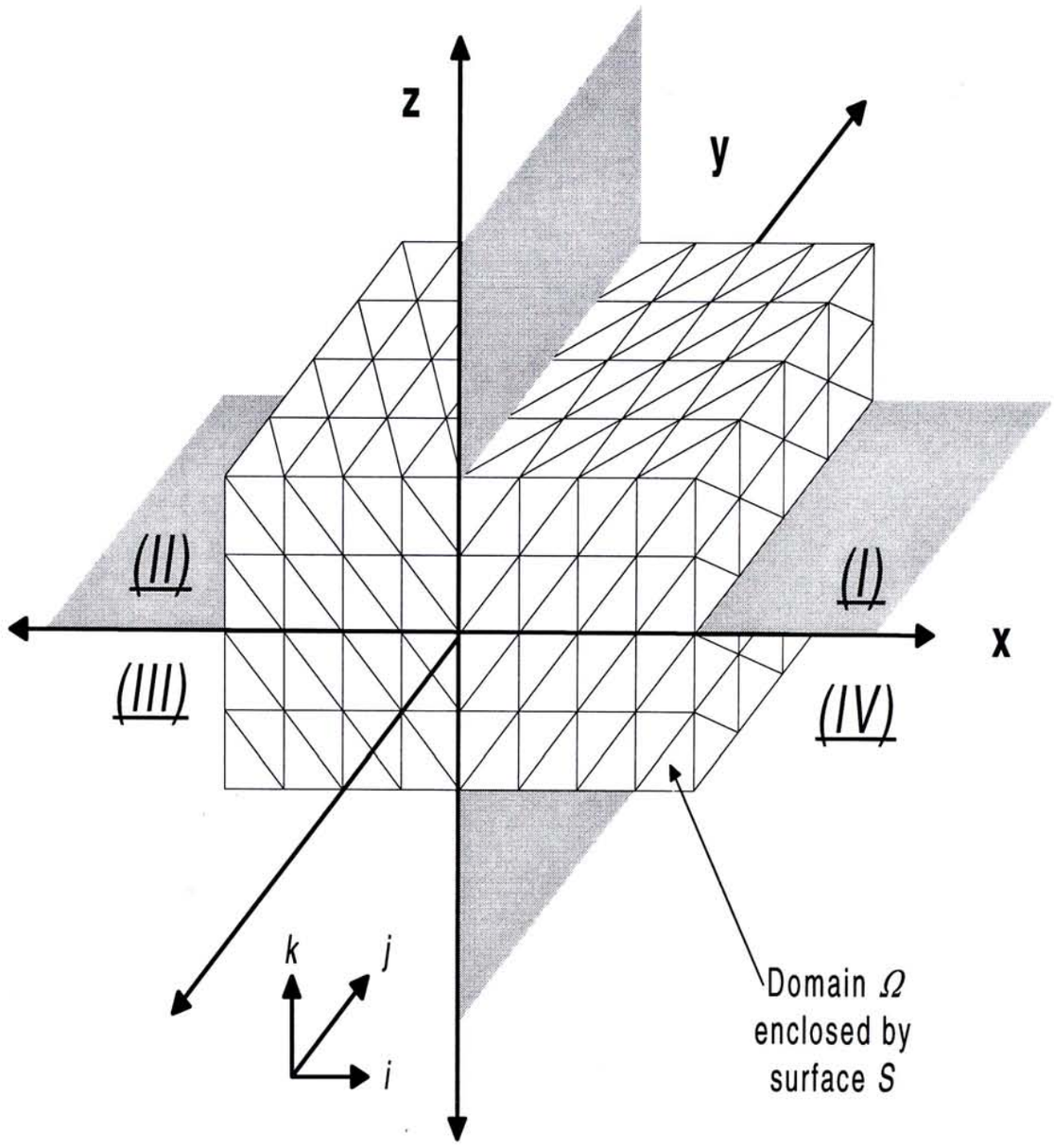

Figure A3.1 Domain Ω is divided into four quadrants (I, II, III and IV).

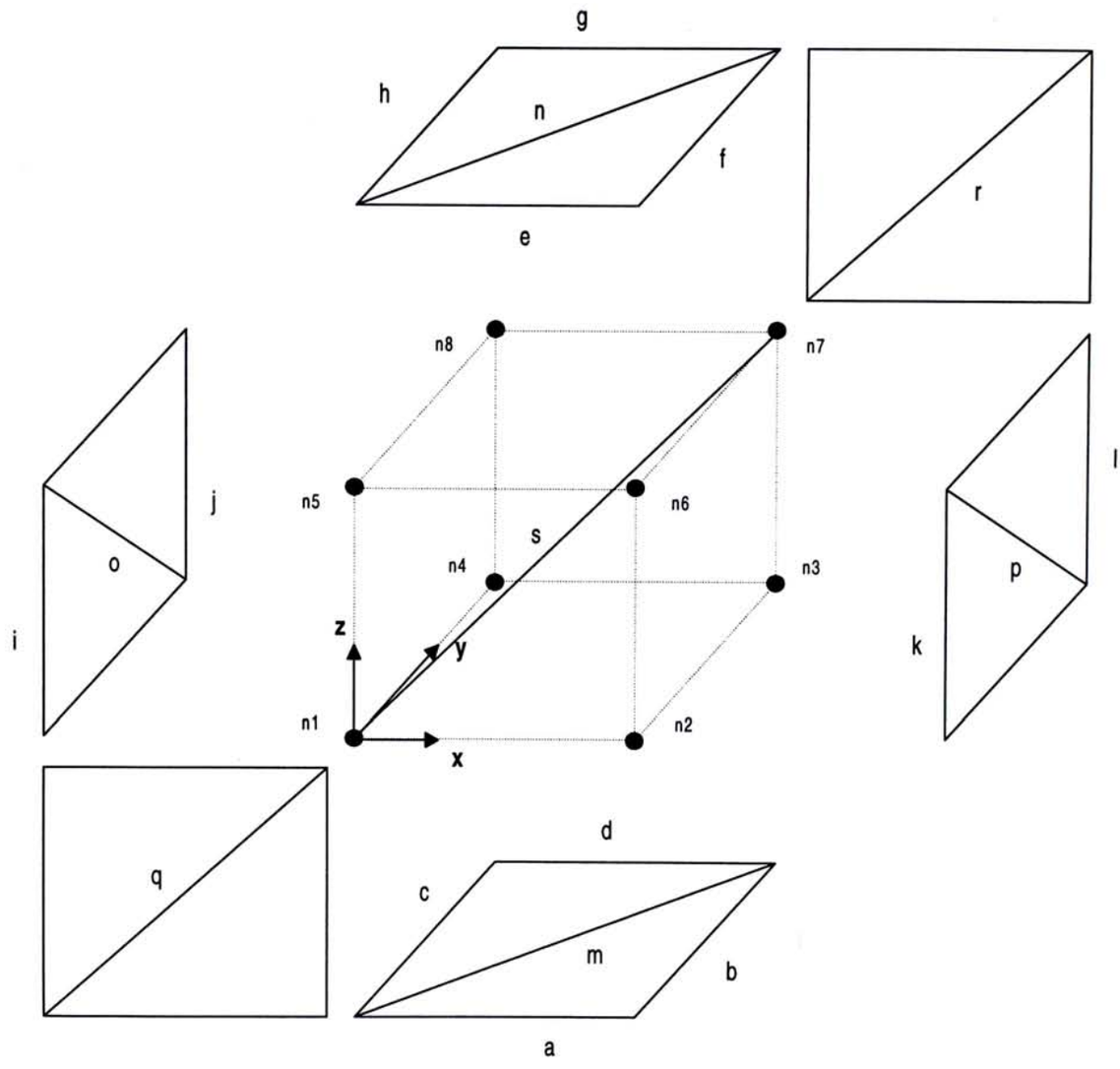

Figure A3.2 Edge arrangement in quadrant (I)

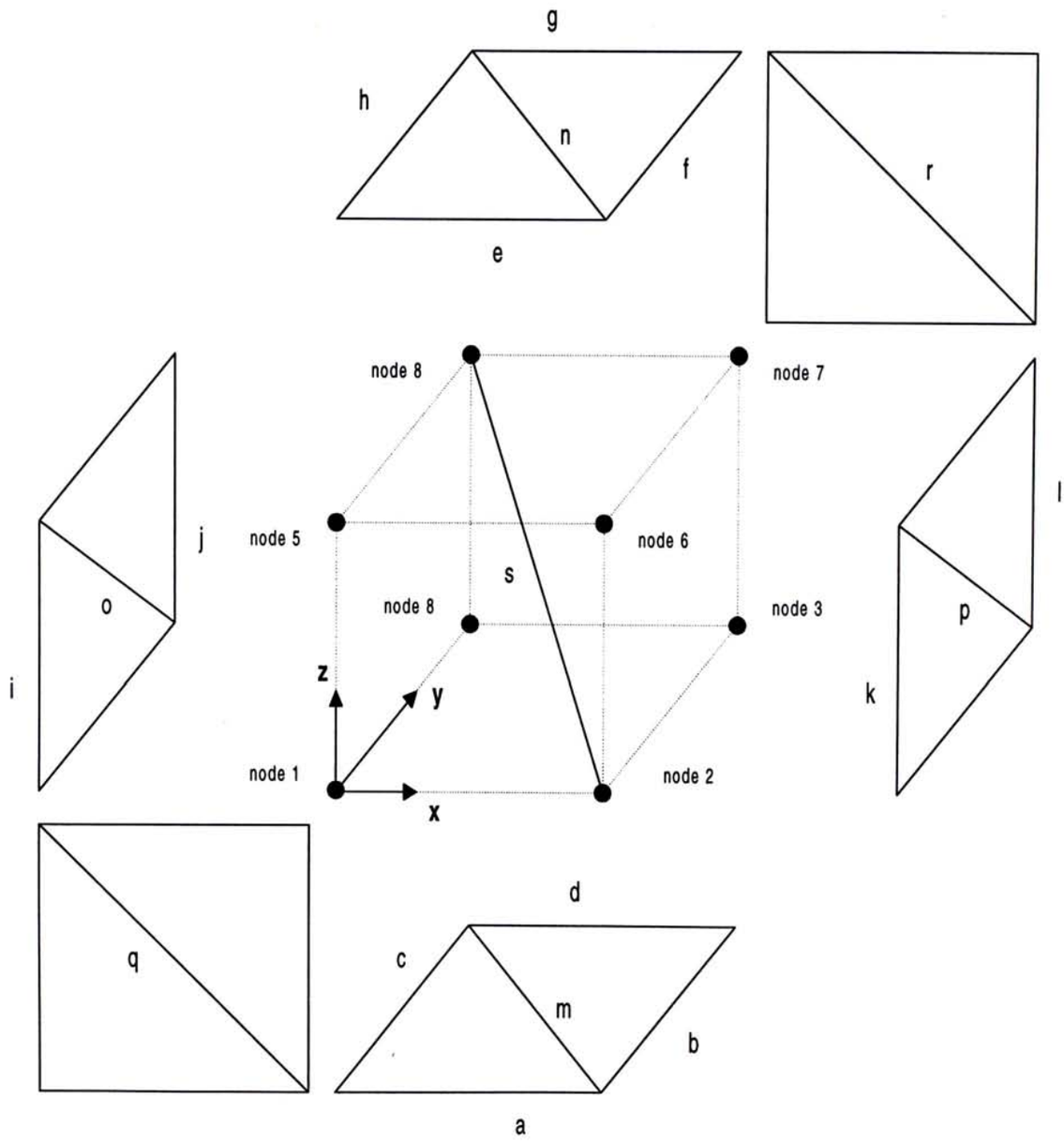

Figure A3.3 Edge arrangement in quadrant (II)

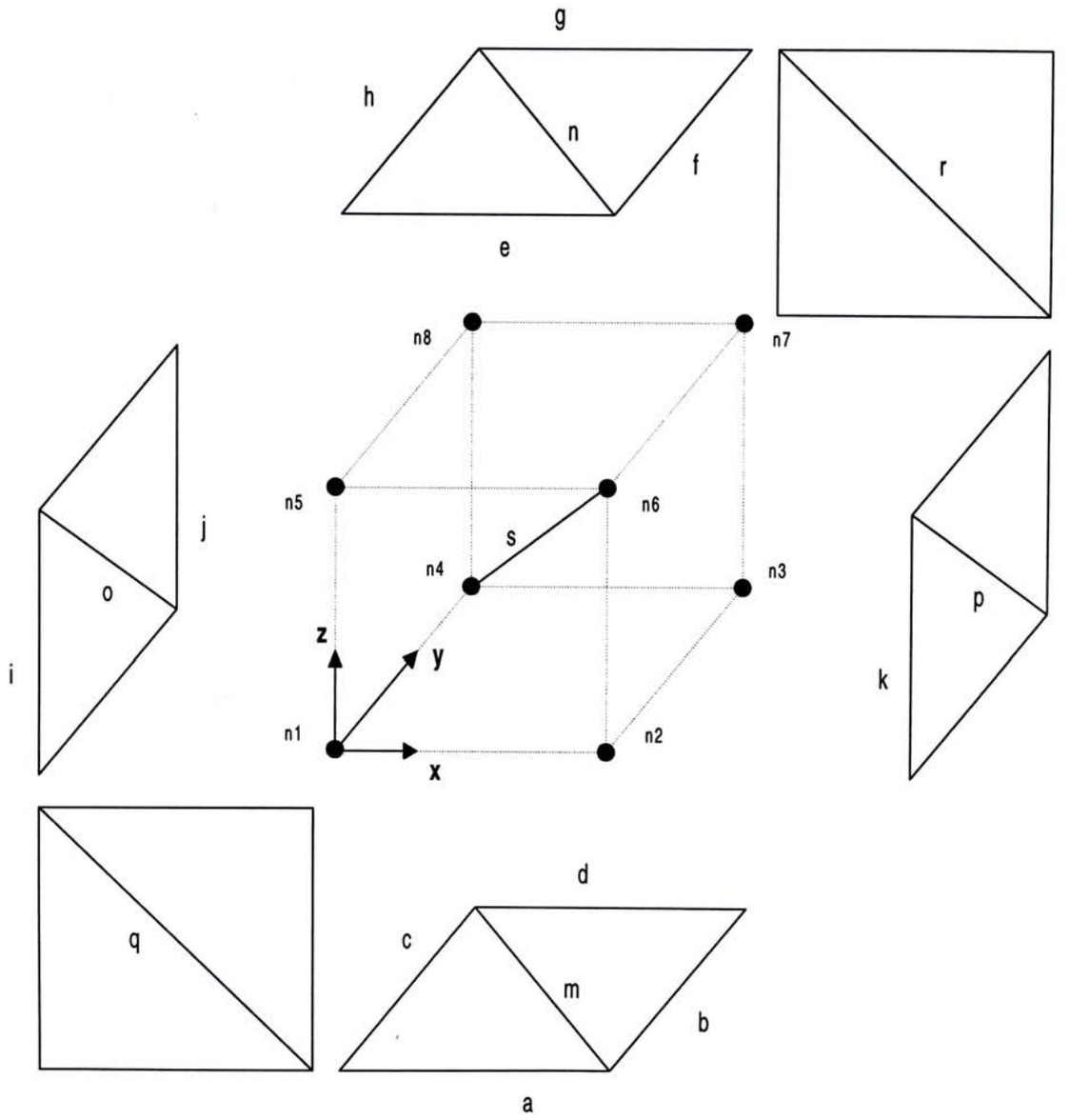

Figure A3.4 Edge arrangement in quadrant (III)

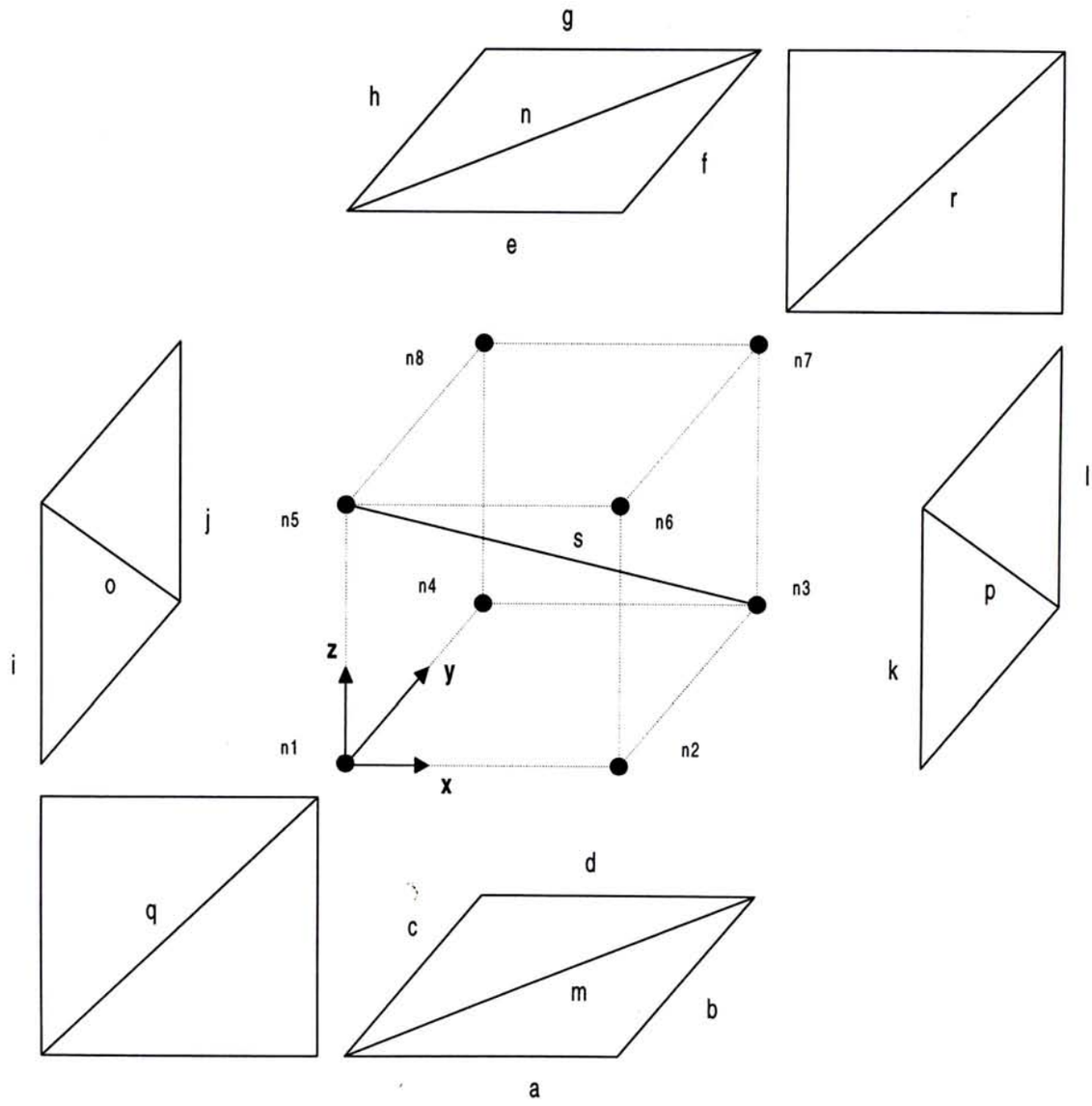

Figure A3.5 Edge arrangement in quadrant (IV)

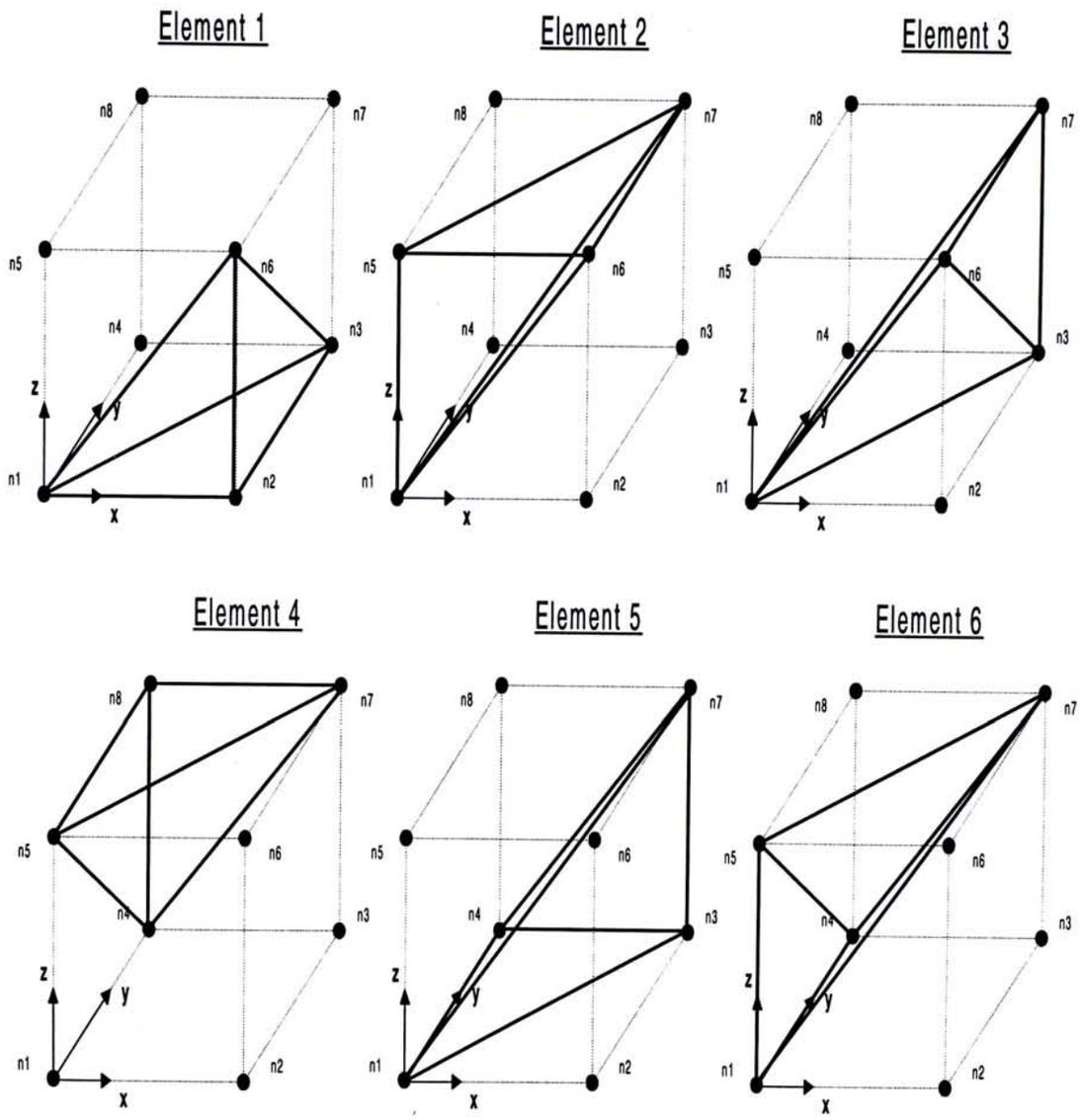

Figure A3.6 Arrangement of tetrahedrons in quadrant (I)

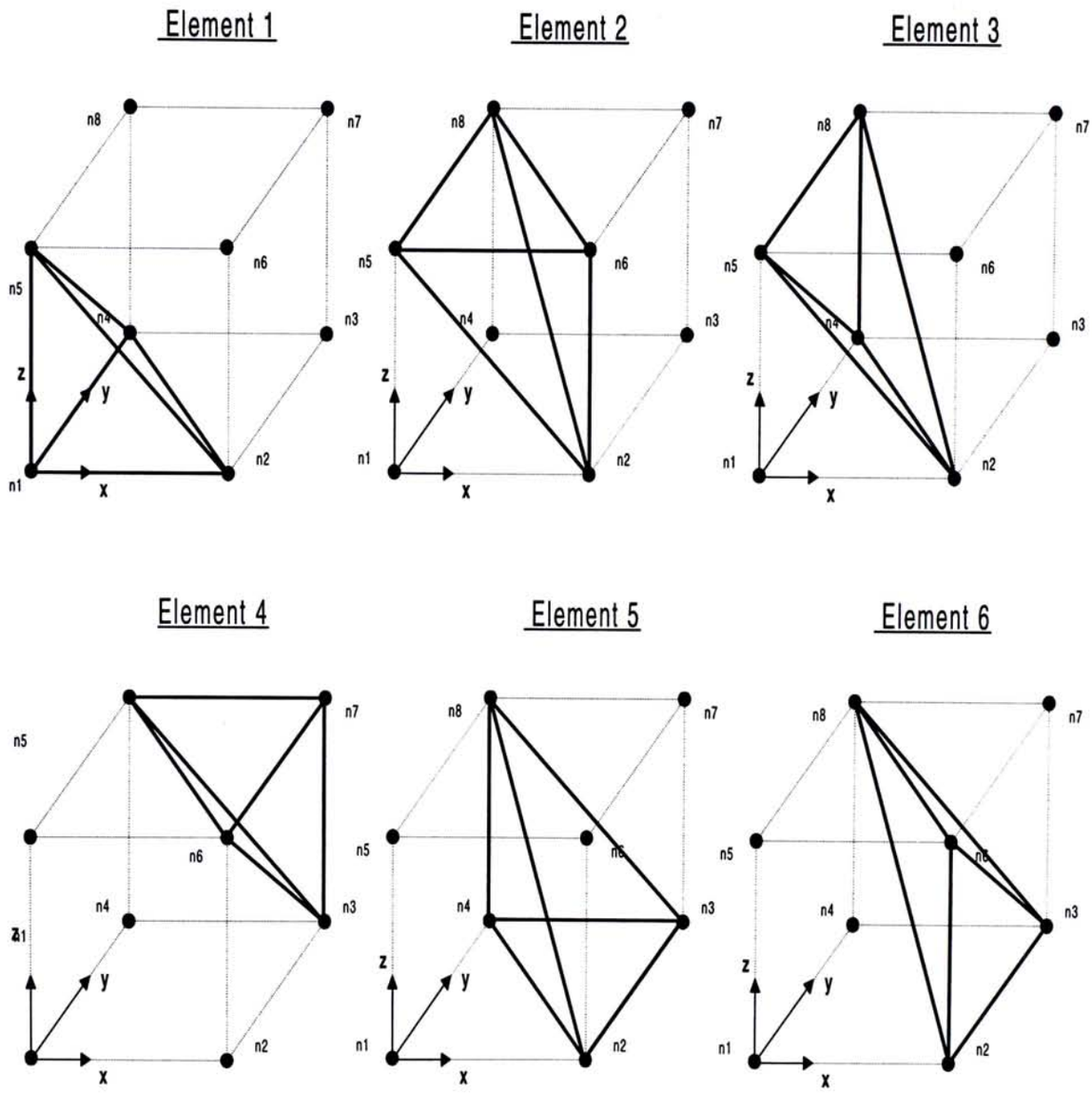

Figure A3.7 Arrangement of tetrahedrons in quadrant (II)

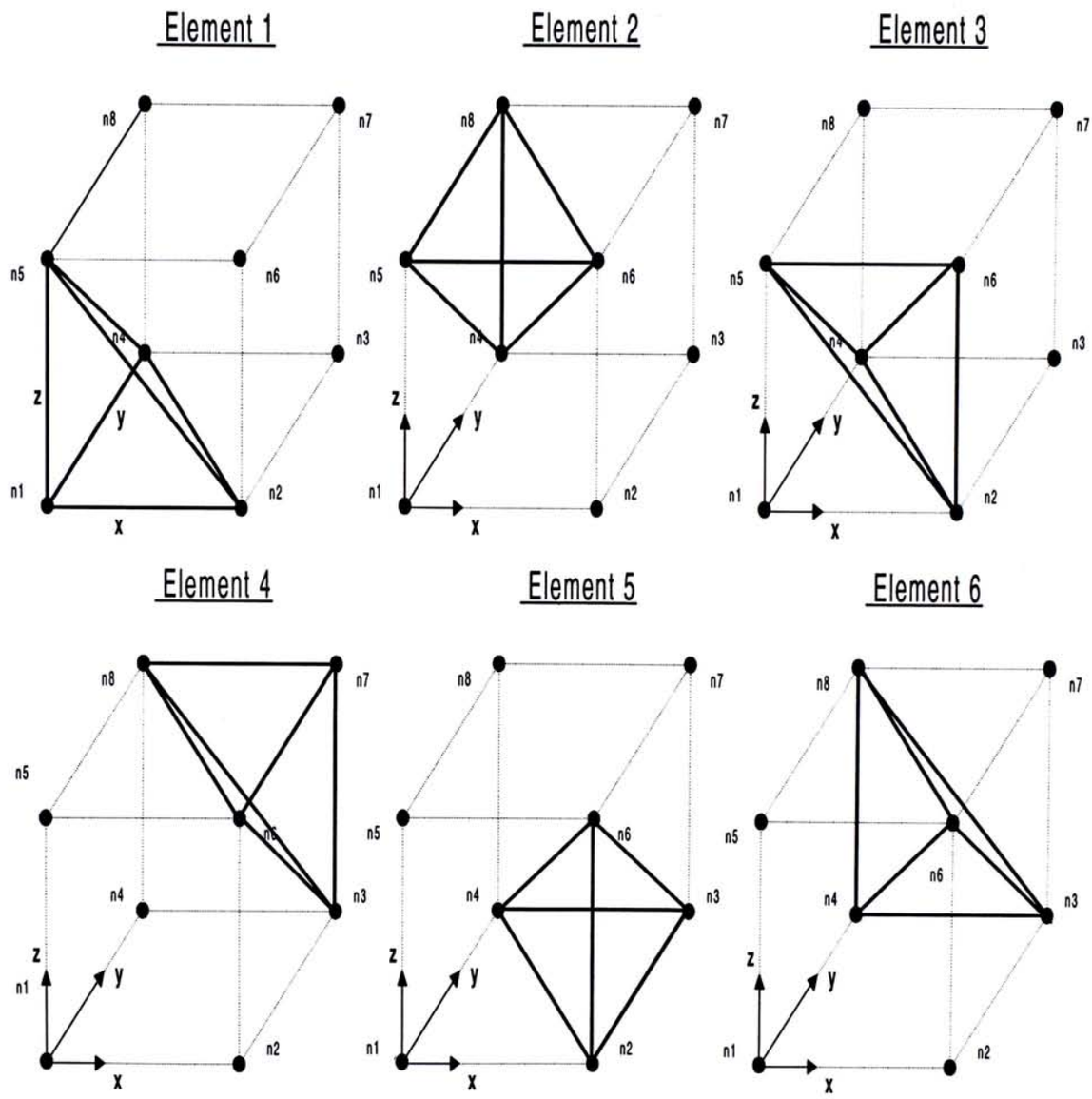

Figure A3.8 Arrangement of tetrahedrons in quadrant (III)

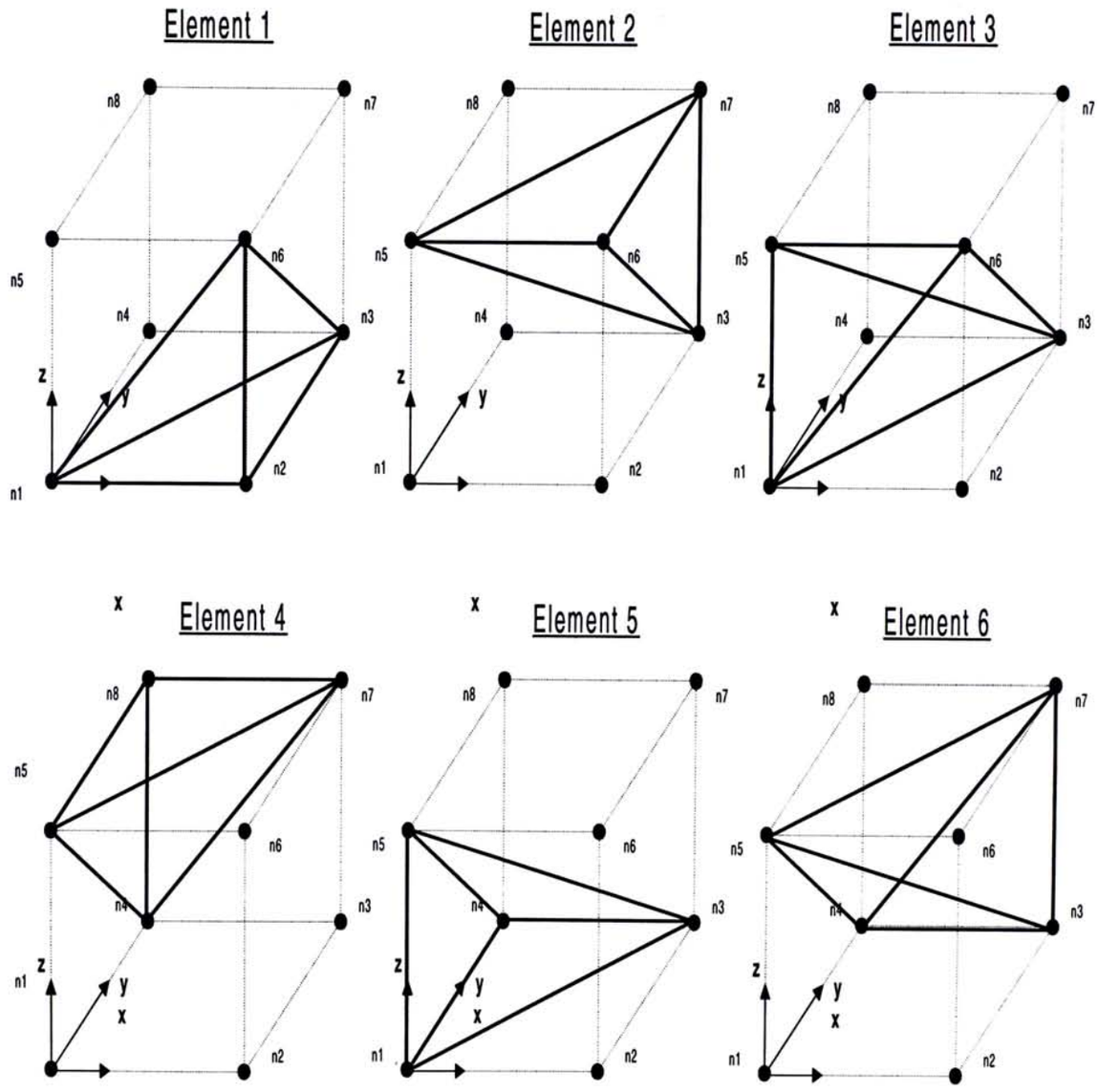

Figure A3.9 Arrangement of tetrahedrons in quadrant (IV)

Bibliography

[1. 1] A.K.Y. Lai, Albert Sinopoli and W.D. Burnside, "A Novel Antenna for Ultra-Wideband Applications", IEEE Transactions on Antenna & Propagation, Vol.40, No. 7, pp. 755-760, July 1992 .

[1.2] Rau Pandya, "Emerging Mobile and Personal Communication Systems", *IEEE Communications Magazine*, Vol. 33, Issue 6, pp. 44-52, June 1995.

[1.3] I.D. Robertson, A.H. Aghvami, "Ultrawideband Biasing of MMIC Distributed Amplifiers Using Improved Active Load", *IEE Electronics Letters*, Vol. 27, No. 21, pp. 1907-1909,October, 1991.

[1.4] Julio Navarro, Yong-Hui Shu and Kai Chang, "A Novel Varactor Tunable Coplanar Waveguide-Slotline Gunn VCO", *IEEE MTTS International Microwave Symposium Digest*, Vol. 3, pp.1187-90, Boston, USA, June 1991.

[1.5] Tsutomu Takenaka, Hiroyo Ogawa, "An Ultra-Wideband MMIC Balanced Frequency Doubler Using Line-Unified HEMTs", *IEEE Transactions on Microwave Theory and Techniques*, Vol. 40, No. 10, pp. 1935-40, October, 1992.

[1.6] Chien-Hsun Ho, Lu Fan, Kai Chang, "Ultra Wide Band Slotline Hybrid Ring Couplers", *1992 IEEE MTTS International Microwave Symposium Digest*, Vol 3, pp.1175-8, Albuqueque, USA, June., 1992.

[1.7] I.D. Robertson, A.H. Aghvami, "Novel Monolithic Ultra-Wideband Unilateral 4-port Junction Using Distributed Amplification Techniques", *1992 IEEE MTTS International Microwave Symposium Digest*, Vol 2, pp. 1051-4, Albuqueque, USA, June., 1992.

[1.8] F. Anderson,W.Christensen, L. Fullerton, B. Kortegaard, "Ultra-Wideband Beamforming in Sparse Arrays", IEE Proceedings-H, Vol. 138, No. 4, pp. 342-346, August 1991.

[1. 9] Larry Fullerton, "UWB Waveforms and Coding for Communications and Radar", *NTC 91, IEEE National Telesystems Conference Proceeding*, Vol.1,pp139-41,Atlanta,USA, March, 1991.

[1.10] Donald E. Voss and Lynn M. Miner, "Ultra-Wideband, High Repetition Rate Single Channel Mobile Diagnostic System", *1992 IEEE MTTS International Microwave Symposium Digest*, Vol 3, pp. 1609-10, Albuqueque, USA, June., 1992.

[1.11] Leon Peters Jr., Jeffrey Daniels, Jonathan Young, "Ground Penetrating Radar as a Subsurface Environmental Sensing Tool", *IEEE Proceedings*, Vol 82, No. 12, December 1994.

[1.12] Sivaprasad Gogineni, K.C. Jezek, Leon Peters, Jonathan Young, Scott Beaven, E Nassar, "Application of Plane Waves for Accurate Measurement of Microwave Scattering from Geophysical Surfaces", *IEEE Transactions on Geoscience and Remote Sensing*, Vol 33, No. 3, May 1995.

[1.13] H.T. Chou, P.H. Pathak, P.R. Rousseau, "An Analytic Treatment of Transient Radiator from Pulse Excited Parabolic Reflectors", *URSI Radio Science Meeting, URSI Digest*, pp 16, Newport Beach, California, June, 1995.

[1.14] Thiele, E., and A. Taflove, "Finite Difference Time-Domain Modeling of Vivaldi Slot Antennas and Array", IEEE Trans. Antenna Propag. Vol.42, pp633-641

[1.15] Kurt Shlager and Glenn Smith, "A resistively loaded bowtie antenna for pulse radiation: FDTD analysis and optimisation", 1993 IEEE Antenna & Propag. Society Symposium, Vol. 2, pp830-3, Ann Arbor, USA, June 1993

[2.1] [Beltzer, A. I.,"variatioal and finite element methods: a symbolic computation approach", Berlin, Springer-verlag, 1990

[2.2] O.C. Zienkiewicz, The Finite Element Method, Mc-Graw-Hill, 1977, p 65-67.

[2.3] Jianming Jin and Weng Cho Chew, "Variational Formulation of Electromagnetic Boundary-Value Problems involving Anisotropic media" Microwave Opt. Tech. Lett., Vol. 7, No. 8, p 348-p 351, June 1994.

[2.4] Jianming Jin, The Finite Element Method in Electromagnetics, Wily, 1993.

[2.5] B. Stupfel, "Numerical Implementation of Second -and Third - ORDER Conformal Absorbing Boundary Conditions for the Vector-Wave Equation", IEEE Trans. Antenna Propagat, Vol. 45, No. 3, Mar. 1997.

[2.6] M.Kuzuoglu and R. Mittra, "Investigation of Nonplanar Perfectly Mehtod Absorbers for Finite Element Mesh Truncation", IEEE Trans. Antenna Propagat., Vol. 45, No. 3, Mar 1997.

[2.7] Thomas B.a. Senior, John L. Volkis, Stephane R. Legault, "Higher Order Impedence and Absorbing Boundary Conditions", IEEE Trans. Antenna Propagat. Vol. 45, No 1, Jan. 1997.

[2.8] J.P. Berenger, "Improved PML for FDTD Solution of Wave- Structure Interaction Problems", IEEE Trans. Antenna Propagat., Vol. 45, No. 3, Mar 1997.

[2.9] Jian Gong, John L. Volakis, A.C. Woo H.T.G. Wang, "A Hybrid Finite Element-Boundary Integral Method for the Analysis of Cavity-Bucked Antennas of Arbitrary Shape", IEEE Trans. Antennas and Propagat. Vol. 42, No. 9, Sept 1994.

[2.10] Cinzia Zuffada, Tom Cwik, Vahraz Jamnejad, "Modelling Radiation with an Efficient Hybrid Finite-Element Integral-Equation Waveguide Mode-Matching Technique", IEEE Trans. Antenna Propagat. Vol. 45, No. 1, Jan 1997.

[2.11] Jian Gong, John L. Volakis, A.C. Woo, H.T.G.Wang, "A Hybrid Finite Element-Boundary Integral Method for the Analysis of Cavity-Backed Antenna of Arbitrary Shape", IEEE Trans. Antenna and Propag., Vol. 42, No.9, Sep,1994

[2.12] Abayliss, M, Gunzburger, E. Turkel, "Boundary Condition for the Numerical Solution of Elliptic Equations in Exterior Regions, SIAM J. Appl. Math., Vol. 42, pp 430-451, Apr. 1982.

[2.13] A.F. Peterson, "Absorbing Boundary Conditions for the Vector Wave Equation", Microwave Opt. Tech. Lett., Vol. 1, pp 62-64, Apr. 1988.

[2.14] J. P. Berenger, "A Perfect Matched Layer for the Absorption of Electromagnetic Waves", J. Comput. Phys. 114, 185-200, 1994.

[2.15] C.H. Wilcox, "An expansion theorem for Electromagnetic Fields", Commun. Pure Appl. Maths., Vol. 9, pp 115-132, 1956.

[2.16] J.P. Webb, V.N. Kanellopulos, "Absorbing boundary conditions for the Finite Element Solution of the Vector Wave Equation", Microwave Opt. Tech Lett., Vol 2, pp 370-372, Oct. 1989.

[2.17] Weng Cho Chew and William H. Weedon, "A 3D Perfectly Matched Medium From Modified Maxwell's Equations With Stretched Co-ordinates", Microwave Opt. Tech. Lett., Vol. 7, no.13, Sept. 1994.

[2.18] Z.S. Sacks, D.M. Kingsland, R. Lee, J. f. Lee, "A Perfectly Method Anisotropic Absorber for Use As an Absorbing Boundary Condition", IEEE Trans. Antermas Propagat ., Vol. 43, pp 1460-1463, Dec. 1995.

[2.19] U. Pebel and R. Mittra, "A Finite-Element-Method Frequency-Domain Application of the Perfectly Matched Layer (PML) Concept", Microwave Opt. Tech. Lett., Vol. 9,No. 3, June 1995.

[2.20] M. Cai. H. Zhou, "Proof of Perfectly Matched Layer Conditions in three Dimensions", Electronics Letters, Vol. 31, No. 19, Sept. 1995.

[2.21] R.P. Edlinger, David M. Kingsland. G. Peng, S.g. Perepelitsa, S.v. Polstyanko J. f. lee, "Application of Anisotropic Absorbers to the Analysis of MMIC Devices by the Finite Element Method", IEEE Trans. Magn., Vol 32, No. 3, May 1996.

[2.22] M. Kuzuoglu, R. Mittra, "Frequency Dependence of the Constitutive Parameters of Causal Perfectly Matched Anisoteopic Absorbers", IEEE Microwave Guided Wave Lett. Vol. 6, No. 12, Dec. 1996.

[2.23] Jo Yu Wu, David M. Kingsland, Jin- Fa Lee, Robert Lee, "A Comparison of Anisotropic PML to Beremger's PML and its Application to the Finite-Element Method for EM Scattering", IEEE Trans. Antennas Propagat. Vol. 45, No. 1, Jan. 1997.

[2.24] Jian-Ming Jin, Wwnng Cho Chew, " Combining PML and ABC for the Finite-Elenent Analysis of Scattering Problems", Micrewave Opt. Tech. Lett., Vol. 12, No. 4, July 1996.

[2.25] M. Hano, "Finite Element Analysis of Dielectric-Loaded Waveguides", IEE Tans. Microwave Theory Tech., Vol. MTT-32, pp. 1275-1279, Oct. 1984.

[2.26] G. Mur, A. T. de Hoop, "A Finite Element Method for Computing Three-Dimentional Electromagnetic Fields in Inhomogeneous Media", IEEE Trans. Magn, Vol. 25, No. 4, July 1958.

[2.27] R.D. Graglia, Ponal R. Witton, A.F. Peterson, "Higher Order Interpolatory Vector Bases for Computational Electromagnetrics", IEEE Trans. Antenna Propagat., Vol. 45, No. 3, Mar. 1997.

[2.28] J.P. Webb, "Edge Elements and What They can do for you", IEEE Trans., Vol. 29, No. 2, Mar. 1993.

[2.29] A. Bossavit, I. Mayergoyz, " Edge Elements for Scattering Problems" IEEE. Trans. Magn. MAG-25, pp. 3019-3021, 1989.

[2.31] C.W. Crowley, P.P. Silvester, H. Hurwitz, "Convariant Projection Elements for 3D Vector Field Problems", IEEE Trans. Microwave Theory Tech., Vol. MTT-39, PP. 395-404, Mar. 1991.

[2.32] K.D.Paulsen, D.R.Lynch, "Elimination of Vector Parasites in Finite Element Maxwell Solutions', IEEE Trans. Microwave Theory Tech., Vol. MTT-39,pp395-404, Mar. 1991

[2.33] A. Bossavit, J.C. Verite, "A Mixed FEM-BIEM Mehtod to Solve 3D Eddy Current Problems", IEEE Trans Magn., Vol MAG-18, pp.431-435, Mar. 1982.

[2.34] S.H. Wong,Z.J.Cendes,"Numerically Stable Finite-Element Methods for the Galerkin Solution of Eddy Current Problems', IEEE. Trans. Magn. MAG-25,pp2019-3021,1989

[2.35] J. S. Savage, A.F.Peterson, "Higher-Order Vector Finite Elements for Tetrahedral Cells',IEEE Trans. Microwave Theory Tech., Vol.44, no. 6, June 1996

[2.36] D.Sun, J. Manges, X. C. Yuan, Z, Cendes, "Spurious Modes in Finite-Element Methods", IEEE Antennas Propagat. Magn. Vol. 37, No. 5, Oct. 1995.

[3.1] Jian Ming Jin and Weng Cho Chew "Combining PML and ABC for the Finite-Element Analysis of Scattering Problems". Microwave Opt. Tech. Lett., Vol. 12, No. 4, July 1996.

[3.2] J.M. Zhou "Automatic Mesh Generation allowing for efficient a priori and a posterior Control of the number and distribution of elements", IEEE Trans. Magn., Vol. 25, No. 4, July 1989.

[3.3] Vijay Srinivasan, Lee R. Nackman, Jung Mu Tang and Siavash N. Meshkat, "Automatic Mesh Generation Using the Symmetric Axis Transformation of Polygonal Domains". Proc. IEEE Vol. 80, No. 9, Sept.1992.

[3.4] A. Nicolas, L. Nicolas, "3D Automatic Mesh Generation For Boundary Integral Mehtod". IEEE Trans. Magn., Vol. 26, No. 2, Mar. 1990.

[3.5] Z. J. Cendes, D. Shenton, H. Shahnasser, "Magnetic Field Computation Using Delaunay Triangulation and Complementary Finite Element Mehtods", IEEE Trans. Magn., Vol Mag-19, No. 6, Nov. 1983.

[3.6] D.N. Shenton, Z.J. Cendes "Three-Dimensional Finite Element Mesh Generation Using Delaunary Tesselation" IEEE Antenna Propagat. Mag., Vol 39, No. 1, Feb. 1997.

[3.7] Jin-Fa Lee, Romanus Oyczij-Edlinger, "Automatic Mesh Generation Using a modified Delaunay Tossellation", IEEE Antenna Propagat. Mag., Vol. 39, No. 1, Feb. 1997.

[4.1] Cohn, S. B., "Slotline on a Dielectric Substrate", IEEE Trans. Microwave Theory Tech., Vol. MTT-17, pp768-778, 1969.

[4.2] S. N. Prasad, S. Mahapatra, "A new MIC Slotline Aerial", IEEE Trans, Antenna Propagat., Vol. AP-31, No. 3, May 1983.

[4.3] Cohn, S. B., "Slotline Field Components", IEEE Trans. Microwave Theory Tech., Vol. MTT-20, pp172-174, 1972.

[4.4] K.C. Gupta, *et al*, "Microstrip Lines and Slotlines", pp269-295, second edit.,1996, Artech House

[A1.1] David S. Burnett, Finite Element Analysis, Wesley, 1988, Chapter 8.

[A2.1] O.C. Zienkiewicz, The Finite Element Method, Mc Graw-Hill, 1997, Chapter 7.